Line Scan Proton Magnetic Resonance Spectroscopic Imaging

by
Jiqun Meng
M.S., University of New Hampshire, 1990

Submitted to the Department of Nuclear Engineering
in Partial Fulfillment of the Requirements for the Degree of

Doctor of Philosophy in Radiological Sciences
at the Massachusetts Institute of Technology
May 1995

Signature of Author . . . . . .
Department of Nuclear Engineering
April 11, 1995

Certified by . . . . . .
Gordon L. Brownell
Professor of Nuclear Engineering, MIT
Thesis Supervisor

Certified by . . . . . .
Robert V. Mulkern
Assistant Professor of Radiology, Harvard Medical School
Thesis Supervisor

Certified by . . . . . .
Sow-Hsin Chen
Professor of Nuclear Engineering, MIT
Thesis Reader

Certified by . . . . . .
David G. Cory
Assistant Professor of Nuclear Engineering, MIT
Thesis Reader

Certified by . . . . . .
Ferenc A. Jolesz
Associate Professor of Radiology, Harvard Medical School
Thesis Reader

Accepted by . . . . . .
Allen F. Henry
Chairman, Committee on Graduate Students

Line Scan Proton Magnetic Resonance Spectroscopic Imaging

by

Jiqun Meng

Submitted to the Department of Nuclear Engineering
on May 1995, in Partial Fulfillment of the
Requirements for the Degree of
Doctor of Philosophy

Abstract

This thesis explores magnetic resonance (MR) imaging methodologies that provide *in vivo* spectroscopic information. To date such information has not been routinely acquired and used in diagnosis. The general objective of the thesis is to develop and implement new and fast MR spectroscopic imaging techniques that can be practically utilized to study spectroscopic information *in vivo*.

This thesis presents innovative line scan spectroscopic imaging methodologies based on spectroscopic interrogation of voxels along strategically oriented tissue columns. The techniques combine some of the most attractive features of both imaging and spectroscopic methods utilizing Carr-Purcell-Meiboom-Gill multiple-echo sequences, rapid acquisition and relaxation enhanced or equivalently fast spin echo sequences, inner-volume localization, and chemical shift imaging principles. The techniques offer a compromise between the low-spectral-resolution, high-spatial-resolution, large-volume-coverage imaging methods of Dixon and Sepponen and the high-spectral-resolution, single-voxel localized proton spectroscopic approaches. Developed and implemented on the conventional 1.5 Tesla clinical MR imaging scanner with standard software and hardware configurations, the non-invasive line scan spectroscopic imaging techniques generate spectroscopic images with high spatial, variable spectral resolution and adequate volume coverage in clinically useful time periods of 10 minutes or less.

This thesis demonstrates the line scan spectroscopic imaging techniques *in vivo*. Spectral concentrations and relaxation times are obtained for bone marrow and brain metabolites. Specifically, quantification of water and saturated fat (concentration and T_2 relaxation time) is performed on vertebral bone marrow in a group of healthy adult volunteers. Studies of developing bone marrow in knee are performed on a group of children and a group of adult volunteers. Furthermore, with variable spectral resolution and slightly modification, the techniques are shown applicable for quantification the lipid chemical composition. The applications include measurements of lipid spectral T_1 relaxation time, detection of terminal methyl protons even with a limited spectral resolution, monitoring of degree of unsaturated fatty acid. In addition, the techniques are modified and applied to quantify and map human brain metabolites. The clinical feasibility of brain metabolite studies is illustrated in a group of healthy adult volunteers and a tumor patient.

The techniques developed in this thesis promise many possible applications. One is to quantitatively study lipid spectra in bone marrow during and after radiation therapy and chemotherapy for patients with bone marrow diseases like leukemia. Another one is to study the evolution of cerebral metabolites within brain tumors to see how relative concentrations of MR observable metabolites correlate with the state of the tumors and the relative progress of various therapies. The other application is to study lipid metabolic disorders, such as cystic fibrosis. The techniques also provides the opportunities to perform dynamic chemical shift imaging studies *in vivo*.

Thesis Supervisor: Gordon L. Brownell
Title: Professor of Nuclear Engineering, MIT

Thesis Supervisor: Robert V. Mulkern
Title: Assistant Professor of Radiology, Harvard Medical School

Thesis Reader: Sow-Hsin Chen
Title: Professor of Nuclear Engineering, MIT

Thesis Reader: David G. Cory
Title: Assistant Professor of Nuclear Engineering, MIT

Thesis Reader: Ferenc A. Jolesz
Title: Associate Professor of Radiology, Harvard Medical School

Acknowledgments

First of all I would like to thank my thesis advisors Dr. Robert Mulkern and Dr. Gordon Brownell. They are the brightest and nicest people I have ever met. I own the opportunity to do this research to Dr. Mulkern. Special thanks for his confidence in supporting me financially. I own him great deal for his constant encouragement at all stage of the project. Without his guidance this thesis would not have been possible. I would also like to express my appreciation for my thesis committee members: Dr. Sow-Hsin Chen, Dr. David Cory and Dr. Ferenc Jolesz for their reviews. Many thanks for Dr. Jolesz for his support. I am indebted to Dr. Cory for his input and advice.

Also I would like to thank Dr. Aria Tzika at Children's Hospital for her advice and support on our brain studies. I am grateful to Howard Lilly at GE Medical Systems for his help with GE MRI scanner. I would especially like to thank Dr. Koichi Oshio at Brigham and Women's Hospital who helped me on MR pulse programming. I am thankful to Dr. Andy Dobrzeniecki at MIT Biomedical Imaging Lab who helped me on my GUI formated automated imaging processing software.

Many thanks for many peoples who helped me one way or another. I could not possibly mention them all.

Finally, I would like to thank my parents and my wife for their support and patience throughout my entire academic career. I could not have done it without them. Special thanks to my wife, Joan Yang, who encouraged me spiritually and helped me technically. Also thanks to my daughter, Yingying Meng, whose smile makes everything worthwhile.

This thesis is dedicated to my parents, Chuanshu Meng and Meiling Ai, my wife, Joan, and my daughter, Yingying.

Table of Contents

List of Figures

(TR/TE = 600/12 ms). The NAA trace was taken from integration across the NAA frequency band in the first echo spectroscopic data sets of the column (TE = 145 ms, Figure 6.3 (c)). The metabolites trace has been multiplied by a scaling factor to make it comparable to the water trace for visualization. Both traces show coincident spikes at the edges of the skull due to strong lipid signal in the T_1-weighted localizer and to lipid signal bleed along the frequency direction into the NAA band at scalp locations in the TE = 145 ms spectroscopic image.

. 142

6.7 line scan metabolite mapping of a healthy 26-year-old man with a 20×20 mm^2) column oriented anteriorly to posteriorly. (a): A localizing image acquired in 23 seconds with a 3 echo RARE sequence (TR/TE = 600/12). (b): A 15 second scout image (5 echo RARE, 120 phase encodes, TR = 600 ms) used to confirm the position of the target tissue column with a dark saturation band. Unlike Figure 6.3 (b), the multiplicative factor of 350 has not been applied to the sampled data, allowing one to see some anatomy. (c): The first echo CPMG spectroscopic image. In this case, 114 ms TE, 96 ms echo readouts and 5 echoes CPMG were employed. The smaller echo spacing reduces T_2-weighted signal loss and leads to a higher temporal sampling of spectral T_2 decay at the expense of spectral resolution. The effective spectral resolution is 10.4 Hz for such scan. Note that the metabolites mapping along the column, the NAA and the combined Cho+CR, are curved in the image. The curvature means a shift in resonance frequency, which is caused by magnetic field inhomogeneity and magnetic susceptibility effect. (d): The summation spectroscopic image generated by adding data from the first 3 echoes (114, 228, and 342 ms) of the CPMG acquisition.

. 144

6.8 An example of the techniques as applied to a 17-year-old boy with a brain tumor of glial origin. Shown are the 20×20 mm^2 tissue column selected for interrogation from a T_2-weighted localizing image (a), the summation image generated from the first 3 echoes

List of Tables

Chapter 1

Introduction

In this thesis innovative magnetic resonance (MR) spectroscopic imaging techniques and their applications are demonstrated. The general objective of the thesis is to develop and implement new and fast MR methodologies to study spectroscopic information *in vivo*. The purpose of this chapter is to review MR spectroscopic imaging and the problems that prevent its practical use clinically, to present an outline on approaches of the thesis, and also to highlight the main contributions of this thesis to the field of MR spectroscopic imaging. This chapter is organized as follows. In Section 1.1 a review on spectroscopic imaging techniques and their associated problems are presented. In Section 1.2 an overview of this thesis is stated. In section 1.3 the factors that motivated the thesis are discussed. Then the main contributions of the thesis are highlighted in Section 1.4. This is followed by an outline of the thesis in Section 1.5.

1.1 Review of Spectroscopic Imaging

Proton MR imaging (MRI) is widely used as a diagnostic modality. Images of internal organs in the human body are routinely acquired by MRI scans. These MR images are collective contributions from chemically distinct hydrogen nucleus within voxels. The images usually reflect water content and in some cases and to some degree, they represent lipid protons. The intensity of the images depend on average relaxation times and density contributions from chemically distinct proton species. Therefore, the diagnosis with MR images alone often lacks biochemical specificity. It is well known that MR can be used to

detect hydrogen nuclei associated with molecules other than water. The basis is that these hydrogen nuclei precess at slightly different frequencies within the magnet. The frequency shift, termed as chemical shift, is determined by the molecular structure and chemical environment. Identifying the types and quantities of different hydrogen nuclei through their chemical shift with MR spectroscopy will give not only biological but also molecular and chemical environmental information. This qualitative and quantitative information may play an important clinical diagnostic role complimentary to conventional MR imaging. MR spectroscopy can provide a non-invasive *in vivo* approach for biochemical analysis in humans [1, 2]. One of the potential applications may be in monitoring and assessment of the therapeutic interventions. The spectroscopic information may provide further insight into both radiation therapy follow-up assessment and prognosis if it could show changes at the cellular biochemical level that precede the morphologic changes detected with MR imaging and/or other radiological imaging modalities. Because of the demands on hardware and methodology, as well as the lack of clearly defined clinical usage, spectroscopic information has not been acquired and used clinically, and so presents a challenge to both scientists and manufacturers in proving its clinical applicability [3].

There are many ways to study spectroscopic information. The general approaches are through imaging based methods, spectroscopy methods, or spectroscopic imaging methods.

The image approach to extract chemical shift was proposed by Dixon and independently by Sepponen [4, 5]. The technique needs two acquisitions to separate water and saturated fat (methylene), the two dominate peaks in proton spectra of many tissues. One acquisition is an "in phase" image, whose phase difference of water and fat is zero, another is "opposed phase" image, whose phase difference is 180 degrees. The "water-only" and "fat-only" images can be obtained by addition and subtraction of in phase and opposed phase images. This two-point technique and its modified version, multi-point Dixon technique [6], have been used for composition assessment in hematological bone

marrow disorders [7], Gaucher disease [8], acute leukemia [9] and to study effects of radiation therapy and chemotherapy [10-13]. Such imaging based approaches generate images with high spatial resolution, excellent anatomic details and contrast to noise ratio, but poor spectral resolution. Since there are more resonance peaks other than water and saturated fat (methylene) in each voxel [14], the limitations of a few points image approaches become obvious in some applications.

There are several spectroscopic approaches to study chemical shift information, such as Stimulated Echo Acquisition Mode (STEAM) sequences [15-18] and the Point Resolved Spatial Selection (PRESS) sequence [P.A. Bottomley, U. S. Patent 4480 228 (1984), 6]. These volume-localized spectroscopy techniques have been used to acquire spectra from single voxels in brain [19] and in vertebral bone marrow [20-22]. Such approaches offer high spectral resolution and can provide more precise measurements of water and fat (methylene/methyl) cellularity than Dixon-based imaging methods. In addition to water and methylene/methyl peak quantification, smaller lipid resonance peaks other than water and methylene peaks as well as spectral peak relaxation times can also be measured. These offer a means to assess lipid chemical composition and to probe microscopic chemical and physical environments of protons under observation [23-24]. The single voxel spectroscopy approaches are limited by relatively low spatial resolution and volume coverage. Lengthy acquisition times are required if relaxation behavior is to be studied.

1.2 Thesis Overview

In this thesis, the author presents line scan spectroscopic imaging methods based on spectroscopic interrogation of voxels along strategically oriented tissue columns [25-26]. The techniques combine some of the most attractive features of both imaging and spectroscopic methods utilizing Carr-Purcell-Meiboom-Gill (CPMG) multiple-echo sequences [27], rapid acquisition and relaxation enhanced (RARE) or equivalently fast spin

echo (FSE) sequences [28-30], inner-volume localization [28, 31], and chemical shift imaging principles [29, 32]. The techniques offer a compromise between the low-spectral-resolution, high-spatial-resolution, large-volume-coverage imaging methods of Dixon and Sepponen and the high-spectral-resolution, single-voxel localized proton spectroscopic approaches. Developed and implemented on the conventional 1.5 Tesla clinical MR imaging scanner with standard software and hardware configurations, the non-invasive line scan spectroscopic imaging techniques generate spectroscopic images with high spatial, variable spectral resolution and adequate volume coverage in clinically useful time periods of 10 minutes or less.

In this thesis, the line scan spectroscopic imaging techniques are demonstrated *in vivo* [33-38]. Spectral concentrations and relaxation times are obtained for bone marrow and brain metabolites. Specifically, quantification of water and saturated fat, or cellularity measurement, is performed on vertebral bone marrow in a group of healthy adult volunteers. Studies of developing bone marrow in knee are performed on a group of children and a group of adult volunteers. Furthermore, with variable spectral resolution and slight modification, the techniques are shown applicable for quantification the lipid chemical composition [33-36]. The demonstrations include measurements of lipid spectral T_1 relaxation time, detection of terminal methyl protons even with a limited spectral resolution [33], monitoring of degree of unsaturated fatty acid, and study of levels of mono-unsaturated versus poly-unsaturated triglycerides [34]. In addition, the techniques are modified and applied to quantify and map human brain metabolites. The clinical feasibility of brain metabolite studies is illustrated in a group of healthy adult volunteers and a tumor patient.

The techniques developed in this thesis promise many possible applications. One is to quantitatively study lipid spectra in bone marrow during and after radiation therapy and chemotherapy for patients with bone marrow diseases like leukemia. Another one is to study the evolution of cerebral metabolites within brain tumors to see how relative

concentrations of MR observable metabolites correlate with the state of the tumors and the relative progress of various therapies. The other application is to study lipid metabolic disorders, such as cystic fibrosis.

The specific goals of this thesis are: (1). to demonstrate the techniques as a very applicable tool in the clinical setting; (2). to apply the techniques to the studies of vertebral bone marrow in the lumber spine of adults; (3). to apply the techniques to the characterization of developing bone marrow in the knees of children and adults; (4). to modify and apply the techniques to the studies of human brain metabolites; (5). to determine optimal compromises between acquisition speed, spectral resolution, and relaxation measurement; (6). to automate the image processing algorithms for fast data analysis and clinical interface and/or interpretation.

1.3 Motivation of the Thesis

The first motivation factor for this thesis is to develop and optimize new MR methodologies to generate spectroscopic images. For *in vivo* studies the methods are designed to combine the imaging methods with spectroscopy. They are optimized to maintain a balance between spectral resolution, volume coverage, speed and relaxation properties. To utilize spectroscopic information practically and effectively in clinical setting, the new methods have to be fast enough and convenient enough so that they can be easily incorporated into clinical protocols. At the same time, the methods have to provide well-defined spectroscopic information.

The second motivation factor is to see the new MR spectroscopic imaging tools successfully implemented on a conventional MRI scanner. The spectroscopic imaging can then be tested for their use in clinical diagnosis. To bring the broad spectrum of spectroscopic information into clinical reality, new tools that ensure spectroscopic information can be acquired accurately and practically are needed. The impact can be huge

with appropriate methodologies developed and implemented on conventional 1.5 T clinical scanner without costly hardware upgrades.

A final compelling motivation factor is to develop new spectroscopic imaging methodologies that offer opportunities for dynamic chemical shift imaging study *in vivo*. As in functional MR imaging, the scan time or temporal resolution is crucial in dynamic studies. Developing fast MR spectroscopic imaging methods may provide such possibilities.

1.4 Main Contributions of the Thesis

In this section the significant contributions of this thesis to the field of MR spectroscopic imaging are highlighted as follows:

The major contribution of the thesis is the development and implementation of innovative MR spectroscopic imaging methodologies [25, 26, 33-39]. Specifically, the focus is on combining CPMG, RARE (or FSE) imaging techniques, inner volume selection scheme, with principles of spectroscopy. The methods offer a compromise between the low-spectral-resolution, high-spatial-resolution, large-volume-coverage imaging methods of Dixon and Sepponen and the high-spectral-resolution, single-voxel localized proton spectroscopic approaches. The acquisitions can be either in imaging fashion that generates the localizing images or in spectroscopic imaging fashion that generates spectroscopic images with CPMG and RARE techniques. Extensive regions of tissue are interrogated by exciting strategically oriented columns. Spectroscopic images of the columns are acquired with high spatial and variable spectral resolution. Information about spectral concentrations, T_1 and T_2 relaxation times are extracted and mapped from each voxel of such spectroscopic images.

The second contribution of the thesis is the development of fast spectroscopic imaging techniques. The techniques generate spectroscopic images much faster than

conventional MR spectroscopic techniques while the images are still informative. As currently implemented, the CPMG spectroscopic imaging techniques generated images that suitable for spectral T_2 and concentration analysis in 4 minutes and 18 seconds while conventional spectroscopic techniques need scan time of 40 minutes. The RARE spectroscopic imaging techniques with 7 echo train generate image in 36 seconds versus 4.5 minutes for the conventional spectroscopic techniques. Limitations of existing techniques for spectroscopic studies include long scan time, so that no spectroscopy is performed routinely in diagnosis. The techniques developed in this thesis can be performed in short scan times, which makes clinical spectroscopic studies practical. Also the short scan time is an especially important advantage when performing MR examinations on very ill patients or on children. In both cases, prolonged scan times either are not available or require increased sedation.

The third contribution of the thesis is the development and implementation of non-invasive methodologies on a conventional 1.5 Tesla clinical MRI scanner with standard software and hardware configurations, which make it convenient to extract spectroscopic information along with conventional MRI examinations. The practical significance of the technologies is that they can be feasibly incorporated into clinical protocols to perform spectroscopic studies on clinically important targets.

The fourth contribution of the thesis is that the new methodologies promise many potential applications, some are demonstrated in this thesis. As very applicable tools, the new methodologies are applied in quantification of vertebral bone marrow in lumbar spine [25], developing bone marrow in knee [26], and brain metabolites in human. This thesis also presents the feasibility to study the lipid chemical composition and degree of unsaturation in fatty acids [33-38]. The suggested applications of the thesis are: (1). to measure bone marrow compositions instead of using painful and invasive bone marrow biopsies; (2). to monitor the response of leukemia patients to radiation therapy; (3). to study progression of bone marrow disorders by monitoring red to yellow bone marrow

conversion with aging; (4). to identify people who are at risk of artherosclorosis by studying lipid chemical composition; (5). to evaluate relative cerebral metabolite concentrations and relaxation times in brain tumors during course of therapy; (6). to characterize relative cerebral metabolites concentration in children with diffuse white matter disease.

The fifth contribution of the thesis is the design of an automated image analysis software package [37]. The image processing software, designed in graphics user interface format on Sun workstation, makes it convenient to extract spectroscopic information from acquired spectroscopic images.

The final contribution of the thesis is providing the possibilities to perform dynamic chemical shift imaging studies *in vivo*. Like functional MRI where many fast imaging techniques have been developed, the fast scan spectroscopic imaging techniques are also essential in dynamic chemical shift studies. The spectroscopic imaging techniques described in this thesis may provide opportunities in studying dynamic chemical shift imaging [39]. In contrast to echo-planar imaging which requires specialized and expensive hardware for fast gradient switching, large peak amplitudes and fast data acquisition [40], the techniques in this thesis require no special hardware and software since they are implemented on the conventional MRI scanner.

1.5 Thesis Outline

This thesis consists of seven chapters, and is organized as follows:

Chapter 1 introduce the concepts of spectroscopic imaging techniques, presents the overview and the motivations of this thesis. Contributions to the field of MR spectroscopic imaging are highlighted.

Chapter 2 provides some background materials that are important to this thesis, including CPMG and RARE imaging techniques, relaxation phenomena, structure of a conventional MR scanner, and outline of image reconstruction.

Chapter 3 presents the line scan CPMG and RARE spectroscopic techniques. It covers image localization protocols, pulse sequence designs, k-space sampling, 2-D Fourier transformation representation, optimization of spectral resolution, T_2 relaxation time measurement and acquisition speed. Also discussed is the practical significance of the column selection scheme. The post processing methods for acquired spectroscopic images are illustrated.

Chapter 4 demonstrates the applications of the techniques to quantify vertebral bone marrow and knee bone marrow *in vivo*. The lumbar spine studies, consisting of a group of healthy adult volunteers, concentrate on the cellularity measurements. The developing knee marrow studies, consisting a group of healthy adult volunteers and a group of children, focus on spectral characterization of red and yellow marrow and the potential to monitor the conversion from red to yellow marrow. In both cases, the relative concentrations and T_2 relaxation values from extensive region of bone marrow are obtained and mapped for the major proton resonance peaks.

Chapter 5 illustrates the applications of the techniques to study lipid chemical composition. This capacity is demonstrated on an array of oil phantoms in which lipid spectral resonances are mapped spatially. The pulse sequences are modified with a non-selective inversion pulse and applied to yellow marrow of a group of healthy adults. The spectral T_1 relaxation values for major lipid protons are obtained, as well as the detection of terminal methyl protons even with a limited spectral resolution. The potential to monitor the degree of unsaturated fatty acids in bone marrow is demonstrated.

Chapter 6 presents the applications of the techniques to study human brain metabolites. Major metabolites in proton spectrum (N-acetyl aspartate, choline containing compounds/creatine) are quantified and mapped. T_2 relaxation values of the NAA and composite Cho+Cr protons are obtained from a group of healthy adult volunteers. The improvement of signal-to-noise ratios is examined by adding data from several different echoes. The potential to study brain disorders is demonstrated with a tumor patient.

Chapter 7 summarizes the thesis, suggests potential clinical applications, and outlines future research possibilities.

References

1. Radda GK, Rajagopalan B, Taylor DJ. Biochemistry in vivo: an appraisal of clinical magnetic resonance spectroscopy. Magn Reson Quarterly 1989; 5:122-151.

2. Weiner MW. The promise of magnetic resonance spectroscopy for medical diagnosis. Invest Radiolo 1988; 23:253-261.

3. Bottomley PA. Human in vivo NMR spectroscopy in diagnostic medicine: clinical tool or research probe? Radiology 1989; 170:1-15.

4. Dixon WT. Simple proton spectroscopic imaging. Radiology 1984; 153:189-194

5. Sepponen RE, Sipponen JT, Tanttu JI. A method for chemical shift imaging: Demonstration of bone marrow involvement with proton chemical shift imaging. J. Comput Assist Tomogr 1984; 8:585-587.

6. Glover GH. Multipoint Dixon technique for water and fat proton and susceptibility imaging. JMRI 1991; 1:521-530.

7. Rosen BR, Fleming DM, Kushner WP, Wismer GL, Brady TJ. Hematologic bone marrow disorders: quantitative chemical shfit MR imaging. Radiology 1988; 169:799-804.

8. Johnson LA, Hoppel BE, Gerard EL, Miller SP, Doppelt SH, Zirzow GC, Rosenthal DI, Dambrosia JM, Hill SC, Brady RO, Rosen BR, Barton NW. Quantitative chemical shift imaging of vertebral bone marrow in patients with gaucher disease. Radiology 1992; 182:451-455.

9. Gerard EL, Ferry JA, Amrern PC, Harmon DC, McKinstry RC, Hoppel BE, Rosen BR. Compositinal changes in vertebral bone marrow during treatment for acute leukemia: assessment with quantitative chemical shift imaging. Radiology 1992; 183:39-46.

10. Casamassima F, Ruggiero C, Caramella D, Tinacci E, Villari N, Ruggiero M. Hematopoietic bone marrow recovery after radiation therapy: MRI evaluation. Blood 1989; 73:1677-1681.

11. Kauczor H, Brix G, Dietl B, Jarosch K, Knopp MV, Kaick G. Bone marrow after autologous blood stem cell transplantation and total body irradiation: Magnetic resonance and chemical shift imaging. Magne Reson Imag 1993; 11:965-975.

12 Steiner RM, Mitchell DG, Rao VM, Murphy S, Rifkin MD, Burk DL Ballas SK, Vinitski S. Magnetic resonance imaging of bone marrow: Diagnostic value in diffuse hematologic disorders. Magn Reson Quart 1990; 6:17-34.

13 Fletcher BD, Wall JE, Hanna SL. Effect of hematopoietic growth factors on MR images of bone images of bone marrow in children undergoing chemotherapy. Radiology 1993; 189:745-751.

14. Brix G, Heiland S, Bellemann ME, Koch T, Lorenz WJ. MR imaging of fat -containing tissues: Valuation of two quantitative imaging techniques in comparison with localized proton spectroscopy. Magnetic Resonance Imaging 1993; 11:977-991.

15. McKinnon G. Volume selective excitation spectroscopy using the stimulated echo, "Proc., SMRM, 5th Annual Meeting, 1986, " p.168

16. Granot J. Selected volume excitation using stimulated echoes (VEST). Application to spatially localized spectroscopy and imaging. J. Magn. Reson. 1986; 70:488-492.

17. Frahm J, Merboldt KD, Haenicke W. Localized proton spectroscopy using stimulated echoes. J. Magn. Reson. 1987; 72:502-508.

18. Kimmich R, Hoepfel D. Volume-selective multipulse spin echo spectroscopy. J. Magn. Reson. 1987; 72:379-384

19. Ross BD (ed.). Proton spectroscopy in clinical medicine. NMR Biomed. 1991; 4.

20. Ballon D, Jakubowski A, Gabrilove J, Graham MC, Zakowski M, Sheridan C, Koutcher JA. In vivo measurements of bone marrow celularity using volume-localized proton NMR spectroscopy. Magn Reson. Med. 1991; 19:85-95.

21. Schick F, Bongers H, Jung W, Skalej M, Lutz O, Claussen CD. Volume-selective proton MRS in vertebral vodies. Magn. Reson Med 1992; 26:207-217.

22. Jensen KE, Jensen M, Grundtvig P, Thomsen C, Karle H, Henriksen O. Localized in vivo proton spectroscopy of the bone marrow in patients with leukemia. Magn Reson Imaging 1990; 8:779-789.

23. Schick F, Eismann B, Jung W, Bongers H, Bunse M, Lutz O. Comparison of localized proton NMR signals of skeletal muscle and fat tissue in vivo: Two lipid compartments in muscle tissue. Magn. Reson Med 1993; 29:158-167.

24. Schick F, Bongers H, Jung W, Eismann B, Skalej M, Einsele H, Lutz O, Claussen C. Proton relaxation times in human red bone marrow by volume selective magnetic resonance spectroscopy. Appl Magn Reson 1992; 3:947-963.

25. Mulkern RV, Meng J, Oshio K, Williamson DS, Lilly HS, Guttmann CRG, Jaramillo D. Inner volume CPMG spectroscopic imaging of developing bone marrow in the knee: red and yellow marrow characterization. J. Comput Assist Tomogr. 1995; 19(2): 247-255.

26. Mulkern RV, Meng J, Oshio K, Guttmann CRG, Jaramillo D. Bone marrow characterization in the lumbar spine with inner volume spectroscopic CPMG imaging studies. JMRI 1994; 4:585-589.

27 Meiboom S, Gill D. Modified spin-echo method for measuring nuclear relaxation times. Rev Sci Instrum 1958; 29:688-691.

28. Oshio K, Mulkern RV. Rapid fat/water assessment in knee bone marrow with inner volume RARE spectroscopic imaging. JMRI 1992; 2:601-604.

29. Mulkern RV, Melki PS, Lilly HS, Hoffer FA. 1D spectroscopic imaging with RF echo plannar (SIRFEN) methods. Magn Reson Imaging 1991; 9:909-916.

30. Hennig J, Naureth A, Friedburg H. RARE imaging: a fast imaging method for clicical MR. Magn Reson Med. 1986; 3:823-833.

31. Feinberg DA, Hoenninger JC, Crooks LE, Kaufman L, Watts JC, Arakawa M. Inner Volume MR imaging: technical concepts and their application. Radiology 1985; 156:743-747.

32. Brown TR, Kincaid BM, Ugurbil K. NMR chemical shift imaging in three dimensions. Proc Natl Acad Sci USA 1982; 79:3522-3526.

33. Meng J, Oshio K, Williamson DS, Mulkern RV. Inversion recovery spectroscopic imaging of bone marrow: lipid T_1 relaxation and terminal methyl detection. Book of Abstracts, Second Meeting of SMR, Volume 1, Page 180, 1994.

34. Mulkern RV, Lilly HS, Meng J, Bowers J, Guttmann CRG, Oshio K, Williamson DS, Jaramillo D. Assessing triglyceride unsaturation with a proton spectroscopic imaging method: in vivo and in vitro studies. Book of Abstract, Second Meeting of SMR, Volume 1, Page 176, 1994.

35. Mulkern RV, Meng J, Oshio K, Jaramillo D, Williamson DS. In vivo measurements of lipid chemical composition in bone marrow with a line scan CPMG ^1H spectroscopic imaging method. Book of Abstracts, ENC, 1995.

36. Jaramillo D, Meng J, Mulkern RV. Evaluation of red and yellow marrow in children and young adults using spectroscopic CPMG imaging. Book of Abstracts, RSNA, 1993.

37. Mulkern RV, Meng J. Fat and water quantification in spine and knee with inner volumn CPMG sequences and automated post-processing. Book of Abstracts, SMRI 3, 1993.

38. Tice HM, Mulkern RV, Meng J, Jolesz FA. Spectroscopic studies of the pituitary fossa with an inner volumn spectroscopic imaging techniques. Book of Abstracts, ASNR, 1992.

39. Mulkern RV, Meng J, Lilly HS, Oshio K. Dynamic chemical shift imaging. SMRI, 12th Annual Meeting, March 1994.

40. Cohen MS, Weisskoff RM. Ultra-fast imaging. Magn Reson Imaging. 1991:9:1-37.

Chapter 2

Background

In this chapter some background materials that are essential to this thesis are briefly presented. This chapter is organized as follows. In Section 2.1 the CPMG sequence is illustrated. In Section 2.2 the RARE sequence is demonstrated. This is followed by a discussion of the relaxation phenomena in Section 2.3. Then in Section 2.4 the structure of the clinical MRI scanner used for experiments in this thesis is presented. In Section 2.5 the way RF receiver acquires signal is described. The chapter concludes with an outline on image reconstruction in Section 2.6.

2.1 CPMG Sequence

The Carr-Purcell-Meiboom-Gill (CPMG) sequence, or called phase shifted Carr-Purcell, is based on Carr-Purcell (CP) sequence [1]. The CPMG may be described as a $\pi/2$ (+x), τ, π (+y), 2τ, π (+y), 2τ, π (+y), 2τ, ..., sequence. The $\pi/2$ pulse is applied along the positive x axis and π pulses are along the positive y axis while in CP the π pulses are along x axis. The echoes are generated at 2τ, 4τ, 6τ, ... In CPMG the echoes are along the positive y axis instead of alternatively positive and negative as in CP. CP experiment requires that pulses be reasonably accurate and that the RF pulses be uniform over the entire sample volume. Because the RF field inhomogeneity over the entire sample makes it quite impossible in most cases to have pulses set accurately for entire sample, the errors in setting the π pulses in a CP sequence accumulate and become quite

troublesome. The advantage of CPMG over CP is that the accumulated errors due to imperfect π pulses are minimized [2].

2.2 RARE Sequence

The Rapid Acquisition Relaxation Enhanced (RARE) sequence was pioneered in 1986 by Hennig [3]. With slight modifications, the sequence has been called fast spin echo (FSE) [4, 5]. The FSE sequence is a variant of the echo planar method first proposed by Mansfield and Maudsley [6]. A demonstration of its use for making images was first described by Hall and Sukumar [7]. The essential difference between clinically demonstrated FSE sequence and those methods widely referred to as echo planar imaging (EPI) [6, 8-11] lies in the way the echoes are created. The FSE sequence utilizes RF refocused echoes generated from a CPMG sequence while EPI methods utilize gradient recalled echoes.

In both FSE and EPI techniques, a single excitation of the spins is followed by an echo train during which each echo is individually phase encoded and sampled in the presence of a frequency encoding gradient. The number of frequency encoding steps determines the number of pixels along the read direction in the final image. Therefore, sampling rates and desired pixel resolution along the read axis limit minimum echo spacing in both sequences. In a single shot excitation scheme, the number of echoes following the original excitation determines the number of pixels in the phase encoding direction. It becomes a practical matter to attempt to acquire as many echoes as possible in a single echo train in order to reduce data acquisition times.

In FSE sequence the echo spacings are longer than those from gradient recalled EPI sequence. The reason is that the RF refocusing pulses take some time, especially if they are slice selective. This lengthens the minimum spacing between echoes available in a FSE sequence over that permitted by an EPI sequence.

In both FSE and EPI sequences, echoes are collected while natural relaxation processes are reducing successive echo heights. The effects these relaxation processes are two-fold: a blurring artifact in the phase encoding direction, and T_2 image contrast [3, 12].

2.3 Relaxation Phenomena

The T_1 relaxation, the spin-lattice relaxation time, is a measure of how rapidly the z component of the magnetization reaches thermal equilibrium if it is displaced from its equilibrium state by the absorption of RF energy [13]. The main feature of T_1 relaxation is an exchange of spin energy with the thermal energy of the molecules, or the lattice. Only fast fluctuations (occur at the rate of $1 / \omega_0$ or faster) contribute to T_1 relaxation. For liquid systems such as water, typical T_1 relaxation times lie in the range of 0.1-10 second. In solids, where the motion is considerably less, T_1 relaxation times could be minutes or even hours.

The T_2 relaxation, spin-spin relaxation, is a measure of how rapidly the transverse components of magnetization lose phase coherence. It is the process in which the transverse magnetization in the rotating frame is destroyed. In contrast to T_1 relaxation, both fast and slow fluctuations contribute to T_2 relaxation. Consequently, T_2 is always equal to or less than T_1.

The T_1 and T_2 relaxations *in vivo* are complex processes to which many different relaxation mechanisms exist: dipole-dipole interaction, J-coupling, paramagnetic, susceptibility, diffusion, etc. Generally the T_1 and T_2 relaxation times are tissue specific and have been used for characterizing certain diseases [14-17]. *In vivo* measurement of the T_1 and T_2 relaxation times, particularly of individual spectral peaks, may provide insight in clinical diagnosis.

2.4 Scanner Overview

The instrument used for experiments of this thesis is a standard 1.5 Tesla GE Signa whole body MRI clinical scanner with 4.x hardware and software configuration (General Electric Medical Systems, Milwaukee, Wisconsin). The block diagram in Figure 2.1 shows the hardware configurations of the scanner. The hardware consists of the host computer (Data General MV4000) connected to the transceiver processing and storage (TPS) chassis, and the consolidated pulse control module which the pulse sequence generator boards (PSG) are contained within. The TPS chassis consists of a 68020 CPU, and array processor, bulk access memory, data acquisition board, the receiver and the exciter. The PSG boards provide control of the devices and also produce 16 bit digital waveforms for the gradient and RF amplifiers. There are six PSG boards in all: XGRAD, YGRAD, ZGRAD, RHO (RF envelope), THETA (RF phase), and LOGIC (master board). The first five are descriptive of the device being controlled. The last board is not descriptive and linked to bus and controls the hardware in TPS. The LOGIC board is the master board because when it stops all the other boards stop.

In designing new MR experiments, pulse sequence database programs (PSD) have to be developed to control the hardware. A pulse program controls gradient boards, RF boards, digital exciter, receiver, master board, and keeps all components operating in a sequential order. A pulse program also loads in appropriate frequencies, phases, order of waveforms, as well as specifying the way data are acquired and images are reconstructed. MR physics, computer architecture, digital hardware knowledge and computer software skills are involved in designing and implementing new PSDs.

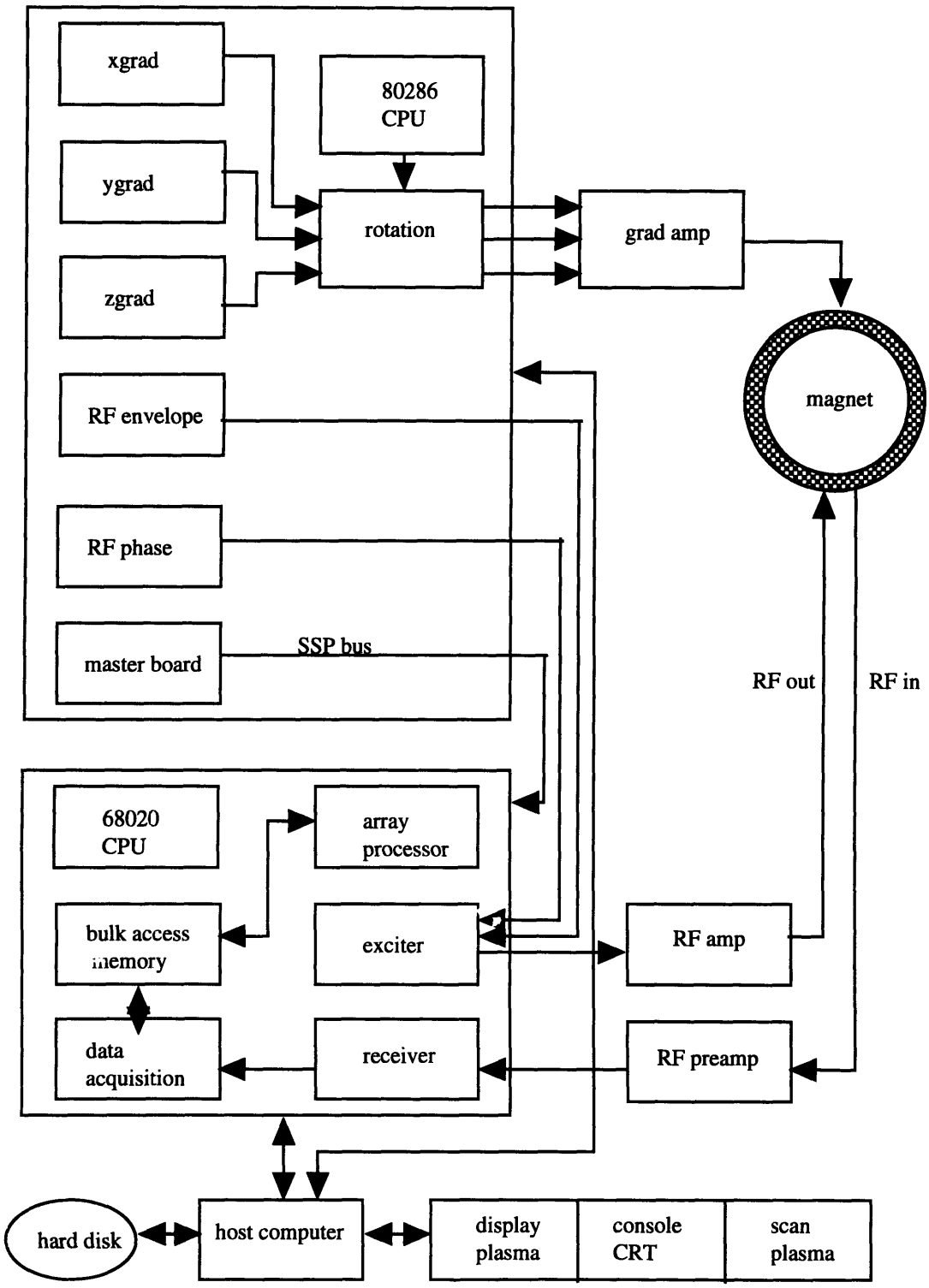

Figure 2.1: Hardware configurations of a clinical MRI scanner.

2.5 Data Acquisition

The main structure of the RF receiver of the GE Signa scanner is schematically shown in Figure 2.2. To understand how the data are acquired, follow the path of an input signal from a coil, through the mixers, the anti-alias filter, A/D converter, and digital filtering. The signal from the coil is mixed with the receiver frequency to create an intermediate frequency signal centered at 187.5 kHz. An anti-alias filter immediately prior to the A/D converter reduces the bandwidth of the signal to 125 kHz, again centered at 187.5 kHz. The A/D converter has 250 kHz fixed sampling rate. Since the signal is band-limited to 125 kHz, aliasing is not a concern. The sampled signal is then broken down digitally into inphase (I channel) and quadrature (Q channel) components which then enter separate digital filter paths.

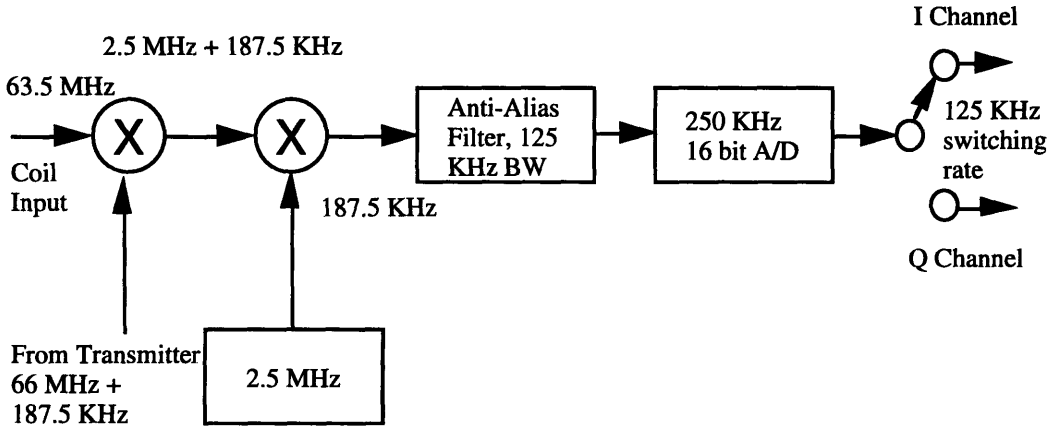

Figure 2.2: Schematic representation of RF receiver of the scanner.

The sampled signal, with a frequency spectrum centered at 62.5 kHz, can also be viewed as a low pass signal whose spectrum is reflected and centered at 62.5 kHz. To create

I/Q pairs in the analog domain, it would be necessary to mix this signal down to the baseband with $\sin(2\pi \times 62.5 \times t)$ and $\cos(2\pi \times 62.5 \times t)$ where t is time. In digital domain, replacing t with n/250 gives following two mixing signals: $\sin(n\pi / 2)$ and $\cos(n\pi / 2)$. For n = 0, 1, 2 ..., gives {0, 1, 0, -1} for sine and {1, 0, -1, 0} for cosine. The task of multiplying every other point by zero is equivalent to switching the A/D output between I and Q channels. Thus, points sampled at even discrete time units move to the I channel, and points sampled at odd discrete time units move to the Q channel.

2.6 Image Reconstruction Outline

This section outlines the general steps of image reconstruction. Most of the images contained in this thesis were reconstructed on-line, though some were reconstructed off-line. The recon routine does the following:

For each scan, build fermi (low pass) filter. For each echo, perform rational image scaling depending on pre-scan attenuation factors and divide frame by number of excitations. If y resolution < 256, zero fill to 256, perform frequency FFT (x-direction) and phase FFT (y-direction). Then calculate magnitude, phase, I or Q image, as well as Clip/Offset.

References

1. Carr HY, Purcell EM. Effects of diffusion on free precession in nuclear magnetic resonance experiments. Phys. Rev. 1954; 42:630-638.

2. Farrar TC, Pulse Nuclear Magnetic Resonance Spectroscopy, The Farragut Press, Chicago, 1987.

3. Hennig J, Naureth A, Friedburg H. RARE imaging: a fast imaging method for clicical MR. Magn Reson Med. 1986; 3:823-833.

4. Jones K, Mulkern RV, Mantello MT, Melki PS, Ahn SS, Barnes PD, Jolesz A. Brain Hemorrhage: Evaluation with fast spin echo and conventional dual spin echo images. Radiology 1992; 182: 53-58.

5. Melki PS, Mulkern RV, Panych LP, Jolesz FA. Comparing the FAISE method with conventioal dual echo sequnces. JMRI 1991; 1: 319-326.

6. Mansfield P, Maudsley AA. Plannar spin imaging by NMR J. Magn. Reson. 1977; 27: 101-119.

7. Hall LD, Sukuman S. Rapid data acquisition for NMR imaging by the projection reconstruction method. J. Magn. Reson. 1984; 56: 179-182

8. Stehling JM, Howseman AM, Ordidge, RJ, Chapman B, Turner R, Coxon R, Golver P, Mansfield P, Coupland R. Whole-body echo-plannar MR imaging at 0.5 T. Radiology 1989; 170: 257-263.

9. Chapman B, Turner R, Ordidge RJ. Real time movie imaging from a single cardiac cycle by NMR. Magn. Reson. Med. 1987 5: 246-254.

10. Howseman AM, Stehling MK, Chapman B. Improvements in snap-shot NMR imaging. Br. J. Radiol. 1988 61: 822-828.

11. Cohen MS, Weisskoff RM. Ultra-fast imaging. Magn Reson Imaging. 1991:9:1-37.

12. Johnson G, Hutchinson JMS. The limitation of NMR recalled echo imaging techniques J. Magn. Reson. 1985; 63: 14-30.

13. Morris PG, Nuclear magnetic resonance imaging in medicine and biology. Clarendon Press, Oxford, 1986.

14. Rosen BR, Fleming DM, Kushner WP, Wismer GL, Brady TJ. Hematologic bone marrow disorders: quantitative chemical shfit MR imaging. Radiology 1988; 169:799-804.

15. Johnson LA, Hoppel BE, Gerard EL, Miller SP, Doppelt SH, Zirzow GC, Rosenthal DI, Dambrosia JM, Hill SC, Brady RO, Rosen BR, Barton NW. Quantitative chemical shift imaging of vertebral bone marrow in patients with gaucher disease. Radiology 1992; 182:451-455.

16. Gerard EL, Ferry JA, Amrern PC, Harmon DC, McKinstry RC, Hoppel BE, Rosen BR. Compositinal changes in vertebral bone marrow during treatment for acute leukemia: assessment with quantitative chemical shift imaging. Radiology 1992; 183:39-46.

17. Jensen KE, Jensen M, Grundtbig P, Thomsen C, Karle H, Kenriksen O. Localized in vivo proton spectroscopy of the bone marrow in patients with leukemia. Magn Reson Imag. 1990; 8: 779-789.

Chapter 3

Line Scan Spectroscopic Imaging

3.1 Introduction

In this chapter, the line scan CPMG and RARE spectroscopic imaging techniques and image analysis methods are demonstrated. This chapter is organized as follows. In Section 3.2 the target localization sequences are presented. In Section 3.3 the line scan CPMG spectroscopic imaging sequence is demonstrated. Also illustrated in this section are a k-space representation and the solution of Bloch equations that is used to explain the echo signals as the Fourier transformation image of the magnetization. Then in Section 3.4 the line scan RARE spectroscopic imaging sequence is described. This is followed by a discussion on optimizing spectral resolution, T_2 measurements and acquisition speed (Section 3.5). In Section 3.6 the importance of column selection is stated. The chapter concludes with a presentation on image post processing analysis methods (Section 3.6.)

3.2 Target Localization

The imaging protocols consist of section image localization, target column localization and spectroscopic imaging sequences. This section explains section image localization and target column localization sequences.

Section image localization is from a set of T_1-weighted section images acquired with a standard RARE sequence (TR/TE = 600/12 ms) [1], a variation of Fast Spin Echo imaging. A section image that contains most of the target tissues is selected, and location of

the image slice is recorded. For *in vivo* studies of this thesis the target tissues are bone marrow and brain. Within this section image, a target column is localized as the volume of interest. Visualization of this column is achieved with a RARE based rapid scan (TR/TE = 600/75 ms, 18 sec scan time for 128 phase encodes) [2], shown in Figure 3.1. Such scan generates a section image at the selected slice location that contains a dark band outlining the targeted tissue column.

Figure 3.1 is the pulse sequence for rapid visualization of the target column. The sequence is a standard RARE sequenc combined with a pre-saturation pulse. The selective 90° pulse along with a gradient on the readout direction prior to the RARE sequence saturates the targeted tissue column in the section image. The imaging slice is excited by the initial 90° pulse along with a slice selective gradient and refocused by the following 180° pulses along with refocusing gradients. Each echo is individually phase encoded before echo sampling and rephased after the sampling. Two spatial dimensions of the image are encoded by readout gradients and phase gradients respectively. Up to eight echoes can be collected per excitation even though only three are shown here. Eight k-space lines are acquired per TR if the 8-echo train is used.

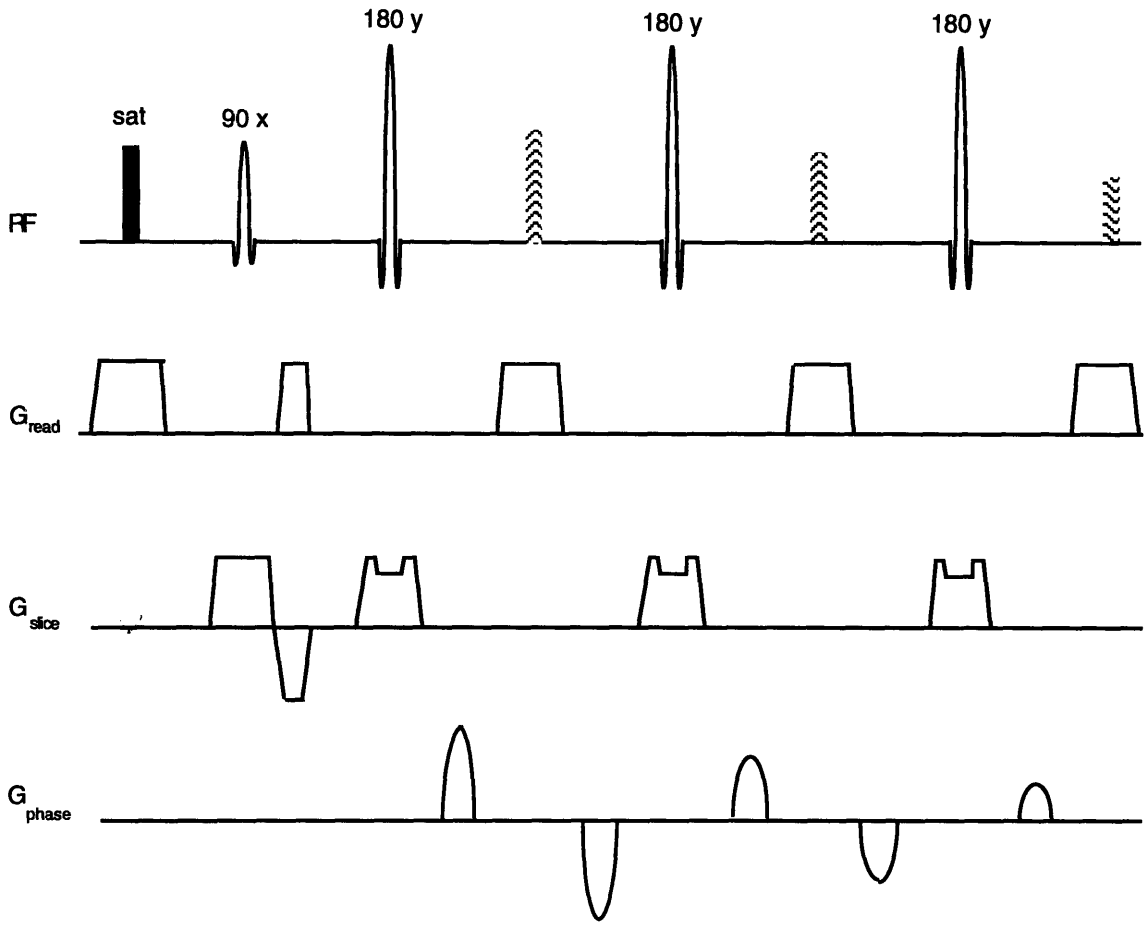

Figure 3.1: Saturation pulse added prior to RARE sequence. The SAT pulse saturates spins from selected tissue column so that the column appear as a dark band in the section image.

3.3 Line Scan CPMG Spectroscopic Imaging

3.3.1 Pulse Sequence

The line scan CPMG spectroscopic imaging sequence is presented in Figure 3.2. The initial 90°_{x} pulse, a one-side-lobe since pulse of 3 ms duration filtered with a Hamming window, along with a slice selective gradient G_{read} (maximum strength of 10 mT/m, 0.6 ms ramp) excites a plane that is orthogonal to the one refocused by the following 180°_{y}

pulses (the same as 90° except the amplitude and phase) along with slice selection gradients G_{slice}. The intersection of the two planes yields a column where the echo signals come from [2, 3]. This procedure ensured that echoes are from spins restricted to a nominally square column whose width is dictated by the RF waveforms and the maximum strength of the slice-select gradients.

Spatial information is encoded along the column, with phase-encoding gradients applied before echo readout and "unwound" after echo readout. In the dimension perpendicular to the column, instead of encoding spatial information, the spectral information is preserved without applying read gradients. Since the echoes are sampled in the absence of frequency-encoding gradients, the Fourier transformation provides the spectral information directly. The figure shows only three echoes even though up to eight can be collected per excitation. Each echo generates a spectroscopic image corresponding to different echo time.

The line scan CPMG spectroscopic imaging sequence has capacity of running in multi-slice mode, that is a series of columns can be selected one at a time. Unless specified, all experiments presented in this thesis were performed with a single column.

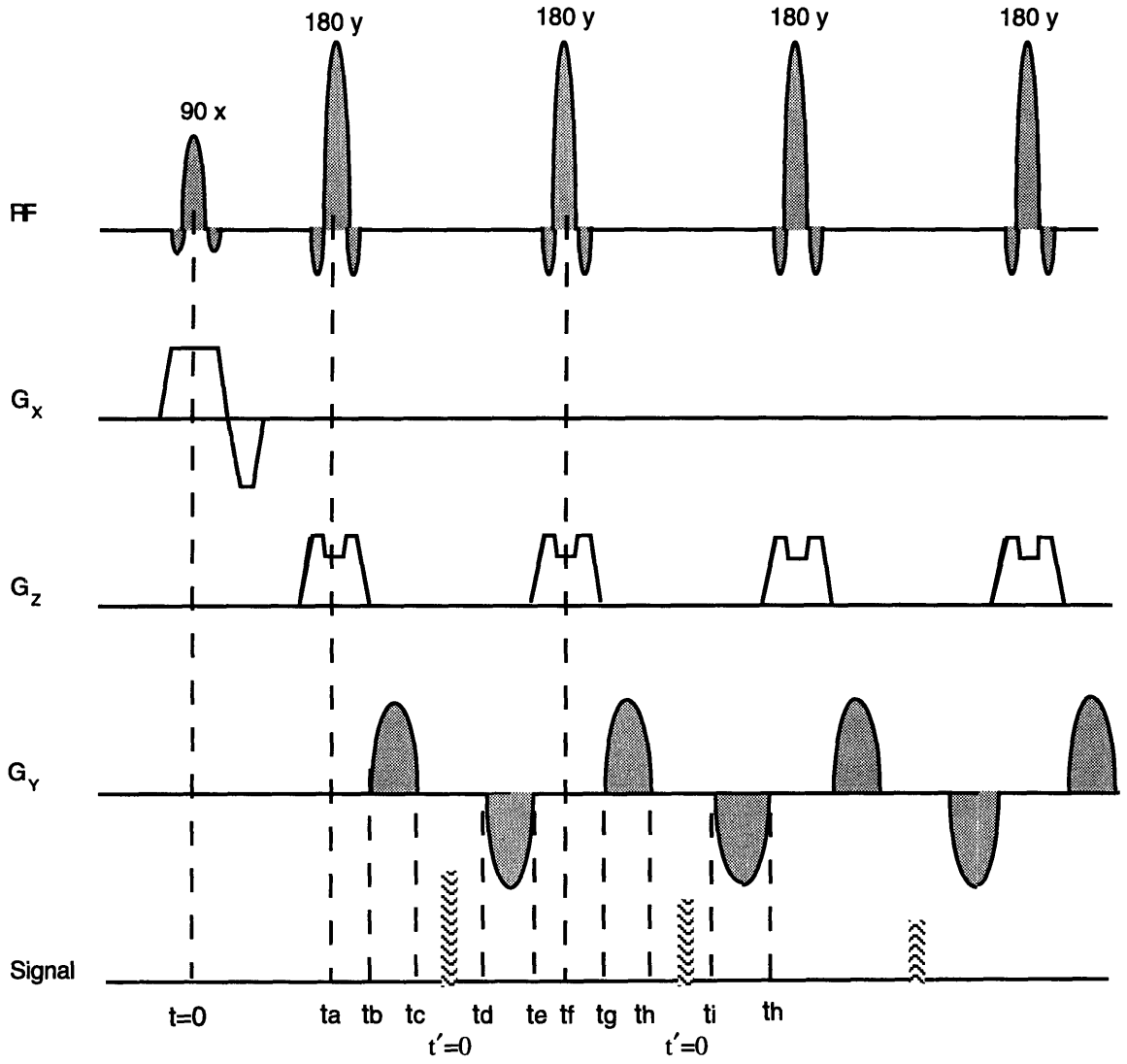

Figure 3.2 Line scan CPMG spectroscopic imaging sequence. Echoes are collected without readout gradient. In each excitation, same phase encoding gradient is used for all echoes. Only three echoes are shown.

3.3.2 Column Selection

Figure 3.3 is the schematic representation of a target column formed by the intersection of two planes, the excitation plane and the refocusing plane.

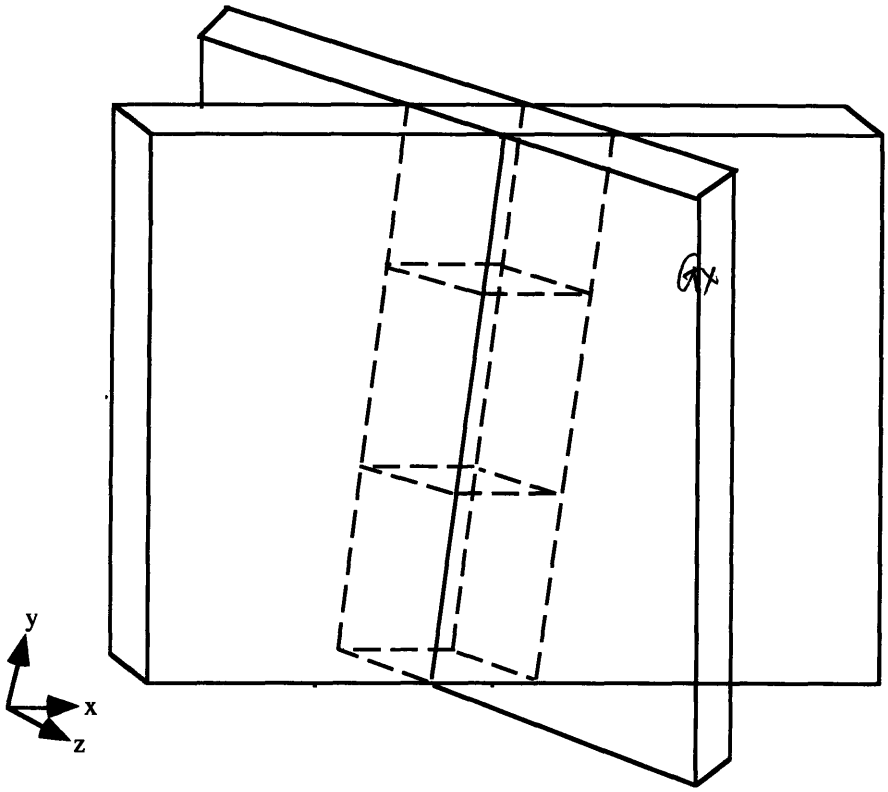

Figure 3.3: The target column is selected by intersection of 90 slice-selective plane and180 refocusing plane. The phase encoding direction is along the column.

The echo data acquired in k-space, $S(k_y, x_0, z_0, t)$, from the column can be expressed as,

$$S(k_y, x_0, z_0, t) = \iiint s(x, y, z, \delta) v(x - x_0) w(z - z_0) e^{-ik_y y - i\delta t} dx dy dz d\delta$$

where $s(x, y, z, \delta)$ is spin density distribution, and δ is chemical shift. $v(x - x_0)$ and $w(z - z_0)$ are the excitation profiles in x and z directions respectively. They are close to zero everywhere except in a narrow intervals ($\pm \Delta x$, $\pm \Delta z$) around chosen position (x_0, z_0). So the integrals on x and z can be approximated,

$$\iint s(x, y, z, \delta) v(x - x_0) w(z - z_0) dx dz$$
$$\cong \int_{x_0 - \Delta x}^{x_0 + \Delta x} \int_{z_0 - \Delta z}^{z_0 + \Delta z} s(x, y, z, \delta) dx dz$$

The column position is determined by center frequencies of the 90°_{x} and 180°_{y} pulse envelopes, as well as the strength of slice selective and refocusing gradients. Assume the central frequencies for the 90°_{x} and 180°_{y} pulses are $\omega_0 + \Delta\omega_{90}$ and $\omega_0 + \Delta\omega_{180}$ respectively with ω_0 being resonance frequency, and let the slice-selective gradient be on x direction and refocusing gradient on z direction, the column position (x_0, z_0) is decided by:

$$x_0 = \frac{\Delta\omega_{90}}{\gamma G_x}, \quad z_0 = \frac{\Delta\omega_{180}}{\gamma G_z}$$

For a given gradients, changing the central frequencies of the 90°_{x} and 180°_{y} pulses allows reposition of the column. On-line column position is performed by changing two control variables that are related to the RF frequencies. Also utilized on-line is an algorithm that ensures the phase difference between 90°_{x} and 180°_{y} pulses remains the same whenever the RF frequencies have changed.

3.3.3 Fourier Transformation Representation

The line scan spectroscopic CPMG images can be understood as follows: One dimension is spatial and another is chemical shift (or spectral). Observe a transverse magnetization m(x, y, z, δ, t) or m(y, δ, t) since the dependence on x and z has been reduced by column configuration (Figure 3.3). Let δ be the spectral variable and B′(y, δ) represent field B_0 inhomogeneity and susceptibility. T_2 relaxation is ignored for the time being. Now follow the magnetization at different timing in the pulse sequence of Figure 3.2:

$t = 0^+$: m(y, δ, 0)

$t = t_a^-$: m(y, δ, 0) $e^{-i\gamma B' t_a} e^{-i\delta t_a}$

$t = t_a^+$: m(y, δ, 0) $e^{i\gamma B' t_a} e^{i\delta t_a}$, (spin flipped 180°)

$$t = t_b:\ m(y, \delta, t_a^+)\, e^{-i\gamma B'(t_b - t_a)}\, e^{-i\delta(t_b - t_a)}$$
$$= m(y, \delta, 0)\, e^{-i\gamma B'(t_b - 2t_a)}\, e^{-i\delta(t_b - 2t_a)}$$
$$t = t_c:\ m(y, \delta, t_b)\, e^{-i\gamma B'(t_c - t_b)}\, e^{-i\delta(t_c - t_b)}\, e^{-i\gamma y\int G_y d\tau}$$
$$= m(y, \delta, 0)\, e^{-i\gamma B'(t_c - 2t_a)}\, e^{-i\delta(t_c - 2t_a)}\, e^{-i\gamma y\int G_y d\tau}$$
$$= m(y, \delta, 0)\, e^{-i\gamma B'(t_c - TE)}\, e^{-i\delta(t_c - TE)}\, e^{-i\gamma y\int G_y d\tau}$$
$$t_c < t < t_d:\ m(y, \delta, t_c)\, e^{-i\gamma B'(TE - t_c + t')}\, e^{-i\delta(TE - t_c + t')}$$
$$= m(y, \delta, 0)\, e^{-i\gamma B' t' - i\delta t' - i\gamma y\int G_y d\tau}$$

The total signal is the sum from all the magnetization from the entire column:

$$s(G_y, t') = \int s(y, \delta, 0)\, e^{-i\gamma B' t' - i\delta t' - i\gamma y\int G_y d\tau}\, dy d\delta$$

where $s(y, \delta, 0)$ is proportional to $m(y, \delta, 0)$. Define $k_y = \gamma\int G_y d\tau$, and reintroduce T_2 relaxation term, the signal for the first echo is given by:

$$s(k_y, t') = \int s(y, \delta, 0) e^{-i\delta t - ik_y y} e^{-i\gamma B' t'} e^{-i(TE + t')/T_2} dy d\delta$$

noticed that at $t' = 0$, the field inhomogeneity gets refocused, so the inhomogeneity term disappears. At times after the first echo,

$$t = t_e:\ m(y, \delta, t_d)\, e^{-i\gamma B'(t_e - t_d)}\, e^{-i\delta(t_e - t_d)}\, e^{i\gamma y\int G_y d\tau}$$
$$= m(y, \delta, 0)\, e^{-i\gamma B'(t_e - TE)}\, e^{-i\delta(t_e - TE)}$$
$$t = t_f^-:\ m(y, \delta, t_e)\, e^{-i\gamma B'(t_f - t_e)}\, e^{-i\delta(t_f - t_e)}$$
$$= m(y, \delta, 0)\, e^{-i\gamma B'(t_f - TE)}\, e^{-i\delta(t_f - TE)}$$
$$t = t_f^+:\ m(y, \delta, 0)\, e^{i\gamma B'(t_f - TE)}\, e^{i\delta(t_f - TE)},\ \text{(spin flipped 180°)}$$

$$t = t_h:\ m(y, \delta, t_f^+)\, e^{-i\gamma B'(t_h - t_f)}\, e^{-i\delta(t_h - t_f)} e^{-i\gamma y \int G_y d\tau}$$

$$= m(y, \delta, 0)\, e^{-i\gamma B'(2t_f - t_h - TE)}\, e^{-i\delta(2t_f - t_h - TE)} e^{-ik_y y}$$

$$t_h < t < t_i:\ m(y, \delta, t_h)\, e^{-i\gamma B'(2TE - t_h + t')}\, e^{-i\delta(2TE - t_h + t')}$$

$$= m(y, \delta, 0)\, e^{-i\gamma B' t' - i\delta t' - ik_y y}\ ,\ (2t_f = 3TE)$$

By inserting the T_2 relaxation, the signal for the second echo is given by:

$$s(k_y, t') = \int s(y, \delta, 0) e^{-i\delta t - ik_y y} e^{-i\gamma B' t'} e^{-i(2TE + t')/T_2} dy d\delta$$

This procedure can be repeated for the following echoes. In general, the n-th echo data acquired can be expressed as:

$$S(k_x, k_y, k_z, t) =$$

$$\iiint \int s(x, y, z, \delta) v(x - x_0) w(z - z_0) e^{-i\delta t} e^{-ik_y y} e^{-igB' t} e^{-i(t + nTE)/T_2} dx dy dz d\delta$$

where $v(y - y_0)$ and $w(z - z_0)$ are the excitation profiles in x and z directions respectively. Direct inverse Fourier transformation of $S(k_x, k_y, k_z, t)$ would give T_2 weighted spectroscopic image.

3.3.4 Sampling in k-Space

Figure 3.4 illustrates how a CPMG spectroscopic image is acquired in k-space, the Fourier space of $S(y, \delta)$. In an excitation, a phase gradient G_y is turned on to encode k_y before signal acquisition. A signal line in k-space is sampled from t_{min} to t_{max} without the read gradient. The sampling time equals (t_{max}-t_{min}). A reversed phase gradient (-G_y) is applied to "unwound" the phase. At the end of a TR period, G_y changes to a new value and sequence is repeated. Each k-space line is an echo from the column.

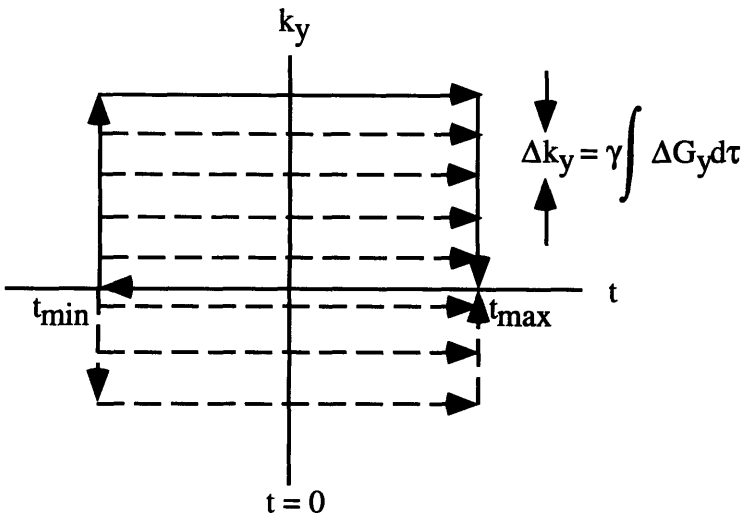

Figure 3.4: k-space representation of signal acquisition with CPMG. Each k-line corresponds an excitation with a distinct phase encodes. The whole k-space is sampled sequentially. The solid line represents the first phase encoding step, and the dashed lines (from top to bottom) correspond the second, third, ... , phase encoding steps.

Let ΔG_y be the step change between phase encodes, and Δk_y be the step change in the consecutive k-space lines. The field of view (FOV) of phase encoding direction is decided by $1 / \Delta k_y$, and the spectral resolution is determined by sampling time or $1 / (t_{max} - t_{min})$.

3.4 Line Scan RARE Spectroscopic Imaging

3.4.1 Pulse Sequence

The pulse sequence for the line scan RARE spectroscopic imaging is presented in Figure 3.5. The column is selected by two orthogonal planes, one is excited by the 90° pulse and another is refocused by the 180° pulses. Phase encoding is along the column.

Each echo is individually phased encoded before acquisition, and sampled without the readout gradients.

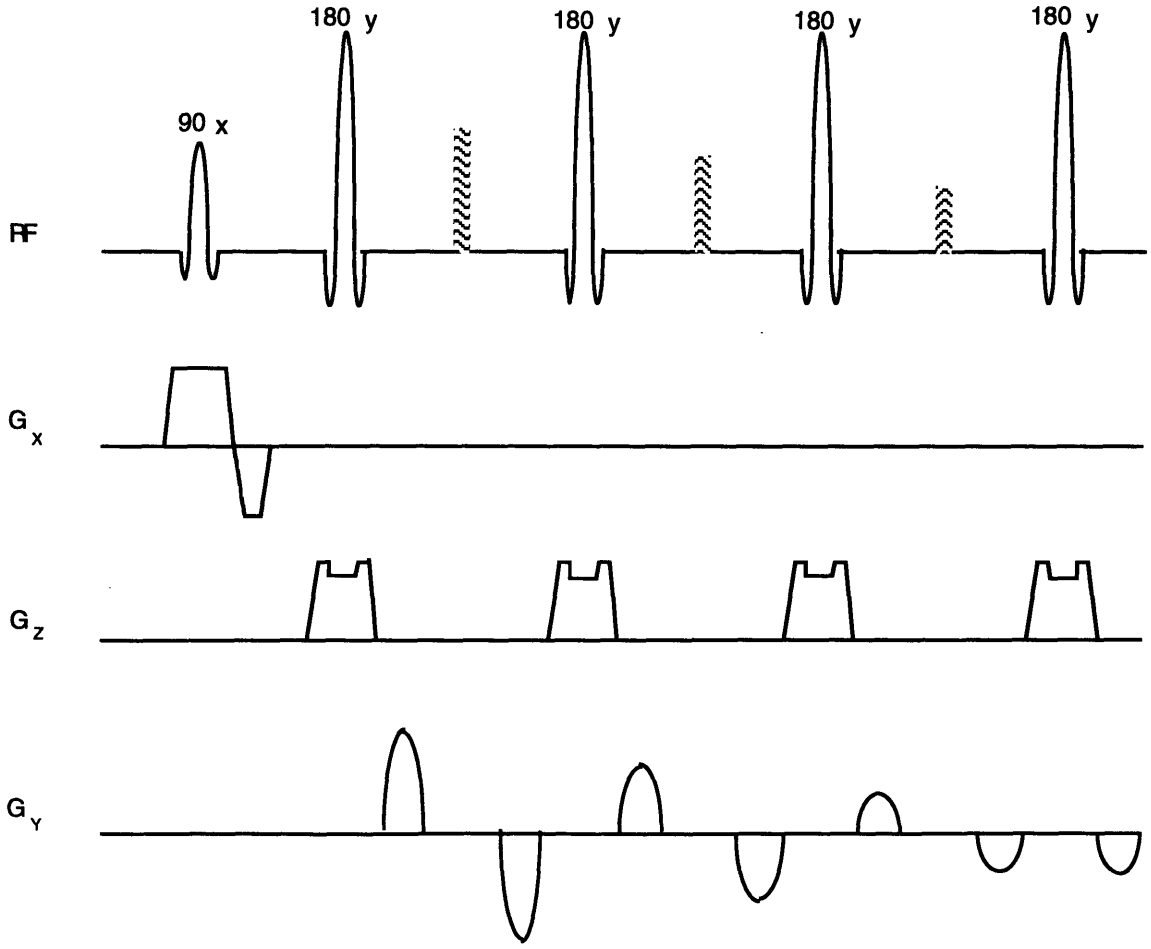

Figure 3.5: Line scan RARE spectroscopic imaging sequences. The 90 pulse along with selective gradient excites a plane that is orthogonal to the plane refocused by 180 pulses. Each echo is individually phase encoded before echo sampling and "unwound" after the sampling. The echoes are acquired without readout gradients.

3.4.2 T2 Weighting

Echoes acquired with large values of phase encoding gradients yield high frequency components in the reconstructed image. However, these echoes suffer the substantial spin

dephasing, and are much smaller in amplitude than echoes associated with the small phase encode gradients. The largest absolute value of phase gradient K_{max} is decided by FOV and the number of pixels in phase direction N_p. The Nyquist criterion gives [1]:

$$|K_{\max}| = \frac{\pi N_p}{FOV}$$

The effective TE of RARE sequence is given by the time delay between the initial excitation and the collection of the zero phase echo. So the T_2 weighting can be manipulated by changing the order of the phase encode. Figure 3.6 shows some scheme of the phase encoding. The horizontal axis represents the sampling from $-K_{max}$ to K_{max} and the vertical axis represents the relative T_2 weighting for each phase encoding step. In (a) the zero phase occurs midway through the sampling cycle. The effective TE for this chronological sweep is $N_p\tau$ where 2τ is the echo spacing. (b) shows one way to reduce T_2 weighting by rotating zero-phase-step forward in time. However, the method creates a large step change during the sampling that may result in a rippling artifact. To avoid this, alternatives are shown in (c) and (d). In (c) the smallest phase-encode values are on early echoes , and alternating positive and negative phase encoding are from one echo to another. In (d) the 2-shot RARE requires two excitations, one for acquiring the positive K_y and the other for the negative K_y. The phase encoding scheme in (a) is limited to mapping long T_2 species. The methods of (b, c, d), the signal intensities from short T_2 species can be greatly enhanced over that obtained with (a).

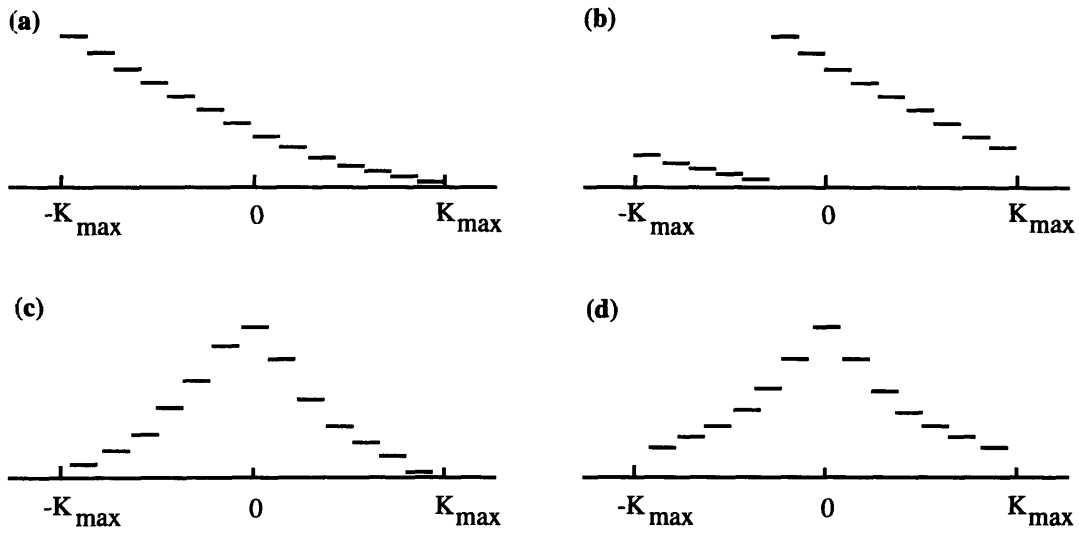

Figure 3.6. Scheme of phase encode from $-K_{max}$ to K_{max}. The vertical axis represents the relative T_2 weighting at each phase encode step. **(a):** Zero phase occurs midway through the sampling cycle. **(b):** Circularly rotating the zero phase forward in time. **(c):** Shuffling the phase encodes between odd and even echoes. **(d):** Two-shot RARE method for phase encoding.

3.5 Optimization of Spectral Resolution, Relaxation Measurements and Acquisition Speed

In Fourier theories, the sampling time is inversely proportional to the spectral resolution. To achieve high spectral resolution in spectroscopic imaging, one wants to use long readout window for spectral signals. However, the long sampling window lengthens the echo spacing, which in turn increasing the echo signal decay due to the T_2 relaxation. In addition, the prolonged TE increases the T_2 weighting in the RARE imaging, and decreases the signal-to-noise ratio for later echoes that are required for T_2 relaxation time measurements in the CPMG imaging. In designing spectroscopic imaging sequences, trade-offs on spectral resolution, relaxation measurements and speed have to be made.

The line scan CPMG spectroscopic imaging sequence is designed for spectral T_2 measurements with variable spectral resolutions. The acquisition filters that offer variable of echo readouts are 32, 64, 96, 128, 160, 192, 217 ms with 128 sampling points, which correspond to apparent spectral resolution of 16, 8, 5, 4, 3.2, 2.6, 2.3 Hz respectively. For example, a 32 ms signal readout provides the image with a spectral resolution of 32 Hz (128 samples with 250 μsec sampling interval). The procedures of zero-filling the raw data from 128 sampling points to 256 and performing FFT yield an apparent 16 Hz spectral resolution. The CPMG spectroscopic sequence trades spectral resolution for spectral T_2 measurements.

The line scan RARE spectroscopic imaging sequence is designed to perform rapid spectral mapping with the variable spectral resolutions. The optional acquisition filters are the same as in the CPMG spectroscopic imaging. The effective TE can be manipulated by choosing different echo train length and phase encodes. The speed is determined by the number of echoes used per excitation. The scan time for a seven-echo-train is 7-fold less than what is needed for the CPMG acquisition. The RARE spectroscopic sequence trades spectral T_2 measurements for acquisition speed.

In both CPMG and RARE spectroscopic imaging, the duration of echo readout window places a limit on the minimum echo spacing. For instance, a 32 ms echo read needs a minimum 48 ms echo spacing to accommodate the RF pulses, the gradients, and the sampling window while a 128 ms readout window requires a minimum TE of 145 ms. High spectral resolution can be achieved by applying acquisition filter of long echo sampling at the expenses of large echo spacing. Control variables such as echo spacing and echo sampling filter can be selected on-line to balance the spectral resolution, T_2 measurements and speed for specific applications.

3.6 The Significance of Column Selection

It is well known that the bone marrow is abundant in long bones, such as in cervical, thoracic and lumbar spine in upper extremity, and femur and tibal in lower extremity. The column localization scheme is an efficient way to probe bone marrow in the long bones. The use of orthogonal 90° and 180° slice-selective RF pulses to select a column is very important in practical sense. It reduces the dimensions of spectroscopic interrogated voxels to the point at which meaningful spectra from restricted anatomy can be obtained. It also speeds up the acquisition process so that the line scan techniques are very applicable as a clinical tools.

The CPMG spectroscopic imaging sequence in Figure 3.2 can be extended to 2-D chemical shift CPMG sequence. Instead of targeting a column, an image plane can be selected by using 90°-180°pulses combined with slice selective gradient and refocusing gradients. The 2-D spatial information can be encoded by phase gradients along G_X and G_Y directions. Such modification would increase the volume coverage and generate 2-D chemical shift images of different TE at the expenses of imaging scan time.

3.6 Image Analysis

For each spectroscopic imaging scan, raw data were acquired and reconstructed into magnitude image on the Signa scanner. The spectroscopic images were transferred to a SPARC 2 workstation (Sun Microsystems, Mountain View, California.) for further analysis. An automated imaging post-processing program was used to extract and fit spectra from each individual voxel of the images. The flow chart of this automated program is shown in Figure 3.7.

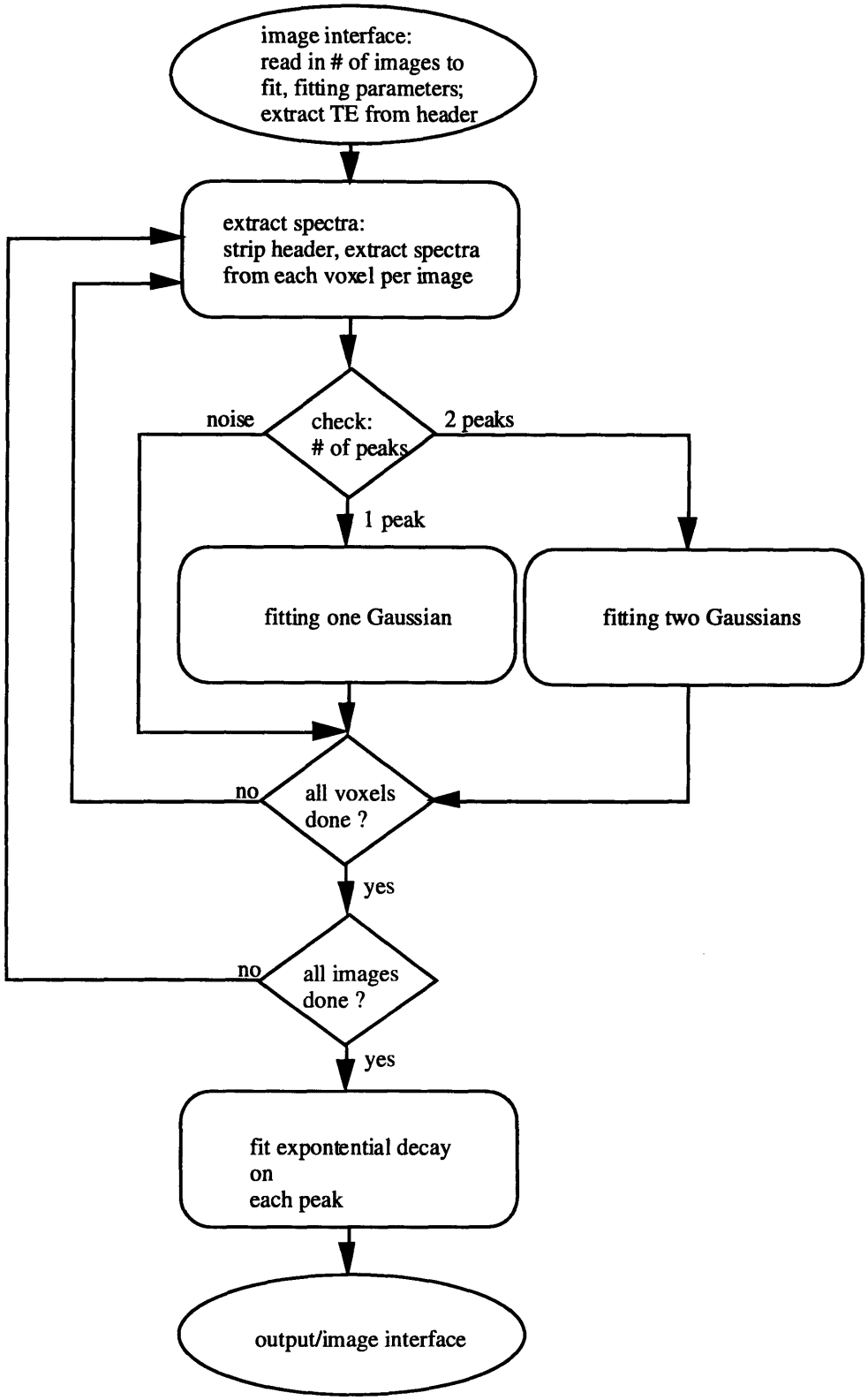

Figure 3.7: Flow chart of the automated image processing/fitting program

The spectra were fitted with Gaussian functions instead of Lorentzian functions because the experimental data are better fitted with Gaussian than with Lorentzian [4, 5]. This can be attributed to magnitude reconstructed image and unresolved overlapping resonance peaks. Assume the envelope of echo signal is a Gaussian function:

$$f(t) = ae^{i\varphi}e^{-t^2/2\sigma^2+i\omega_0 t}$$

and its Fourier transform is:

$$F(\omega) = ae^{i\varphi}\int_{-\infty}^{+\infty} e^{-i(\omega-\omega_0)t}e^{-t^2/2\sigma^2}dt$$

$$= ae^{i\varphi}e^{-\sigma^2(\omega-\omega_0)^2/2}\int_{-\infty}^{+\infty} e^{-[t+i\sigma^2(\omega-\omega_0)]^2/2\sigma^2}dt$$

$$= a\sigma e^{i\varphi}\sqrt{2}e^{-\sigma^2(\omega-\omega_0)^2/2}\int_{-\infty}^{+\infty} e^{-x^2}dx$$

$$= \sqrt{2\pi}a\sigma e^{i\varphi}e^{-\sigma^2(\omega-\omega_0)^2/2}$$

The magnitude spectrum is:

$$M(\omega) = \sqrt{2\pi}a\sigma e^{-\sigma^2(\omega-\omega_0)^2/2}$$

Identifiable peaks within the spectra were fit with Gaussian line shapes using a Marquardt non-linear least square algorithm. The spectra of early echoes were fitted with double peak Gaussian functions of the form:

$$I(\omega) = A\, e^{-(\omega-\omega_{0A})^2/\sigma_A^2} + B\, e^{-(\omega-\omega_{0B})^2/\sigma_B^2} \qquad [1]$$

where A and B are peak amplitudes, σ_A, σ_B are linewidths, and ω_A, ω_B are central peak frequencies. When T_2 relaxation made peaks too small to identify in later echoes, a single Gaussian function was used to fit the remaining peak. Peak area, termed as S, under each spectrum was numerically calculated by trapezoidal integrals using fitted parameters, A, B, $\sigma_A, \sigma_B, \omega_A$ and ω_B. The spectral peak area S, as a function of TE, were fitted with mono-exponential function of the form:

$$S = S_0 e^{-TE/T_2} \qquad [2]$$

where S_0 is the extrapolated peak area at TE = 0, and T_2 is the transverse relaxation time. S_0 is proportional to spin density, and the proportional constant depends on the hardware of scanner. In case where absolute spin density is needed, the data could be calibrated using an additional phantom that contains materials with known concentration. For simplicity, the relative concentrations are calculated in this thesis. The relative concentrations for spectral peak A and B are calculated from peak areas S_{0A} and S_{0B} by:

$$A\% = \frac{S_{0A}}{S_{0A} + S_{0B}} \times 100\%, \quad B\% = \frac{S_{0B}}{S_{0A} + S_{0B}} \times 100\%$$

When more than 2 peaks exist in the spectra, as in the case of knee study where vinyl, water, methylene and methyl proton appear, the fitting program was applied on two peaks at a time. After the absolute peak areas were computed, the relative concentration for each peak was calculated by

$$A\% = \frac{S_{0A}}{S_{0A} + S_{0B} + S_{0C} + S_{0D}} \times 100\%$$

where S_{0A} , S_{0B} , S_{0C} and S_{0D} are extrapolated areas for peak A, B, C and D respectively.

References

1. Mulkern RV, Wong STS, Winalski C, Jolesz FA. Contrast Manipulation and artifact assessment of 2D and 3D RARE sequences. Magn Reson Imag 1990; 8: 557-566.

2. Oshio K, Mulkern RV. Rapid fat/water assessment in knee cavity bone marrow by inner volume spectroscopic imaging with RARE. JMRI 1992; 2: 601-604.

3. Feinberg DA, Hoenninger JC, Crooks LE, Kaufman L, Watts JC, Arakawa M. Inner volume MR imaging: technical concepts and their application. Radiology 1985; 156: 743-747.

4. Mulkern RV, Meng J, Oshio K, Williamson DS, Lilly HS, Guttmann CRG, Jaramillo D. MRS imaging of the knee with line scan CPMG sequences. J. Computer Assisted Tomography 1995; 19(2): 247-255.

5. Mulkern RV, Meng J, Oshio K, Guttmann CRG, Jaramillo D. Bone marrow characterization in the lumbar spine with inner volume spectroscopic CPMG imaging studies. JMRI 1994; 4: 585-589.

Chapter 4

Applications: Relative Concentrations and Spectral Spin-Spin Relaxation in Bone Marrow

4.1 Introduction

Recall that in Chapter 3 the line scan CPMG and RARE spectroscopic imaging techniques are described, as well as image analysis methods. The techniques were developed and implemented on a conventional 1.5 T MRI scanner with standard hardware and software configuration. In this chapter the applications of the techniques are demonstrated. First, the techniques are tested on a phantom that consists of different mixtures of agar and mayonnaise, and the MR measurements on the phantom are evaluated. Second, some fundamental concepts about bone marrow that are relevant to the applications of the techniques are stated. Third, the techniques are applied *in vivo* on bone marrow in lumbar spine. The vertebral marrow studies focus on quantification of fat and water. Fourth, the techniques are demonstrated on developing bone marrow in knee. The knee marrow studies concentrate on characterization of red and yellow marrow with the potential to monitor conversion of red marrow to yellow marrow by quantifying not only the water proton but smaller lipid proton peaks as well. The spectroscopic images are analyzed to map relative spectral concentrations and T_2 relaxation times.

This chapter is organized as follows. In Section 4.2 the phantom experiment is presented. In Section 4.3 fundamentals about bone marrow are introduced. Then the vertebral marrow quantification in lumbar spine is described in Sections 4.4. It is followed

by a study on developing bone marrow in knee in Section 4.5. This chapter concludes with a discussion in Section 4.6.

4.2 Phantom Experiment

To prove the capability of the techniques for fat/water percentages, a phantom of 5 vials with various mixtures of agar and mayonnaise were prepared to test correlation of MR measured fat/water percentages [1]. The experiment was performed with a clinical 1.5 T GE Signa Imager with the 4.x hardware and software configurations (General Electric Medical Systems, Milwaukee, Wisconsin). The sequence was used in multi-slice mode to spectroscopically interrogate the phantom. Five columns with 192 phase encode steps each and TR of 2 seconds were acquired in 6 minutes and 24 seconds. The column clearly containing all five vials was used for spectral post-processing.

In the phantom study of 5 vials with different mixtures of agar gel and mayonnaise, the pure mayonnaise was found to be 81% fat by the MR measurement. Figure 4.1 is a plot of the MR measured fat percentage versus that calculated based on weight percentages of mayonnaise and agar, assuming fat is 81% in pure mayonnaise and 0% in agar. The correlation found between MR measured fat percentage and that calculated on a weight percentage basis is given by the following equation,

$$\text{Fat }\%(\text{MR}) = 0.998 \times \text{Fat(Weight)} + 0.70$$

with a correlation coefficient of 0.998.

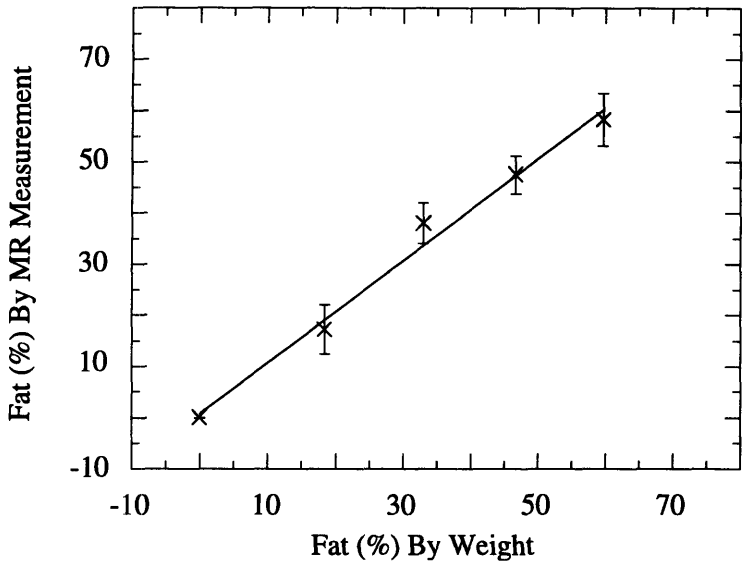

Figure 4.1. Fat percentage measurement of a phantom with different mixtures of agar and mayonnaise. Horizontal axis is calculated by weight and vertical axis is measured by MR method described in the text. The solid line is the best linear fit.

4.3 Bone Marrow Fundamentals

The purpose of this section is to present some background about bone marrow and the biological basis relevant to this thesis. In the latter sections, the applications of the line scan techniques to human bone marrow *in vivo* are demonstrated. This section contains bone marrow anatomy and function, red to yellow marrow conversion, and marrow disorders [2-4].

4.3.1 Anatomy and Function

Bone marrow is one of the largest and most important organs of the body within the confines of the human skeleton. Except for bone, muscle, and fat, it is the largest organ of the body by weight, approaching 3000 g in adult man and approximately 2600 g in women. Its function is to provide a continual supply of red cells, platelets, and white cells to meet the body's demands for oxygenation, coagulation and immunity.

The basic micro structure of bone marrow consists of a trabecular framework housing fat cells covered with hematopoietic cells both supported by a system of reticulum cell nerves and vascular sinusoids coursing among them. Fat cells are a major component of bone marrow. These cells, however, differ from those at other locations in the body. From animal studies it is known that marrow fat cells are smaller in size than those from extramedullary sites. Despite their smaller size, the marrow fat cells display the same metabolic activity. The size of these cells appears to be responsive to hematopoietic activity. During periods of decreased hematopoiesis, fat cells increase their volume and number, while during increased hematopoiesis the fat cells atrophy. The diversity and complexity of the various anatomic, physiologic and biochemical constituents of bone marrow may be simplified by the unifying concept of a balanced red and yellow marrow distribution.

4.3.2 Red and Yellow Marrow

"Red marrow" is considered hematopoietically active marrow involved in the production of red cells, white cells and platelets. "Yellow marrow" is considered hematopoietically inactive. Yellow marrow is composed predominantly of fat cells and has an aggregate weight of approximately 1500 g in adult man and 1300 g in adult women, thus accounting for roughly half the total bone marrow weight. Although red marrow accounts for the other half of total marrow weight, of that marrow classified as red, half is adipose tissue. Thus, about three-quarters of adult total bone marrow is composed of fat

cells. Red marrow fat cells may contain slightly greater concentrations of unsaturated fatty acids.

The chemical composition and vascular supply of the two types of marrow differ in important ways. Red marrow contains approximately 40% water, 40% fat, and 20% protein, while yellow marrow contains approximately 15% water, 80% fat, and 5% protein. The vascular network of red marrow can be viewed as being rich and arborized, while that of yellow marrow is more sparse.

Conversion of red to yellow marrow occurs during growth and development and has a predictable and orderly pattern. At birth virtually the entire fetal marrow space is dedicated to hematopoietic (red) marrow. In the immediate postnatal period, conversion from red to yellow marrow begins and is first evident in the extremities, like hands and feet. This conversion progresses from peripheral (appendicular) toward central (axial) with respect to the skeleton as a whole and from diaphyseal to metaphyseal in individual long bones. By the time a person is 25 years old, marrow conversion is usually complete and the adult pattern is achieved. At this time, red marrow is predominantly concentrated in the axial skeleton (skull, vertebrae, ribs, pelvis) and to a lesser degree in the proximal portions of the appendicular skeleton (proximal femora and humeri). The yellow marrow is mainly concentrated at skeleton from lower extremity (distal femora, tibia, fibula).

4.3.3 Bone Marrow Disorders

Various diseases that affect bone marrow reveal certain common pathophysiologic patterns. These patterns can be broadly classified into five groups.

The first pattern or pathophysiologic mechanism is reconversion, that is yellow marrow is recruited for red marrow production. It is reversal of normal marrow conversion. The reason could be that the individual's demand for hematopoiesis exceeds the ability of existing red marrow, a conversion of yellow to red marrow is initiated. The

causes vary from anemia to marrow replacement disorders (metastatic disease, myeloma, myelofibrosis, etc.).

The second category is marrow infiltration or replacement, that is the normal marrow cells are replaced with tumor cells. Leukemia, lymphoma, metastases and primary bone tumors such as osteosarcoma, Ewing sarcoma and multiple myeloma are some examples. Tumor cells have long T_1 values and variable T_2 values. T_1 and T_2 have been measured and characterized for a spectrum of infiltrate diseases. In cases of childhood leukemia, T_1 relaxation values seem to be helpful in documentation of new disease, relapse and remission.

The third group is myeloid depletion, that is all cells except fat cells disappear. Myeloid elements (hematopoietic cells) are depleted. It is the opposite of cellular proliferation. The marrow becomes predominantly fatty in nature. The processes include aplastic anemia, radiation therapy and chemotherapy.

The fourth pattern is bone marrow edema. It is vascularly mediated, and resulted in excess water in tissue. Several conditions (trauma, stress, reflex sympathetic dystrophy) seem cause edema. The stimulus and controlling factors are not certain; however, it is postulated that extracellular water increases and this is somehow modulated through control of hypervascularity or hyperperfusion.

The fifth category is bone marrow ischemia, that is the opposite of edema. It may result in subarticular osteonescrosis or metadiaphyseal bone infarction. The manifestations of the process are a balance of progressive cell death and host response through repair. Most vulnerable to the ischemia are the hemaopoietic cells which die in the first 6-12 hours following the ischemic insult. Fat cells appear most resistant to ischemia, surviving for 2-5 days.

4.4 Vertebral Marrow Quantification in Lumbar Spine

4.4.1 Introduction

The objective of this section is to demonstrate the line scan CPMG spectroscopic imaging method as an efficient and non-invasive way to characterize water and saturated fat in vertebral marrow. Spectroscopic images from a column in lumbar spine are acquired. The spectra suitable for fat and water peak area integration from many small voxels throughout the extensive region of vertebral marrow are collected and post processed. The relative concentrations of water and fat, and their spectral T_2 relaxation values are calculated. Spectral T_2 values for water and saturated-fat are mapped along the spine [5].

4.4.2 Materials

Experiments were performed with a clinical 1.5 T GE Signa scanner. A quadrature body coil was used for transmitting and a surface "array" coil positioned beneath the lumbar spine was used for signal reception.

Six healthy adult volunteers participated in the lumbar spine experiments. The mean age ($\pm$ standard deviation) is 33 ($\pm$ 7) years. A total of 128 phase encode steps and a 2 sec TR were used. Two signal average per excitation was used to improve signal-to-noise ratio and to allow for the use of the no-phase-wrap option. The acquisition time was 4 minutes 18 seconds for one acquisition and 8 minutes 36 seconds for two. The column area was 5×5 mm^2, and the column length was 32 cm for all the experiments. These resulted in a voxel size of $5 \times 5 \times 2.5$ mm^3.

4.4.3 Results

(a)

(b)

Figure 4.2. (a): A 5 mm slice sagittal image of the spine of a healthy 31-year-old man. **(b):** The same slice with a vertical dark band representing the target column.

(c)

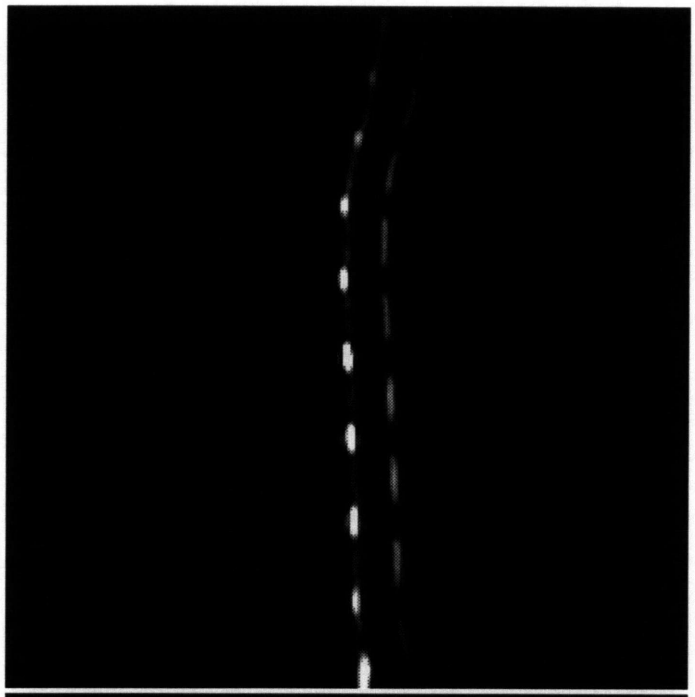

(d)

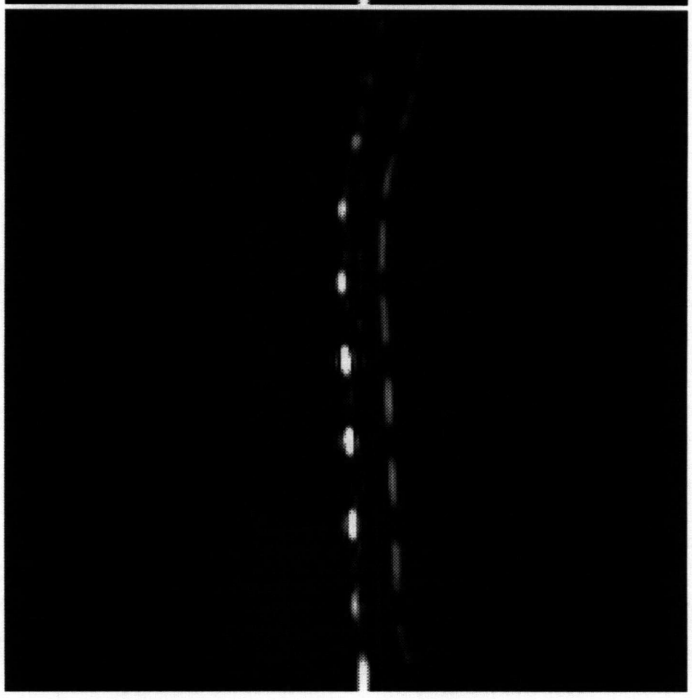

Figure 4.2. (c): Spectroscopic image (first echo) of the column obtained at a TE of 48 ms. The spectroscopic axis is horizontal, and the water signal appears to the left of the saturated fat proton signal **(d):** Spectroscoic image (second echo) at TE of 96 ms.

(c)

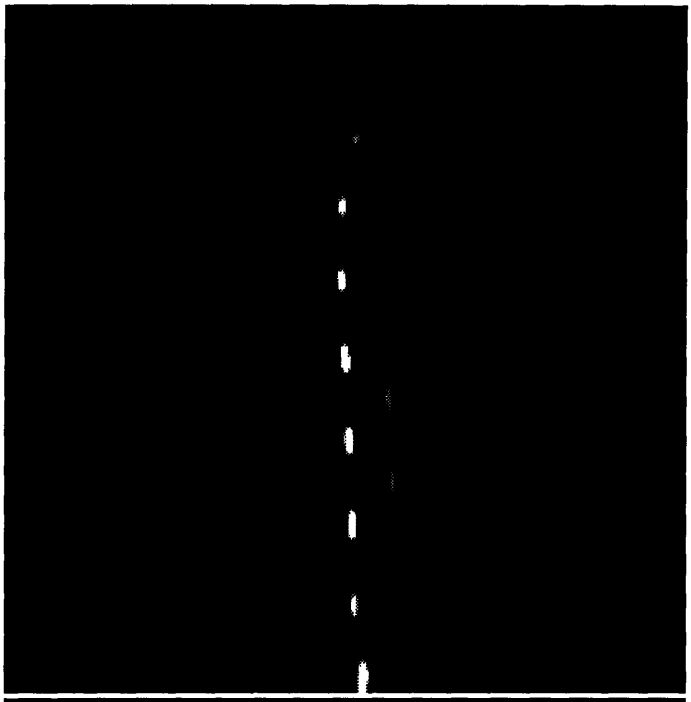

(d)

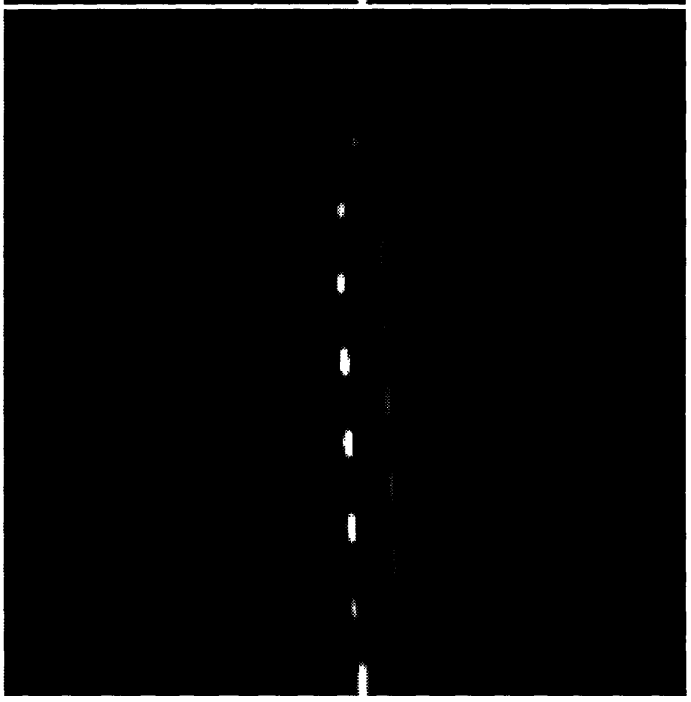

Figure 4.2. (c): Spectroscopic image (first echo) of the column obtained at a TE of 48 ms. The spectroscopic axis is horizontal, and the water signal appears to the left of the saturated fat proton signal **(d):** Spectroscoic image (second echo) at TE of 96 ms.

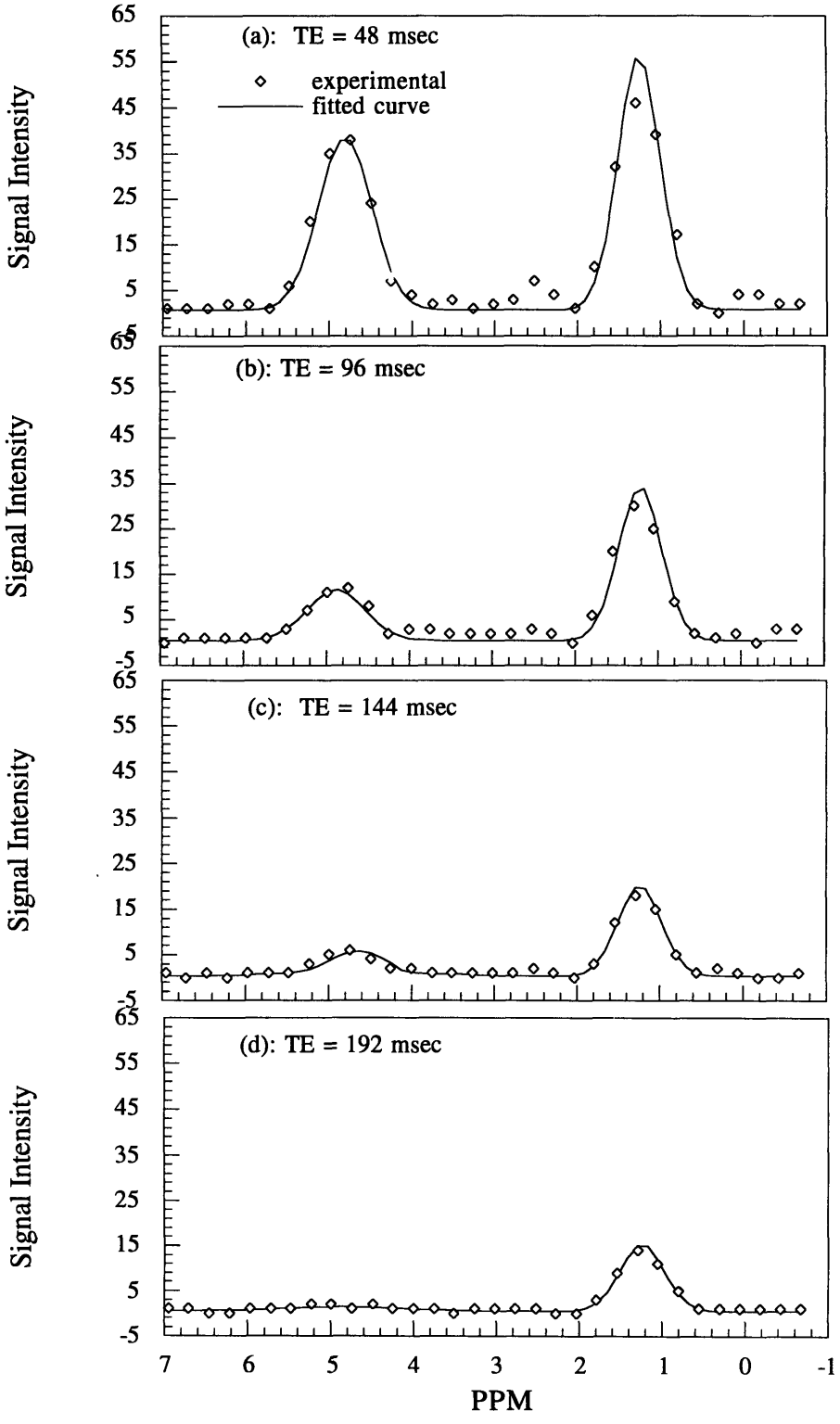

Figure 4.3: Vertebral bone marrow spectra as a function of TE values of 48 ms (**a**), 96 ms (**b**), 144 ms (**c**) and 192 ms (**d**). The water peak is around 4.8 ppm and saturated fat (methylene) peak appears around 1.2 ppm. Solid lines are the best fits to the two-peak Gaussian function.

The decays of the water and saturated fat proton peak areas with TE are shown in Figure 4.4, along with theoretical fits of the data to monoexponential function given by Equation [2].

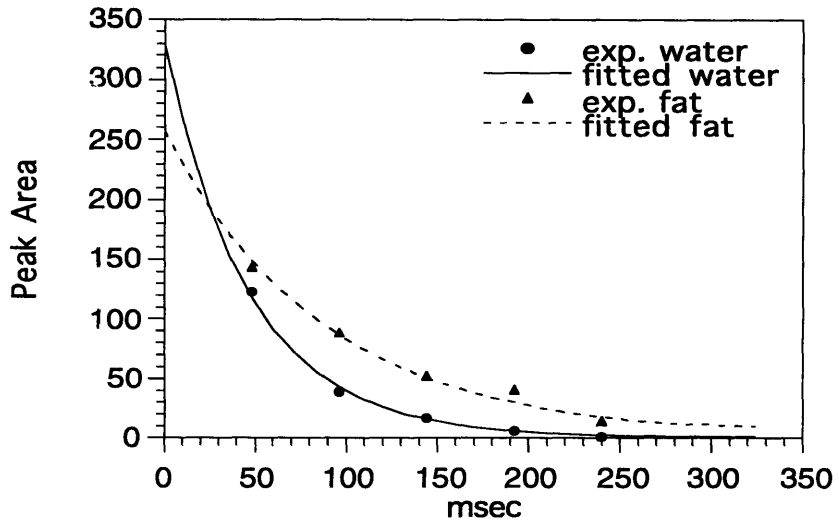

Figure 4.4 T2 decay curve of saturated-fat and water protons calculated from peak area quantification at different TEs. Also shown are least square fits of the data to monoexponential function.

From five of the six spine studies performed in healthy adult volunteers, 20-40 spectra from bone marrow per study were identified and analyzed. The results are summarized in Table 4.1, which gives the mean spectral T_2 values and relative fat and water contents obtained for each individual, along with the inter-individual mean values. The difference between the overall mean marrow water T_2 (71 ms $\pm$ 14) and the saturated fat proton T_2 (113 ms $\pm$ 21) is significant. Overall fat content in the vertebral marrow was 48% $\pm$ 7.

Volunteer*	% Water	% Fat	Water T_2 ms	Fat T_2 ms
A (43)	54 ± 14	46 ± 14	78 ± 20	124 ± 12
B (31)	52 ± 11	48 ± 11	64 ± 15	95 ± 9
C (25)	57 ± 11	43 ± 11	85 ± 23	137 ± 16
D (27)	40 ± 9	60 ± 9	77 ± 14	121 ± 12
E (37)	59 ± 9	41 ± 9	50 ± 13	86 ± 14
Mean±SD**	52 ± 7	48 ± 7	71 ± 14	113 ± 21

Table 4.1: Calculated percentages of water and saturated fat proton peaks and their spectral T_2 values in vertebral bone marrow of five healthy adults. *: Age (years) in parentheses.
**: Inter individual mean value and standard deviation (SD).

Figure 4.5 is a plot of spectral T_2 values for water and saturated-fat protons as a function of position along the spine for one of the volunteers (37-year-old man). The intervertebral disk water T_2 values tend to be higher than the saturated-fat proton T_2 values. The water T_2 values in the vertebral marrow, however, are consistently shorter than the lipid T_2 values in this example as in all the other volunteers (Table 4.1).

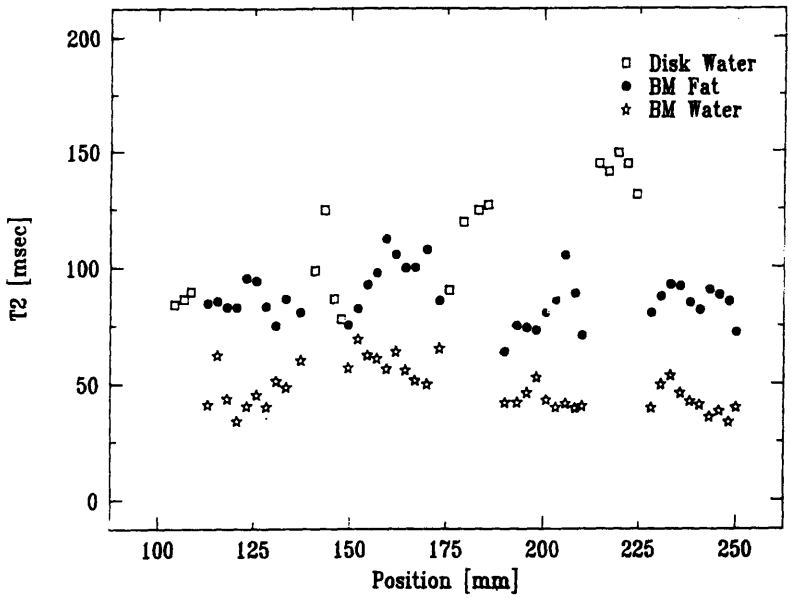

Figure 4.5: Plot of spectral T2 relaxation values versus position (superior to inferior) along the spinal column for a 37-year-old man. At intervertebral disk locations, only the water peak was analyzed and only water T2 values in these regions are shown. A total of 39 voxels within bone marrow contributed to this data set.

4.5 Bone Marrow Quantification in Knee

4.5.1 Introduction

Recall from Section 4.3 that the normal, progressive conversion of red to yellow marrow with aging follows a well-established pattern. Conversion from red (cellular) marrow to yellow (fatty) marrow results in intensity changes on T_1 weighted MR images [2-4, 6-13]. The increased fat content of yellow marrow yields higher signal intensity than red marrow on T_1 weighted image. Conventional MR images has been used to make qualitative assessments of water/fat content in marrow during growth and development [2-4, 6-13].

The purpose of this section is to demonstrate the line scan techniques as a quantitative tool to monitor bone marrow conversion and to study marrow disorders. The applications on bone marrow in knee that includes hematopieic and fatty marrow are presented. The line scan CPMG spectroscopic imaging techniques are applied to map major proton peaks through knees of healthy adults and a group of children. Their bone marrow are in various stages of red to yellow conversion. Information about the lipid spectrum, not only the water and saturted fat contents, are acquired and analyzed. The chemical composition of both red and yellow marrow in knees and spectral T_2 relaxation values are quantified and mapped [14-16].

4.5.2 Materials

The knee studies were performed with the 1.5 T GE Signa scanner using a linear RF transmit/receive extremity coil. At the beginning of the scan, a set of T_1 weighted sagittal scout image (TR/TE = 600 /20, FOV = 20 cm) were acquired. From this set of images, a sagittal section including the distal femoral metaphysis (DFM), distal femoral epiphysis

(DFE), proximal tibial epiphysis (PTE) and proximal tibial metaphysis (PTM) was selected. With in this section, a tissue column 20 cm long and 5×5 mm^2 in cross section was selected. Visulizations of the column were performed with a RARE type sequence [17] (TR/effective TE = 600 /75, 18 second scan time), as described in Chapter 3.

The line scan spectroscopic CPMG sequence was then applied to collect multiple echo spectra along the tissue column. 128 phase encode steps, a 2 sec TR and one signal average per excitation were used. The acquisition time was 4 minutes 18 seconds. The resulted voxel size is $5 \times 5 \times 1.6$ mm^3.

Eight healthy adults and eight children were recruited for the studies. The 8 adult volunteers are between ages of 27 and 44 years (mean $\pm$ SD = 34 $\pm$ 6). One of these volunteer had knee pain but showed no abnormal findings on the T_1-weighted localizers. One 27-year-old woman showed some residual hematopoietic marrow in the distal femoral metaphysis, as seen on the T_1-weighted localizers and confirmed by the spectroscopic scan. The 8 children studied ranged in age from 2 to 16 years (mean $\pm$ SD = 9 $\pm$ 5 years). The spectroscopic imaging examination was performed as an adjunct to clinically indicated examinations. Diagnoses were as follows: 3 meniscal tears, 1 Blount disease, 1 popliteal cyst, 1 patellar fracture, 1 Salter II fracture of the proximal tibia. One patient had a negative examination. In the case of the physeal fracture, bone bruises and marrow edema secondary to trauma were observed. For all the children, special care was taken to measure and analyze spectra from marrow regions which were deemed normal from the MR images.

4.5.3 Spectral Acquisition Results

Figure 4.6 (a) shows a sagittal scout image of the knee of a 57-year-old man. The selected tissue column appears as a dark band on the slice image. The arrow points a location within the proximal tibial metaphysis region where the spectra are extracted and fitted on the following. Figure 4.6 (b) is the first echo spectroscopic image with TE of 78

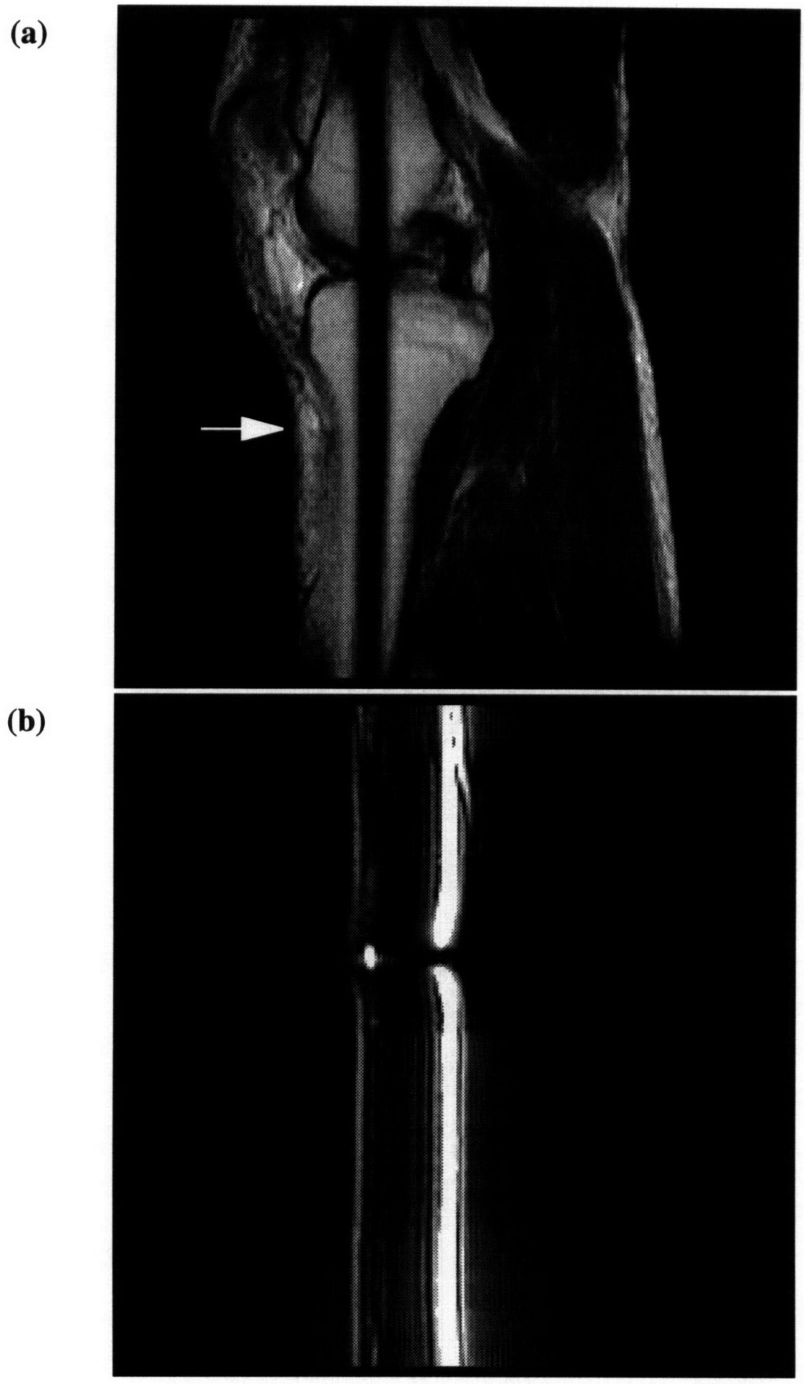

Figure 4.6 (a): T1-weighted sagittal scout image of a 57-year-old man. The dark band represents the selected tissue column. The arrow points at the proximal tibial metaphysis region where single voxel spectra are to be extracted. **(b):** Frist echo spectroscopic image with TE of 78 ms. The echo readout was 64 ms. The horizontal dimension is spectra and vertical dimension is spatial axis.

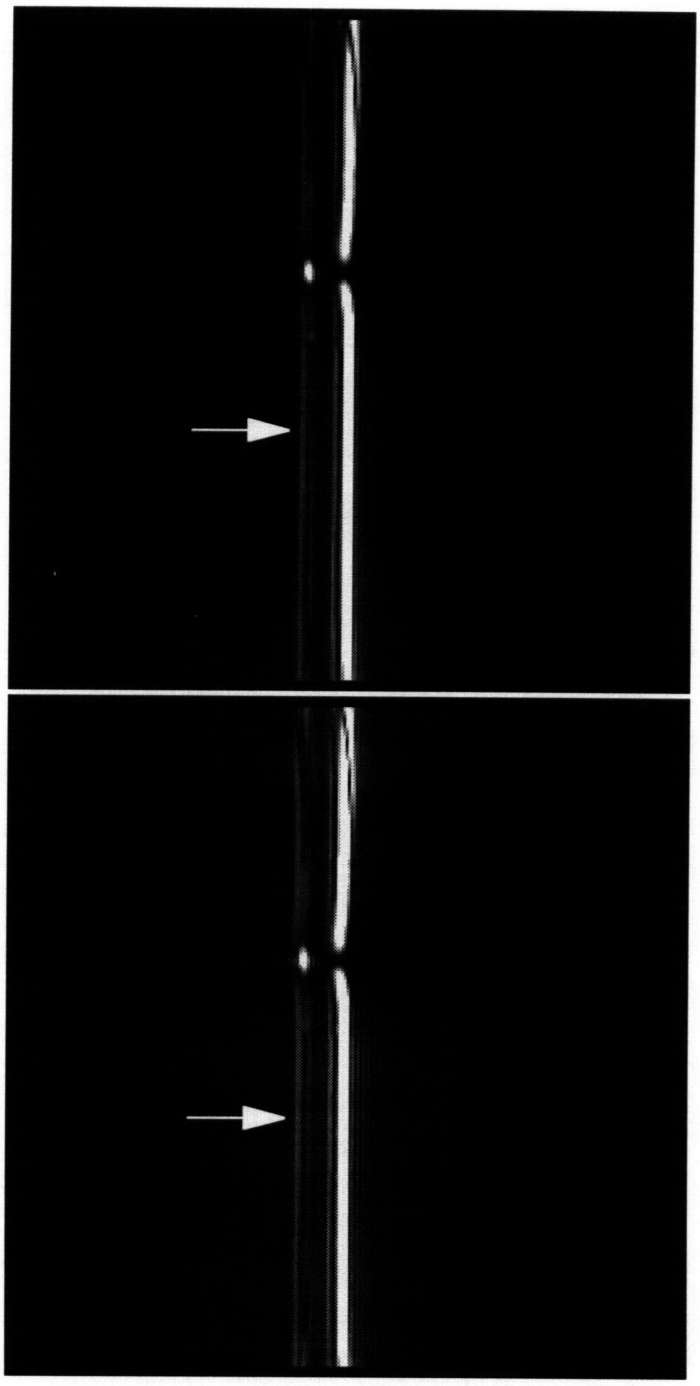

Figure 4.6 (c): First echo spectroscopic imag with TE of 48 msec. The echo readout was 32 ms. The arrow points to the location within the distal tibial metaphysis region where spectra are to be extracted. **(d):** Second echo image with TE of 96 ms.

(c)

(d)

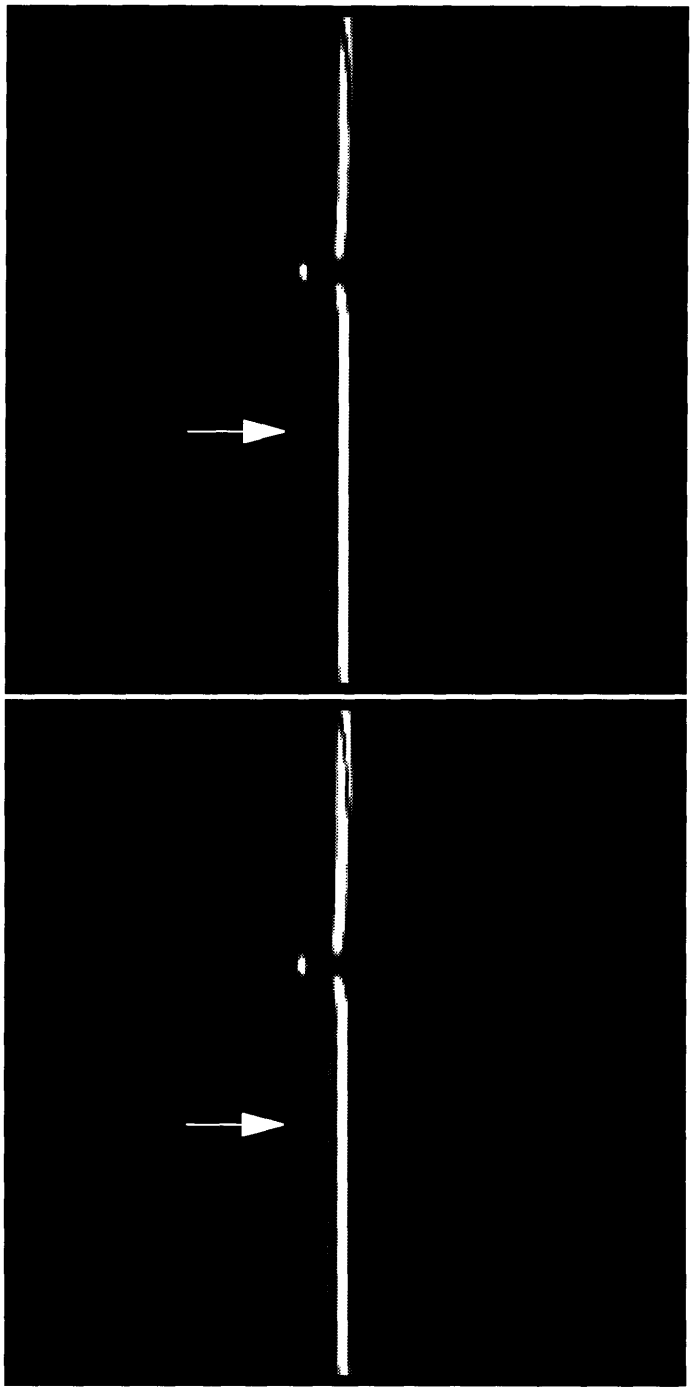

Figure 4.6 (c): First echo spectroscopic imag with TE of 48 msec. The echo readout was 32 ms. The arrow points to the location within the distal tibial metaphysis region where spectra are to be extracted. **(d):** Second echo image with TE of 96 ms.

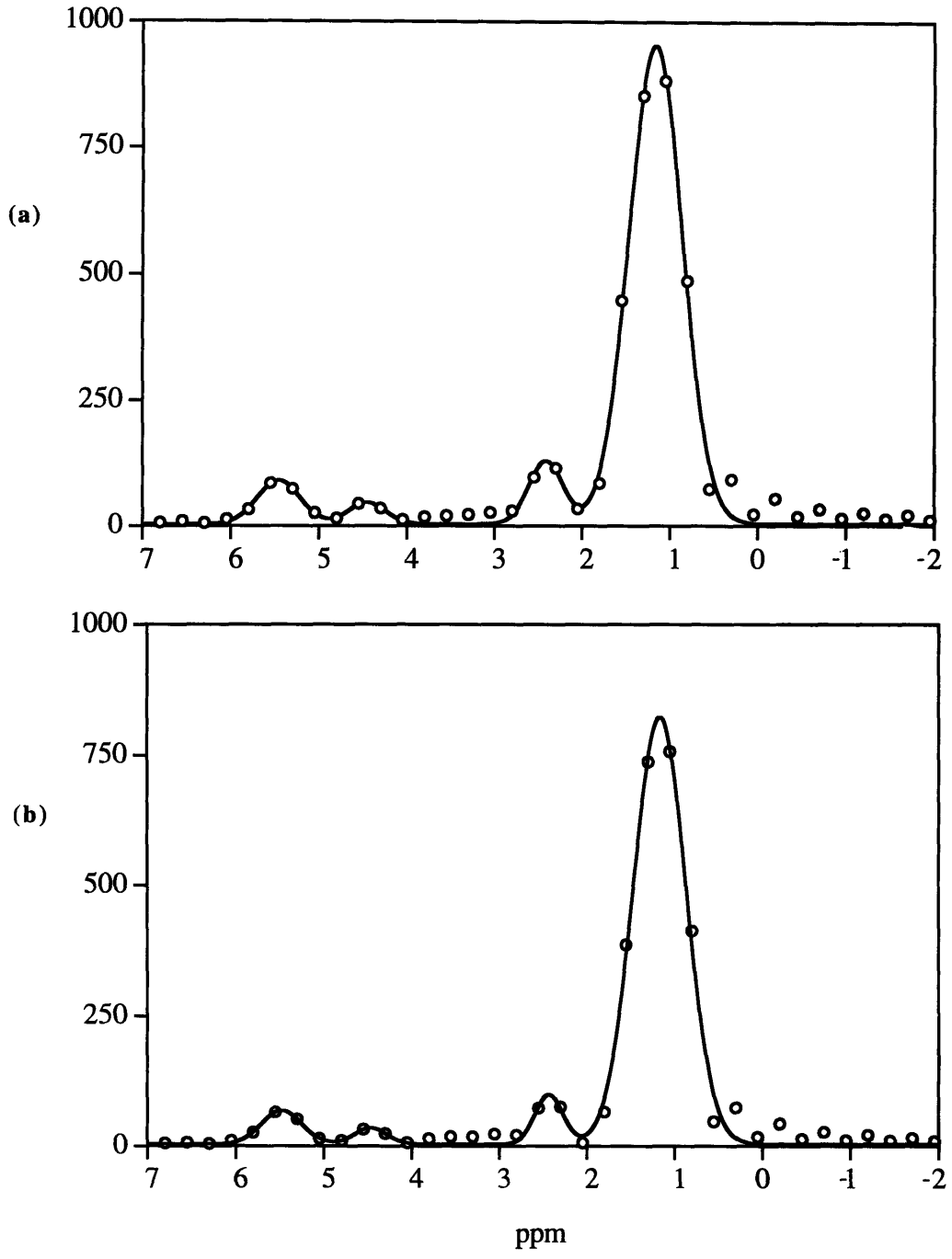

Figure 4.7: Spectra extracted from the arrow location within PTM in Figure 4.6. Horizontal axis is chemical shift and vertical axis is spectral intensity. The circles are MR experimental data and solid lines are expontential fits. **(a):** Spectra of first echo with TE of 48 ms. **(b):** Spectra of second echo with TE of 96ms.

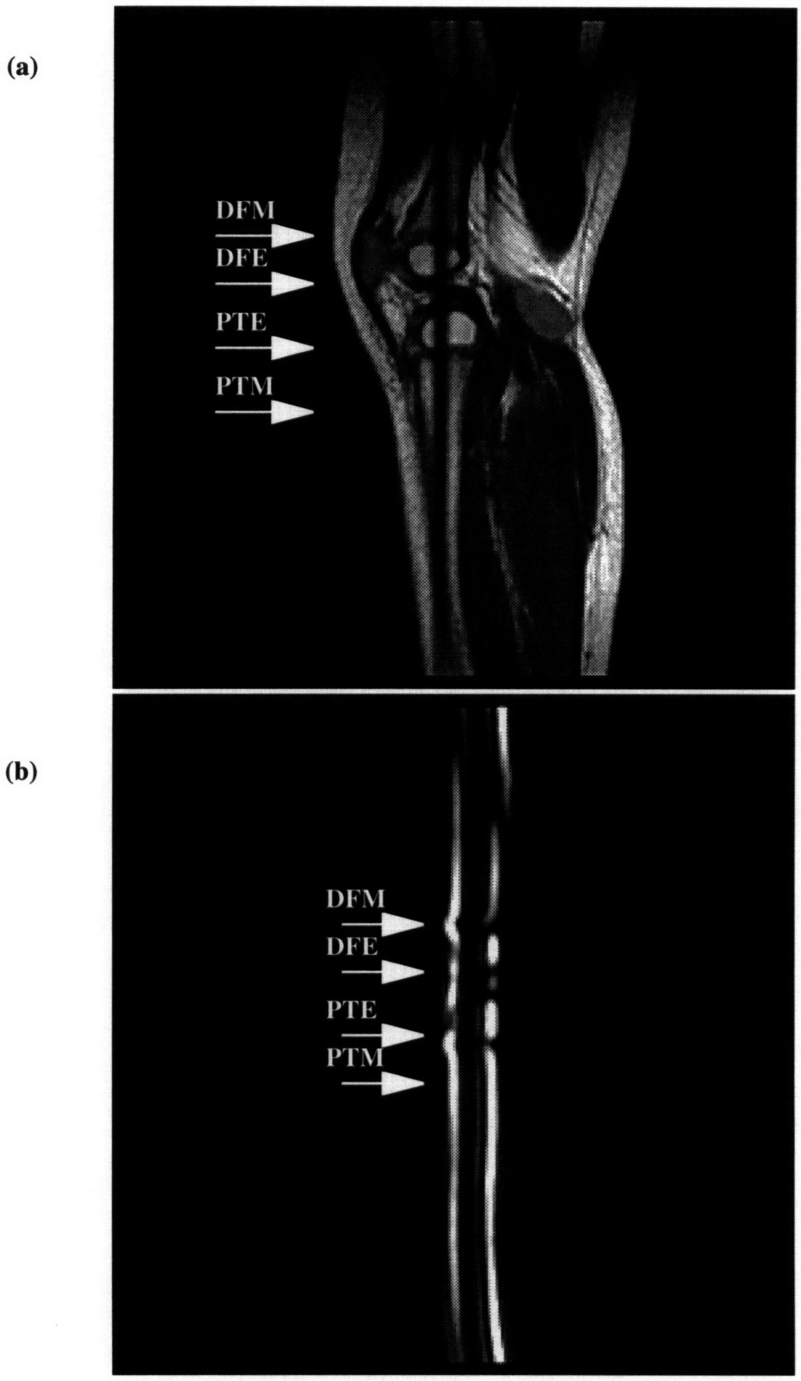

Figure 4.8. (a): Sagittal slice of the knee of a 2-year-old girl with column selection. The arrows point to regions that correspond to distal femoral metaphysis, distal femoral epiphysis, proximal tibial epiphysis, and proximal tibial metaphysis. **(b):** First echo spectroscoic image at TE of 48 ms. Note the water contents are less in two epiphysis than in two metaphysis.

(c)

(d)

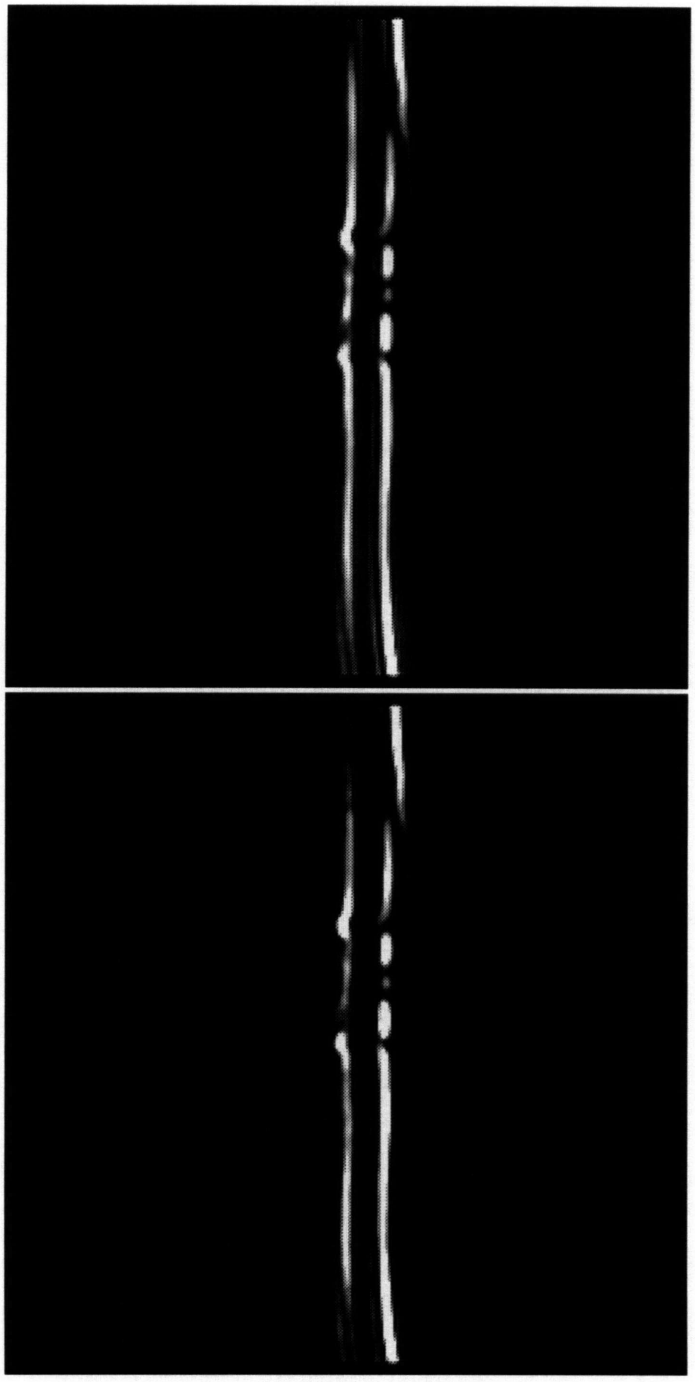

Figure 4.8. **(c):** Second echo spectrscopic image at TE of 96 ms.
(d): Fifth echo spectroscoic image at TE of 240 ms.

(c)

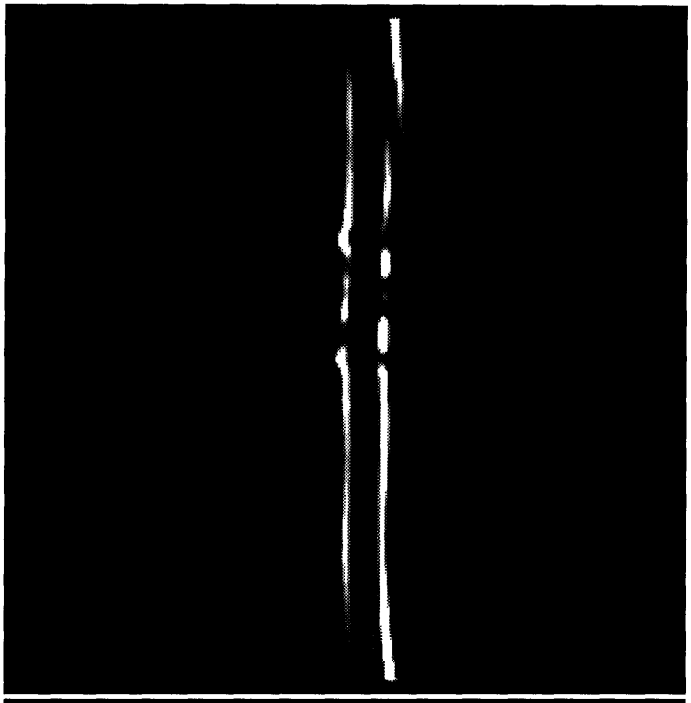

(d)

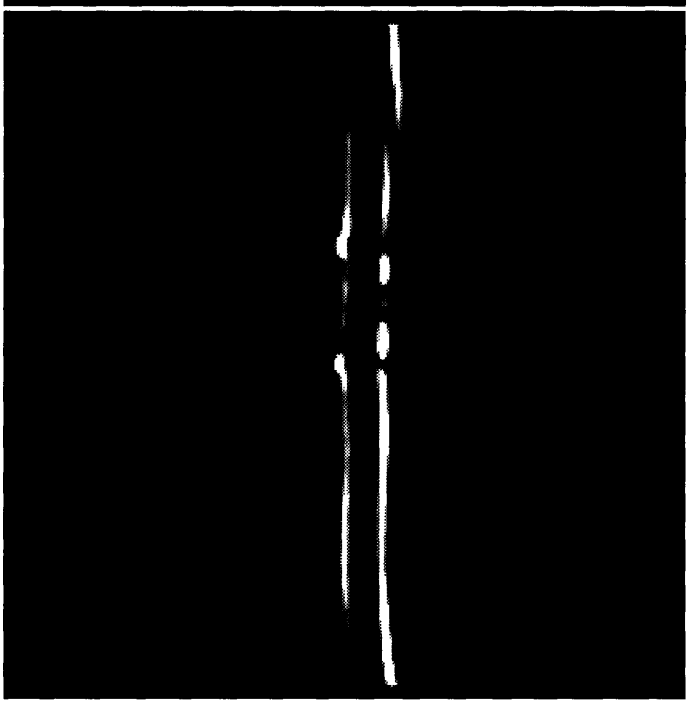

Figure 4.8. (c): Second echo spectrscopic image at TE of 96 ms.
(d): Fifth echo spectroscoic image at TE of 240 ms.

Figure 4.10 shows single voxel spectra extracted from a 32-year-old woman (top) and a 13-year-old boy (bottom) at locations within the DFM, DFE, PTE and PTM. The adult bone marrow spectra show little variation with location. The metaphyseal marrow spectra in the boy had large water peaks, making independent quantification of the neighboring olefinic peak impossible. The epiphyseal marrow spectra more closely resembled that of the adult spectra, with a reduced water allowing for spectra quantification of both olefinic proton and water peaks in 6 to 4 ppm range.

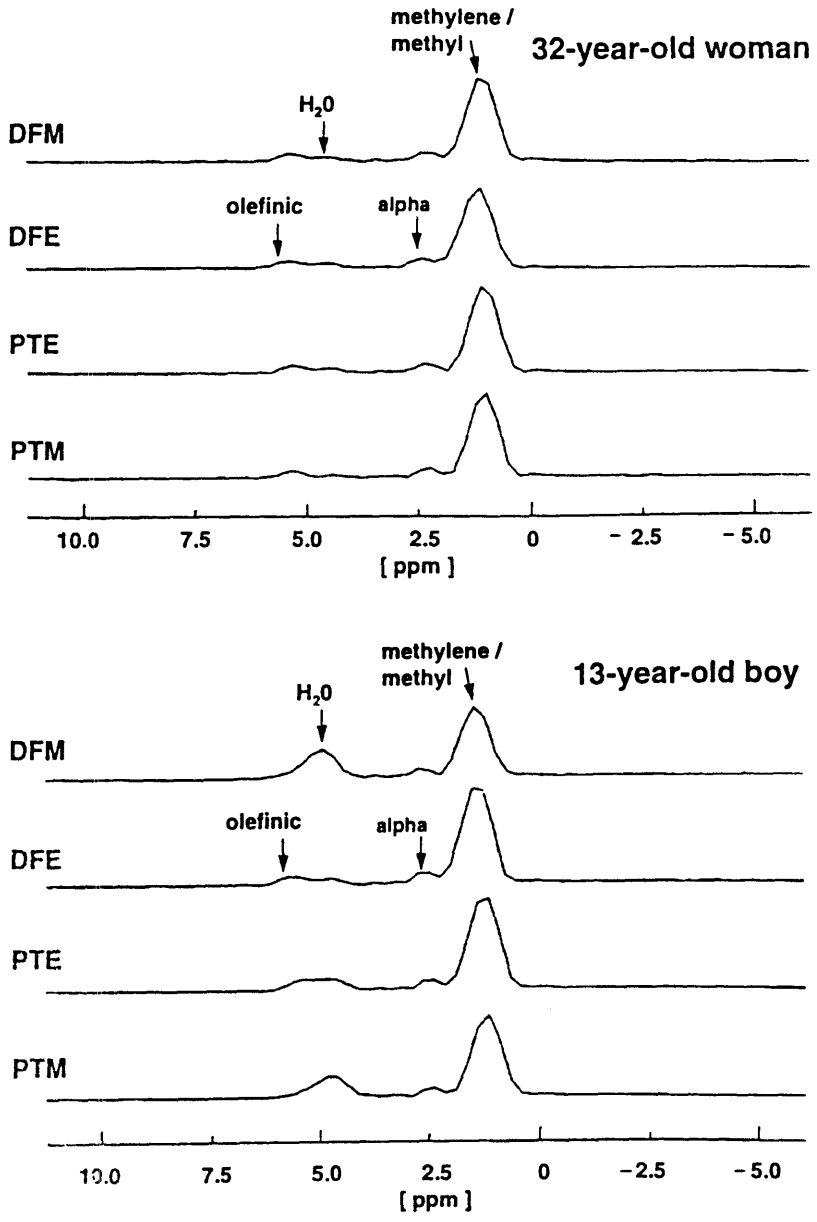

Figure 4.10: Spectra extracted from single voxels from a 32-year-old woman (**top**) and a 13-year-old boy (**bottom**). Single voxels are located at regions of DFM, DFE, PTE, PTM. Spectral peaks are identified with arrows.

4.5.4 Spectral Analyses Results

Figure 4.11 demonstrates double Gaussian lineshape fits (solid lines) of spectral data from a voxel in epiphyseal marrow (DFE) of the 32-year-old woman at the first three echoes. The olefinic and water proton spectral region and the alpha and methylene/methyl proton spectral regions are shown separately for clarity (bottom and top, respectively). In much of the metaphyseal marrow of the children, the water proton peak dominated the olefinic and water spectral region and prohibited separate Gaussian fitting of the olefinic proton peak (see Figure 4.9).

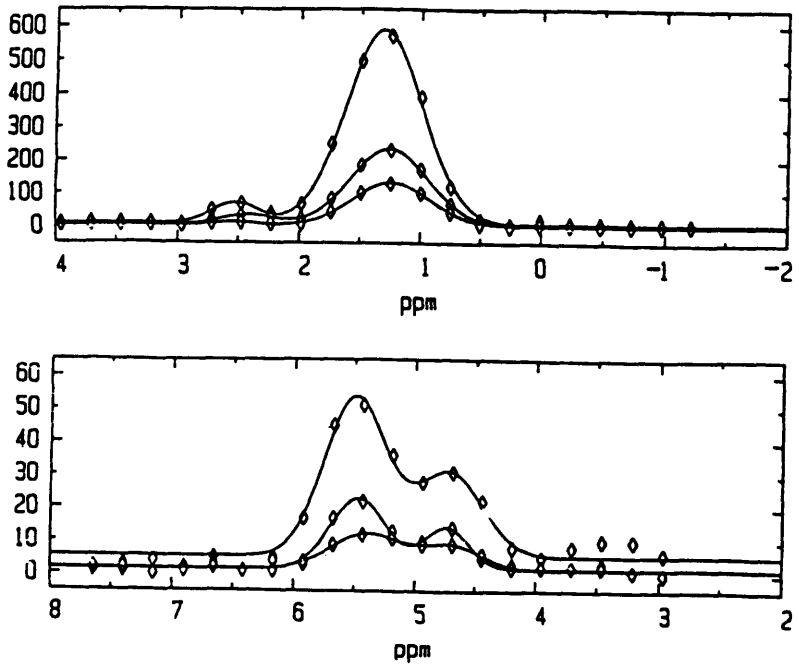

Figure 4.11: Gaussian fits to the alpha and methylene/methyl region **(top)** and olefinic/water region **(bottom)**. The spectra were extracted from adult metaphyseal marrow of a 32-year-old woman at the first three echoes (TE: 48, 96, 144 ms).

Typical spectral peak areas averaged over 10 to 20 voxels within metaphyseal marrow are plotted as functions of echo time in Figure 4.12 (a) and (b) along with best fits of the decay curves to Equation [2] (solid lines). In the adult yellow marrow, water peak areas were generally quantifiable for between two to four echoes (a). The alpha and olefinic proton peak areas were generally quantifiable for between 3 to 6 echoes (a). The methylene/methyl peak areas were quantifiable for all 8 echoes in both adults and children (b). In most of the metaphyseal marrow of the children, the olefinic peak was not quantifiable due to the dominance of the water peak. In these cases, the composite water/olefinic proton peak was quantifiable for between 5 and 8 echoes (b).

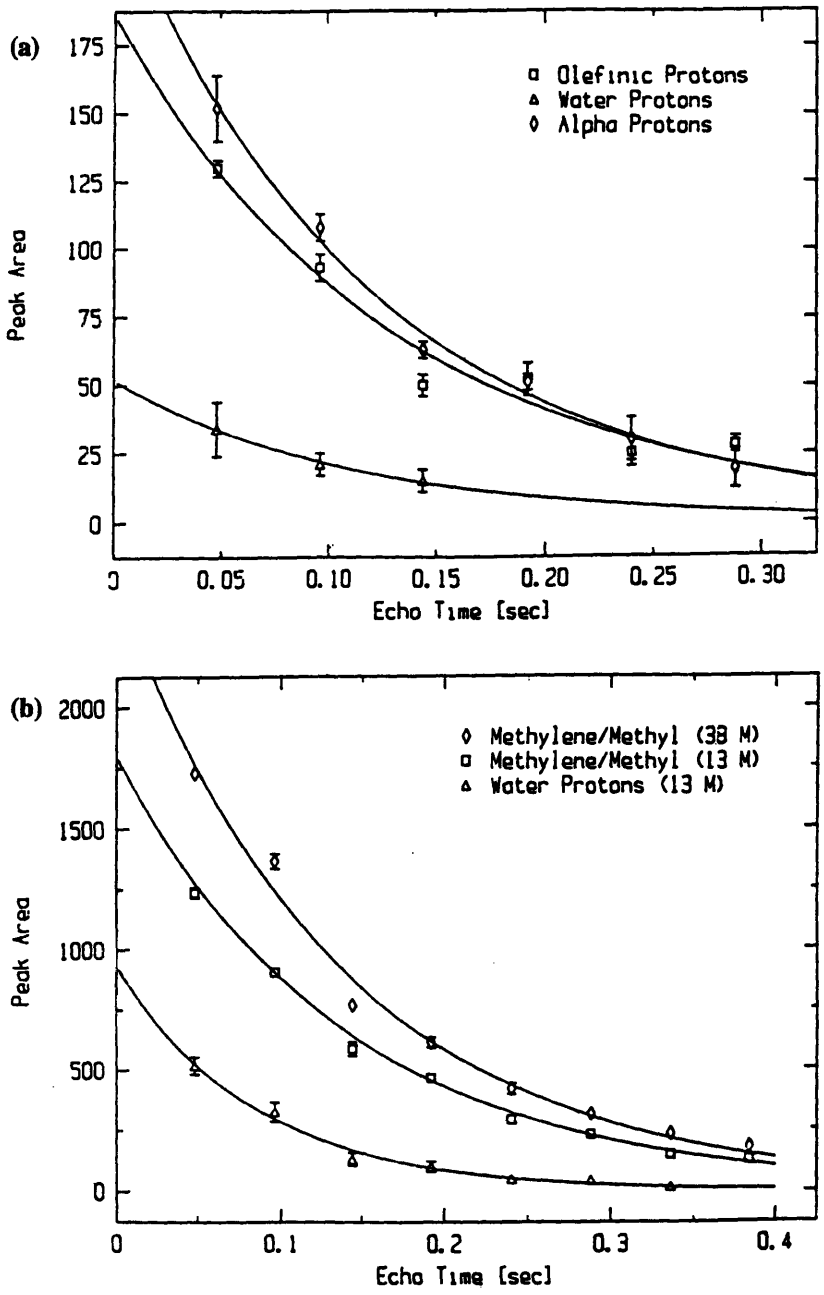

Figure 4.12. (a): Peak area decay with TE as averaged over 10 voxels in the metaphysis of a 38-year-old man for olefinic protons (squares), water protons (triangles), and alpha protons (diamonds). The solid line is the least squares fits of the data with a mono-exponential decay function. (b): Methylene/methyl peak area decay from metaphyseal marrow in the 38-year-old man (diamonds) and in a 13-year-old boy (squares). The water peak area decay from the boy is also plotted (triangles) and, unlike the adult yellow marrow water peak (triangle in (a)), is quantifiable for seven echoes and has a substantial amplitude when extrapolated to TE = 0.

Figure 4.13 maps concentrations at zero TE and T_2 values of water and methylene/methyl peaks of the 2-year-old girl in Figure 4. 8. (a) plots methylene/methyl and water extrapolated peak areas as a function of pixel position along the column. The pixel positions are 1.6 mm apart. The two strong lipid peaks positioning around pixel #90 and 122 correspond to the DFE and PTE. In DFM, at pixel location to the left of DFE, water concentration exceeds lipid concentration, a situation that is reversed in the PTM (pixel location 140-200). (b) is the T_2 map along the column for the methylene/methyl peak (solid line) and water peak (dashed line). In general, the water peak T_2 values are less than the methylene/methyl T_2 values, in agreement with the overall spectral T_2 values reported in Table 4.2 on the following.

Table 4.2 summarizes spectral transverse relaxation T_2 (mean ± standard deviation) found in the adults and children.

	Olefinic	Water	Alpha	Meth
Adults	97 ± 28	82 ± 25	78 ± 17	105 ± 26
Children	83 ± 26	73 ± 22	70 ± 20	95 ± 22

Table 4.2: Mean (± SD) transverse spectral relaxation times T_2 in ms for the four quantifiable peaks (Meth = methylene/methyl).

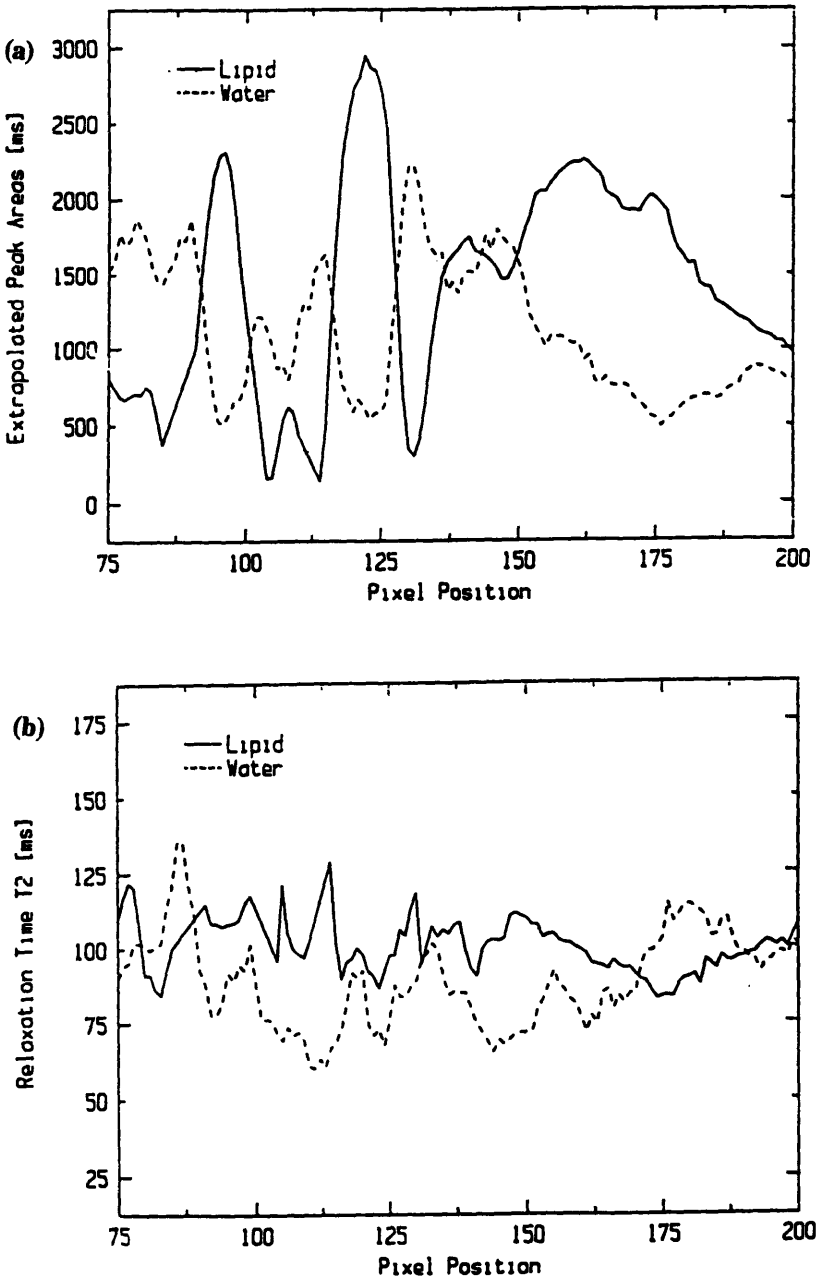

Figure 4.13: Quantitative analyses of water and methylene/methyl peaks of the 2-year-old girl in Figure 4.7. **(a):** Plot of methylene/methyl (solid line) and water (dashed line) extrapolated peak areas as a function of pixel position along the column. The pixels are 1.6 mm apart. **(b):** T2 map for methylene/methyl peak (solid line) and water peak (dashed line) along the column.

Figure 4.14 (a) and (b) present the extrapolated peak areas, expressed as percentages, for the regions sampled in the distal femoral metaphysis (top) and distal femoral epiphysis (bottom) for both the adults (a) and children (b). For each subject, olefinic proton (open bars), water proton (filled bars), alpha proton (left diagonal), and methylene/methyl proton (right diagonal) peak areas are plotted. The horizontal axis represents the subject number. Age/sex of these subjects in (a) are: 1: 38/M; 2: 32/F; 3: 38/F; 4: 44/M; 5: 39/F; 6: 35/M; 7: 35/F; 8: 27/F. In (b) age/sex are: 1: 2/F; 2: 8/M; 3: 9/F; 4: 11/M; 5: 12/M; 6: 13/M; 7: 14/M; 8: 16/F. Asterisks indicate that separate quantification of olefinic protons and water protons was not possible, and the percentage shown represents the combined water and olefinic contribution.

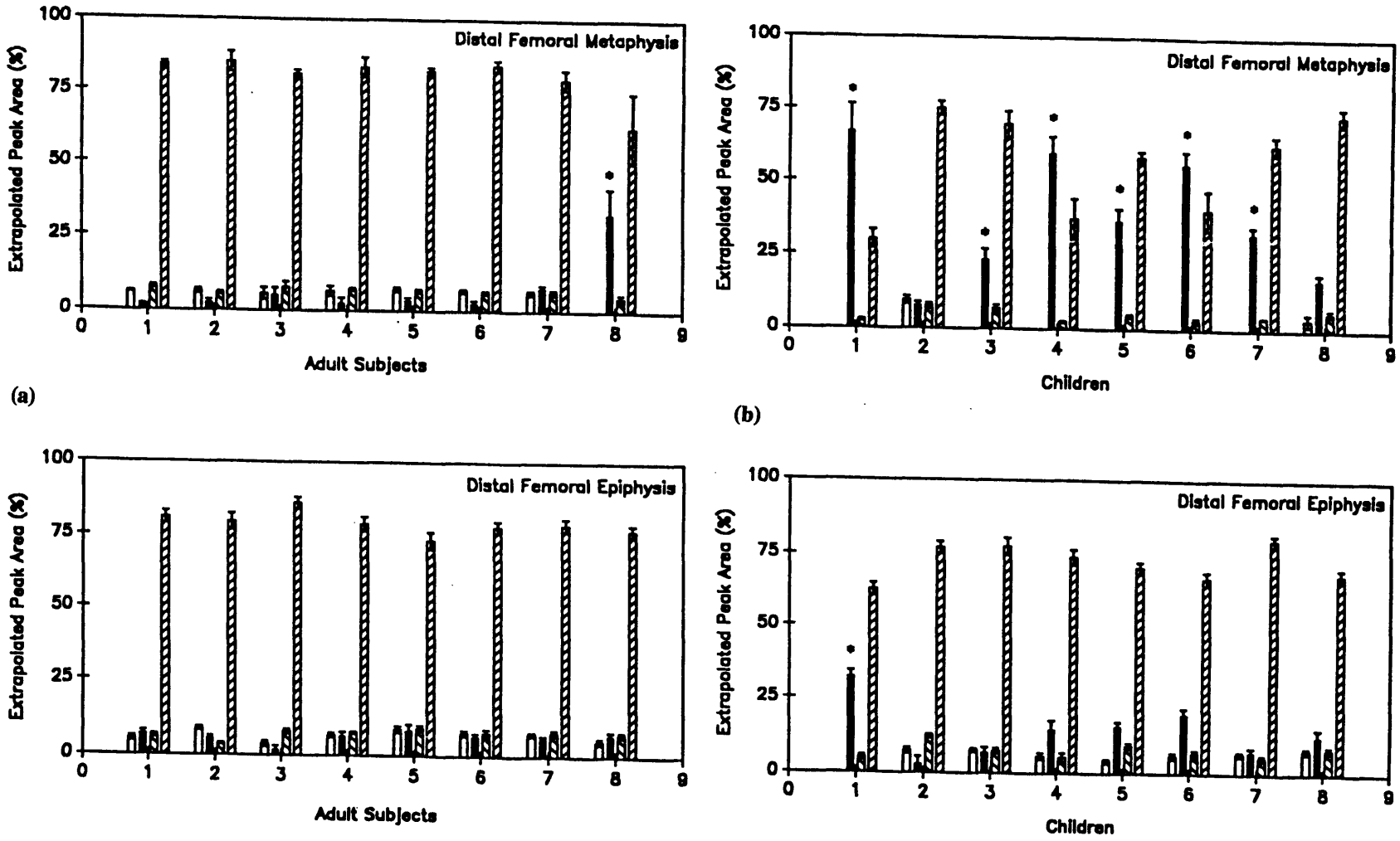

Figure 4.14. (a): Histograms of extrapolated peak areas in the adult population as found in the distal femoral metaphysis (top) and the distal femoral epiphysis (bottom). For each subject, olefinic proton (open bars), water proton (filled bars), alpha proton (left diagonal) and methylene/methyl proton (right diagonal) peak areas are plotted. (b): Histograms of extrapolated peak areas in the children from the same anatomic regions (DFM and DFE).

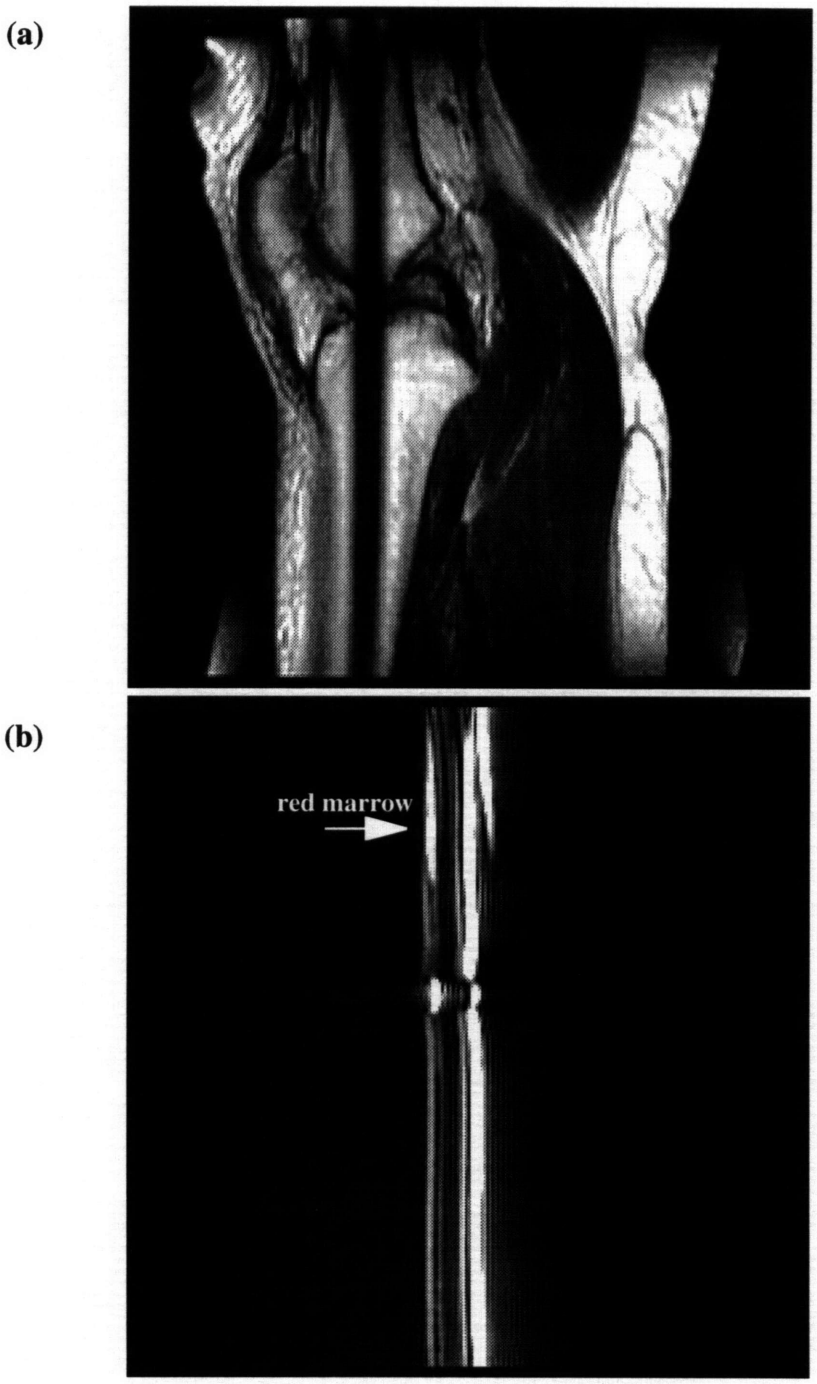

Figure 4.15. (a): Sagittal slice of the knee of a 27-year-old woman. The selected column, 5 by 5 mm squared, is a dark strip in the image. **(b):** First echo spectroscopic image with echo readout of 32 ms and echo spacing of 48 ms. The arrow points at distal femoral metaphysis where some residual red marrow is observed.

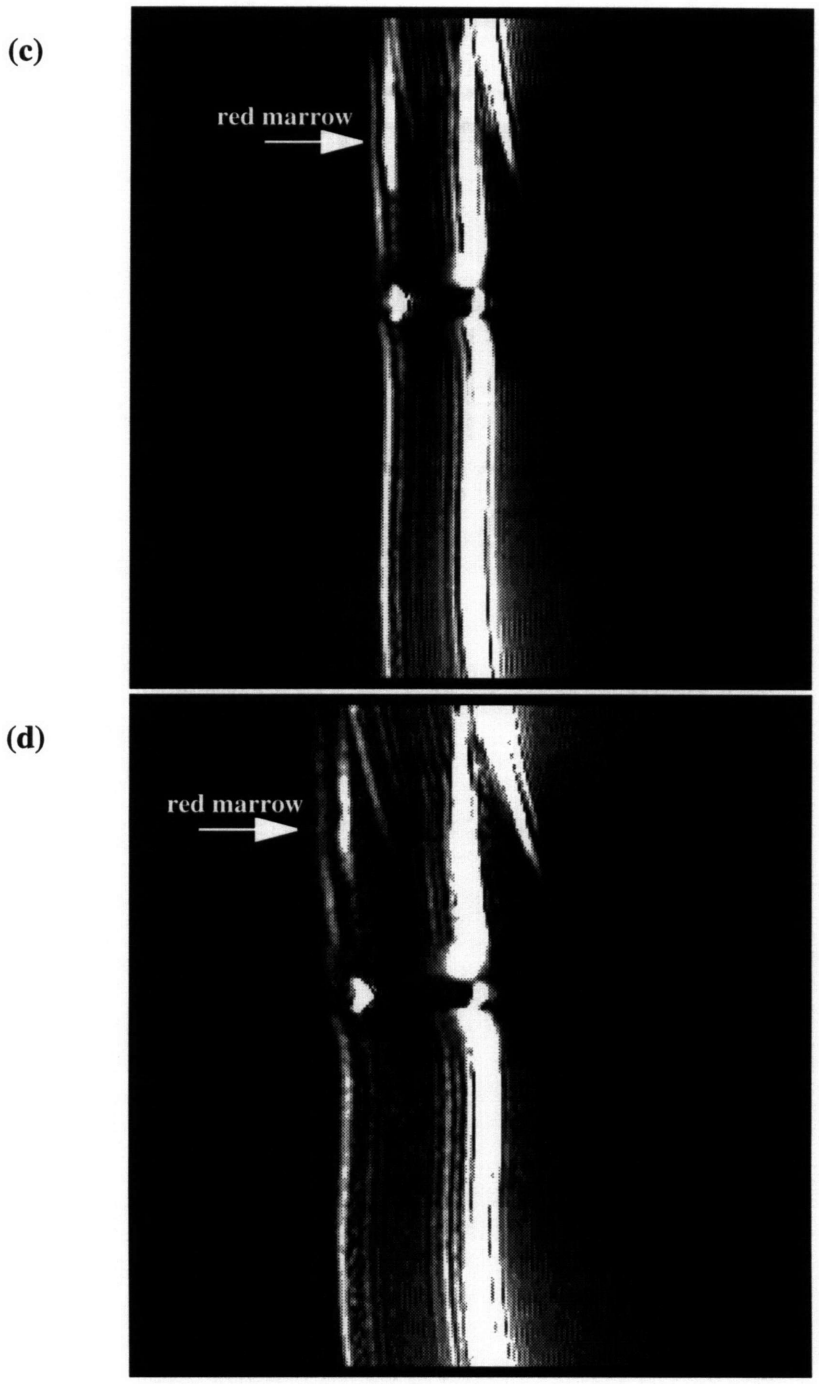

Figure 4.15 (c) (d): First echo spectroscopic image with echo readout of 64 ms **(c)** and 96 ms **(d)**. The echo spacings are 78 and 113 ms respectively. The arrow points at the residual red marrow at the distal femoral metaphysis region.

(c)

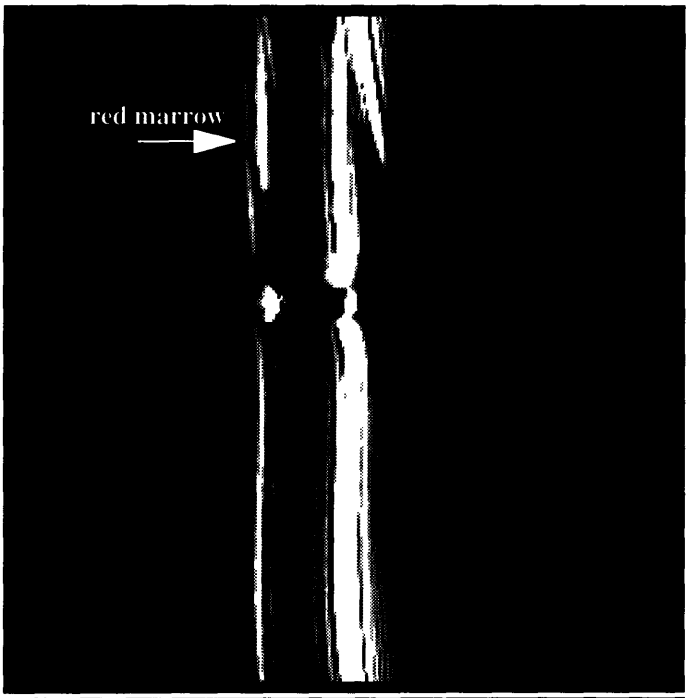

(d)

Figure 4.15 (c) (d): First echo spectroscopic image with echo readout of 64 ms **(c)** and 96 ms **(d)**. The echo spacings are 78 and 113 ms respectively. The arrow points at the residual red marrow at the distal femoral metaphysis region.

4.6 Discussion

4.6.1 Technical Aspects

This chapter has demonstrated the new *in vivo* proton MR spectroscopic imaging methodologies. The techniques provide measurements of intravoxel major proton content and spectral T_2 values throughout extensive regions of bone marrow. Since there are other MR techniques that have been used to obtain similar measurements, it is useful to compare the various methods from technical point of view.

Dixon/Sepponen techniques [20-22] have been used to estimate intravoxel fat/water content in lumbar spine [23-25]. A major advantage of these techniques is that data are collected in full image matrix formats with high spatial resolution and large volume coverage. A disadvantage is the low spectral resolution. Essentially, two-point spectra represented by "in-phase" and out-of-phase" images are added or subtracted to yield pure "fat" or pure "water" images. Additional images that are not in or out phase may be collected to correct for problems associated with the inherently limited sampling of the spectral dimension [22]. The cost is additional imaging time and more sophisticated post-processing. Corrections for different spectral relaxation times may be made by obtaining data sets at different TR and TE values [23-26]. However, to save time, the relaxation measurements are generally based on two-point analyses [23-25] and thus may lack accuracy [27, 28].

A technique at the opposite extreme from the Dixon/Sepponen approach is the single-voxel spectroscopic localization approach [29-31]. Here, a high resolution spectrum is acquired from a selected voxel in 3-5 minutes. Although the method is limited in the amount of tissue that can be studied in reasonable examination times, the spectral resolution is on the order of 1 Hz, making peak area quantification extremely accurate. Thus, spectral peaks other than the water and saturated fat protons can become available for analysis.

Sequence parameters can be adjusted so that corrections for differences in spectral relaxation times to the fat/water percentages are minimal [29].

The line scan methods introduced in this thesis represent a compromise between the high-spatial, low-spectral resolution of the Dixon/Sepponen technique and the high-spectral, low-spatial resolution of the single-voxel spectroscopic approach. The spectral resolution is not as good as it is in the latter method, although it is clearly sufficient to quantify 4 major proton peaks at 1.5 T (Figure 4.7). Many more voxels are sampled than with the single-voxel approach, although not nearly as many as are sampled with Dixon/Sepponen techniques. On the other hand, when addressing the issue of bone marrow cellularity, most of the voxels acquired with Dixon/Sepponen imaging methods are superfluous. In this context, proper placement of tissue columns with inner-volume techniques allows extensive coverage of voxels specifically within bone marrow while maintaining the essential features of the single-voxel spectroscopic examination. Also, eight TEs are sampled, allowing more accurate evaluation of spectral T_2 values than is possible with two-point methods [28]. Use of the relative of long TR of 2 seconds minimizes T_1 saturation of the spectral peaks [29].

The susceptibility induced frequency shift (shown as spectral curvature in Figure 4. 15 (d)) would cause dephasing and line broadening if a large voxel is localized as in single voxel spectroscopy. The column localization helps to minimize such dephasing by choosing a smaller voxel and more spatial sampling than volume localized spectroscopy since the inter voxel shift appears as curvature. However, the susceptibility shift slightly varies the voxel localization along the column. For a 0.5 ppm frequency shift, the spatial variation is about 0.08 mm or about 2% for 5 mm thick column and a gradient strength of 1 gauss/cm.

The line scan techniques have been designed to take advantage of scanner setup and bone marrow distributions in human. For applications not amicable for column localization, the line scan techniques can either be expanded to 2-D CSI with CPMG or RARE by adding another phase encoding along Gx direction (Figure 3.2) or provide a rapid and/or an initial spectroscopic assessments combining with other CSI techniques.

4.6.2 Studies on Vertebral Marrow

The vertebral bone marrow studies focus on quantification of the water and saturated fat protons. Since all three methods mentioned above have been used to study vertebral bone marrow in adult volunteers, it is of interest to compare respective results with regard to relative fat and water contents.

Rosen et al [23] used the Dixon/Sepponen method in lumbar spine studies of six healthy volunteers ranging in age from 21 to 47 years. They reported the fat content as 29% ± 6 in healthy vertebral bone marrow and have used this figure in later studies comparing healthy marrow with marrow from selected patient populations [24, 25]. In more recent studies using Dixon/Sepponen methods, a larger range of fat percentages have been reported, with a trend toward increased fat with age. For instance, Kauczor et al reported a fat content of 41% ± 13 in a healthy population with a mean age of 33 years [32].

Schick et al applied the single-voxel approach to study the spines of 15 healthy volunteers ranging in age from 20 to 68 years and reported fat/water ratios of 0.35 - 5.4 [33]. These ratios correspond to a range of 26% - 84% fat. We have now applied our techniques to the problem and have measured mean intravoxel percentages of fat ranging from 40% to 60% within the vertebral bone marrow of five healthy adult volunteers. The interindividual mean of 48% ± 7 is higher than that reported by Rosen et al [23] but is consistent with values reported by Kauczor et al and Schick et al [32, 33].

In addition to intravoxel estimates of relative fat and water contents, we have measured the spectral T_2 values of water and fat within vertebral marrow. The mean T_2 value for water in the marrow (71 ms ± 14) is longer than the 52-64 ms range reported by Rosen et al [23]. This may be the consequence of a reduced contribution to T_2 decay due to diffusion of water within local field inhomogeneities, stemming from the use of multiple 180° pulses [34]. The mean lipid T_2 value in vertebral marrow was 113 ms ± 21. Again, this is longer than the 56-98 ms range reported by Rosen et al [23] and may be due to the

use of multiple 180° pulses, which are known to effectively lengthen T_2 decay in J-coupled spin systems [34-36]. The statistically significant difference between the water T_2 and saturated fat proton T_2 indicates that extrapolation of peak areas to zero TE is necessary if meaningful fat/water percentages are to assessed.

4.6.3 Studies on Developing Knee Marrow

The line scan techniques are not limited to quantification of two primary peaks, water and saturated fat, as discussed in lumbar spine section. Other major lipid peaks can also be observed. As demonstrated in section 4.5, four peaks (water, methylene/methyl, olefinic, alpha) are quantified in yellow marrow spectra even with limited spectral resolution. Two of them are composite peaks [18, 19] in healthy adult yellow marrow. In developing knee marrow in children, insufficient conversion of red to yellow marrow in the metaphyses often made the olefinic peak unquantifiable due to the large overlapping water resonance. When the combined water/olefinic proton peak dropped to approximately 20 % of the spectrum, as in most epiphyseal marrow of the children studied, the two contributions were separately resolvable. Our spectral finding are qualitatively consistent with the known pattern of red to yellow marrow conversion. In each bone, the conversion begins in the epiphysis, followed by diaphysis and lastly the metaphysis. In each extremity, the conversion occurs from the periphery (fingers and toes) to the center. Thus, in the knee the expected conversion sequence is proximal tibial epiphysis $\rightarrow$ distal femoral ephiphysis $\rightarrow$ proximal tibial metaphysis $\rightarrow$ distal femoral metaphysis. The finding of less water in epiphseal marrow than metaphyseal marrow in the children 8 to 16 year old is consistent with this pattern. The extrapolated peak areas mapping for mthylene/methyl protons and water for 2-year-old girl (Figure 4. 13) are also in accord with the accepted pattern of conversion from periphery to center [3, 4].

It is possible that longer echo readouts within the CPMG trains will help resolve olefinic and water peaks in red marrow, help differentiate peaks currently unresolved within the alpha peak, and help resolve methylene from methyl protons. However, longer echo readouts entail longer echo spacing in the CPMG trains which will, at the very least, increase signal loss from T_2 decay process. It is equally important to note that there are several physical mechanisms in bone marrow which make the spectral T_2 relaxation behavior depend upon the echo spacing chosen. The T_2 decay of water is influenced by diffusion within magnetic field inhomogeneities generated by susceptibility differences between trabecular bone and bone marrow [35, 37]. This can shorten effective water T_2 values at longer echo spacing, potentially limiting water detectability and quantification. For the lipid components, multiexponential relaxation [38] from composite peaks and amplitude modulations due to J-coupling interactions [36, 39-41] influence the observed T_2 behavior in an echo spacing dependent manner. In this work for instance, we consistently found that olefinic proton peak area estimated from the fourth echo was consistently as large or even larger than that calculated from the third echo (Figure 4. 12), a feature we attribute to J-coupling.

Consideration of these complexities underscores an important feature of the CPMG spectroscopic imaging technique. Namely, though the method yields both spectroscopic and T_2 relaxation information, there exists a fundamental tradeoff between these two types of information. Further studies will be useful for evaluating the advantages and limitations associated with different CPMG spectroscopic imaging parameters for studying the complex spectroscopic and relaxation characteristics of protons in both red and yellow marrow.

References

1. Mulkern RV, Meng J. Jaramillo D, Oshio K. Fat and water quantification in spine and knee with inner volume CPMG sequences and automated post-processing", Book of Abstracts, Annual Meeting of SMRI, JMRI 3 (p), 1993.

2. Vogler JB III, Murphy WA. Bone marrow imaging. Radiology 1988; 168: 679-693.

3. Moore SG, Dawson KL. Red ad yellow marrow in the femur: age-related changes in appearence at MR imaging. Radiology 1990; 175: 219-223.

4. Ricci C, Cova M, Kang YS, Yang A, Rahmouni A, Scott WW, Zehouni EA. Norma age-related patterns of cellular and fatty bone marrow distribution in the axial skeleton: MR imaging study. Radiology 1990; 177: 83-88.

5. Mulkern RV, Meng J, Oshio K, Guttmann CRG, Jaramillo D. Bone marrow characterization in the lumbar spine with inner volume spectroscopic CPMG imaging studies. JMRI 1994; 4: 585-589.

6. Dooms GC, Fisher MR, Hricak H, Richardson M, Crooks LE, Genant HK. Bone marrow imaging: Magnetic resonance studies related to age and sex. Radiology 1985; 155: 429-432.

7. Kangarloo H, Dietrich RB, Taira RT, GOld RH, Lenarsky C, Boechat MI, Feig SA, Salusky I. MR imaging of bone marrow in children. J. Comput Assist Tomogr 1986; 10: 205-209.

8. Jaramillo D, Laor T, Hoffer FA. Epiphyseal marrow in infancy: MR imaging. Radiology 1991; 181: 809-812.

9. Shellock FG, Morris E, Deutsch AL, Mink JH, Kerr R, Boden SD. Hematopietic bone marrow hyperplasis: High prevalence on MR images of the knee in asymptomatic marathon runners. AJR 1992; 158: 335-338.

10. Mirowitz SA. Hematopoietic bone marrow within the proximal humeral epiphyses in normal adults: Investigation with MR imaging. Radiology 1993; 188:689-693.

11. Lang PH, Fritz R Majumdar S, Vahlensieck M, Peterfy C, Genant HK. Hematopietic bone marrow in the adult knee: Spin-echo and opposed-phase gradient-echo MR imaging. Skeletal Radiology 1993; 22: 95-103.

12. Kricun ME. Red-yellow marrow conversion: Its effect on the location of some solitar bone lesions. Skeletal Radiology 1985; 14: 10-19.

13. Deutsch AL, Mink JH, Rosenfelt FP, Waxman AD. Incidental detection of hematopoietic hyperplasia on routine knee MR imaging. AJR 1989; 152: 333-336.

14. Mulkern RV, Meng J, Oshio K, Williamoson DS, Lilly HS, Guttmann CRG, Jaramillo D. MRS imaging of the knee with line scan CPMG sequences. J. Computer Assisted Tomography, 1995; 19(2): 247-255.

15. Mulkern RV, Meng J, Guttmann CRG, Oshio K, Jaramillo D. Spectral characterization of marrow conversion using inner volume spectroscopic CPMG sequences. Book of Abstracts, First Meeting of SMR, 1994.

16. Jaramillo D, Meng J, Oshio K, Guttmann CRG, Mulkern RV. Evaluation of red and yellow marrow in children and young adults using spectroscopic CPMG imaging. Book of abstracts, Annual Meeting of RSNA, 1993.

17. Oshio K, Mulkern RV. Rapid fat/water assessment in knee cavity bone marrow by inner volume spectroscopic imaging with RARE. JMRI 1992; 2: 601-604.

18. Gussoni M, Greco F, Pegna M, Bianchi G, Zetta L. Solid state and microscopy NMR study of the chemical constituents of Afzelia cuanzensis seeds. Magn. Reson. Imag. 1994; 12: 477-486.

19. Brix G, Heiland S, Bellemann ME, Koch T, Lorenz WJ. MR imaging of fat-containing tissues: valuation of two quantitative imaging techniques in comparison with localization proton spectroscopy. Magn. Reson. Imaging. 1993; 11: 977-991.

20. Dixon WT. Simple proton spectroscopic imaging. Radiology 1984 153: 189-194.

21. Sepponen RE, Sipponen JT, Tanttu JI. A method for chemical shift imaging: demonstration of bone marrow involvement with proton chemical shift imaging. J. Comput Assist Tomogr 1984; 8: 585-587.

22. Glover GH. Multipoint Dixon technique for water and fat proton and susceptibility imaging. Magn Reson Med 1990; 16: 67-79.

23. Rosen BR, Fleming DM, Kushner WP, Wismer GL, Brady TJ. Hematologic bone marrow disorders: quantitative chemical shfit MR imaging. Radiology 1988; 169:799-804.

24. Gerard EL, Ferry JA, Amrern PC, Harmon DC, McKinstry RC, Hoppel BE, Rosen BR. Compositinal changes in vertebral bone marrow during treatment for acute leukemia: assessment with quantitative chemical shift imaging. Radiology 1992; 183:39-46.

25. Johnson LA, Hoppel BE, Gerard EL, Miller SP, Doppelt SH, Zirzow GC, Rosenthal DI, Dambrosia JM, Hill SC, Brady RO, Rosen BR, Barton NW. Quantitative chemical shift imaging of vertebral bone marrow in patients with gaucher disease. Radiology 1992; 182:451-455.

26. Buxton RB, Wismer GL, Brady TJ, Rosen BR. Quantitative proton chemical shift imaging. Magn. Reson Med 1986; 3: 881-900.

27. Mulkern RV, Wong STS, Jakab P, Bleier AR, Sandor T, Jolesz FA. CPMG imaging sequences for high field in vivo transverse relaxation studies. Magn Reson Med 1990; 16: 67-79.

28. Wong STS, Roos MS. Effects of slice selection and diffusion on T_2 measurement. Magn Reson Med 1987; 5: 358-365.

29. Ballon D, Jakubowski A, Gabrilove J, Graham MC, Zakowski M, Sheridan C, Koutcher JA. In vivo measurements of bone marrow celularity using volume-localized proton NMR spectroscopy. Magn Reson. Med. 1991; 19:85-95.

30. Schick F, Bongers H, Jung W, Skalej M, Lutz O, Claussen CD. Volume-selective proton MRS in vertebral vodies. Magn. Reson Med 1992; 26:207-217.

31. Jensen KE, Jensen M, Grundtvig P, Thomsen C, Karle H, Henriksen O. Localized in vivo proton spectroscopy of the bone marrow in patients with leukemia. Magn Reson Imaging 1990; 8:779-789.

32. Kauczor HU, Brix G, Dietl B, Jarosch K, Knopp MV, Kaick G. Bone marrow after autologous blood stem cell transplantation and total body irradiation: magnetic resonance and chemical shift imaging. Magn Reson Imaging 1993; 11: 965-975.

33. Schick F, Bongers H, Jung W, Skalej M, Lutz O, Claussen CD. Volume-selective proton MRS in vertebral vodies. Magn. Reson Med 1992; 26:207-217.

34. Listerud J, Einstern S, Outwater E, Kressel HY. First principles of fast spin echo. Magn Reson Q 1992; 8: 199-244.

35. Henkelman RM, Hardy PA, Bishop JE, Poon CS Plewers DB. Why fat is bright in RARE and fast spin-echo imaging. JMRI 1992; 2:533-540.

36. Allerhand A. Analysis of Carr-Purcell spin-echo NMR experiments on multiple pulse systems. I. The effect of homonuclear ccoupling. J. Chem Phys 1966; 44: 2-9.

37. Schick F, Einsele H, Kost R, Duda SH, Horny H-P, Lutz O, Claussen CD. Localized MR ^{1}H spectrocopy reveals alterations in bone marrow with hemosiderosis. Magn Reson Med 1994; 32: 470-475.

38. Whittall KP, Bronskill MJ, Henkelman RM. Investigation of analysis techniques for complicated NMR relaxation data. J. Magn Reson 1991; 95: 221-234.

39. Hinks RS, Henkelman RM. Problems with organic materials for magnetic resonance imaing phantoms. Med Phys 1988; 15: 61-63.

40. Melki PS, Jolesz FA, Mulkern RV. Partial RF echo planar imaging with the FAISE method: II. Contrast equivalence with spin echo sequences. Magn Reson Med 1992; 26: 342-354.

41. Mulkern RV, Bowers JL. Density matrix calculations of AB spectral modulations: Quantum mechanics meets in vivo spectroscopy. Concepts in Magnetic Resonance 1994; 6: 1-23.

Chapter 5

Applications: Lipid Chemical Composition

5.1 Introduction

Recall in Chapter 4 the spectroscopic studies on the developing knee marrow concentrated on water and major lipid protons while the studies on vertebral marrow focused on quantification of water and saturated-fat protons. High resolution MR spectroscopy shows that the lipid protons have at least eight resonance peaks [1, 2] with different T_1 and T_2 relaxation. Conventional MR images represent only "bulk" signal intensities, which reflect the sum of signals from all the mobile protons within a given volume element. Since a voxel in the fat-containing tissue such as bone marrow contains the lipid and water protons, the changes of the chemical composition in the voxel can not readily be distinguished from changes in the "bulk" relaxation time measurements [3].

The line scan spectroscopic imaging techniques provide the possibility to estimate T_1 and T_2 relaxation times of some resolved lipid resonances in the ^1H spectrum. The aim of this chapter is to demonstrate the feasibility of quantifying lipid chemical composition. Specifically, the spectroscopic imaging techniques are performed on bone marrow *in vivo* and on various oil samples. Quantification of the small lipid resonance peaks includes estimation of spectral T_1 relaxation values, detection of terminal methyl protons, mapping of fat unsaturation, and study of the levels of mono-unsaturated versus poly-unsaturated triglycerides.

The organization of the chapter is as follows. Section 5.2 provides a background about lipid proton resonances in ^1H spectra expected *in vivo*. Section 5.3 presents the

application of the line scan spectroscopic imaging techniques on an array of oil phantoms , and illustrates the oil spectra. Then the measurement of lipid spectral T_1 relaxation times in knee marrow with inversion recovery RARE spectroscopic imaging are presented (Section 5.4). Section 5.5 demonstrates the studies on monitoring the degree of unsaturation in triglycerides. The chapter concludes with a discussion (Section 5.6).

5.2 Lipid Proton Resonances

The purpose of this section is to introduce some background about lipid proton resonances in ^1H spectra and their chemical shift values [1, 2, 4, 5].

Lipid protons consist mainly of triacylglycerols (TAG), that is esters of the alcohol glycerol with three fatty acids. TAGs fill almost the entire fat cell volume. In human organism TAGs are found under the skin, in the abdominal cavity, in the mammary glands, and in the bone marrow. In contrast to water protons, lipid protons within TAG molecules are chemically distinct and give rise to at least eight resonance peaks with different T_1 and T_2 relaxation times in the ^1H MR spectrum. Figure 5.1 shows the main structural feature of a TAG molecule.

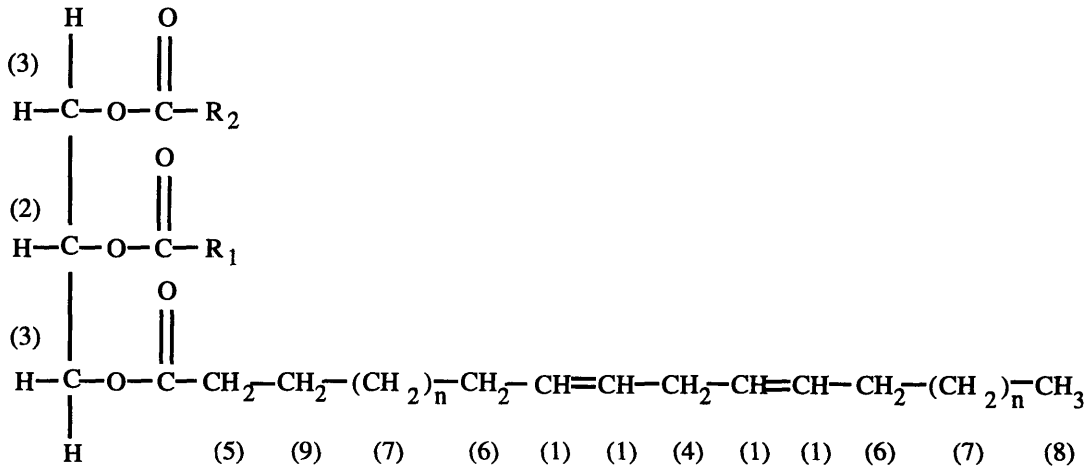

Figure 5.1: Chemically distinct lipid protons of triacylglycerols.

The assignments and the chemical shifts of the resonances are summarized in Table 5.1.

Resonance Number *	Assignment	δ (ppm) **
1	olefinic protons	5.4 - 5.6
2	CH of glycerol backbone	5.1
3	CH_2 of glycerol backbone	4.2
4	diallylic CH_2	2.8 - 3.0
5	CH_2, α to carboxyl	2.3 - 2.5
6	CH_2, α to double bond	2.0
7	CH_2 of aliphatic chain	1.3
8	terminal CH_3	0.9
9	CH_2, 2nd next to carboxyl	1.5
	H_2O	4.7

Table 5.1: Assignments and chemical shifts of proton resonances in lipids.
*: Resonances are numbered as in Figure 5.1. **: Chemical shift are relative to TMS.

5.3 Lipid Spectrum *in vitro*

To demonstrate the techniques with regard to quantification of lipid spectra, a phantom of 5 vials with various mixtures of fish oil and mineral oil was made. The line scan CPMG spectroscopic imaging techniques were applied on this array of oil with the 1.5 T GE clinical scanner. The spectroscopic images were acquired and the lipid resonance peaks stated in the previous section were identified. The scan parameters used were: TR of 2 s, 64 ms spectral read out, 20 cm FOV, 128 phase encoding steps, 1 signal average. The resulted voxel size is $5 \times 5 \times 1.6$ mm^3. The scan time was 4 minutes and 18 second for the 8-echo CPMG sequence, and 1 minute and 26 second for the 3-echo RARE sequence.

(a).

(b).

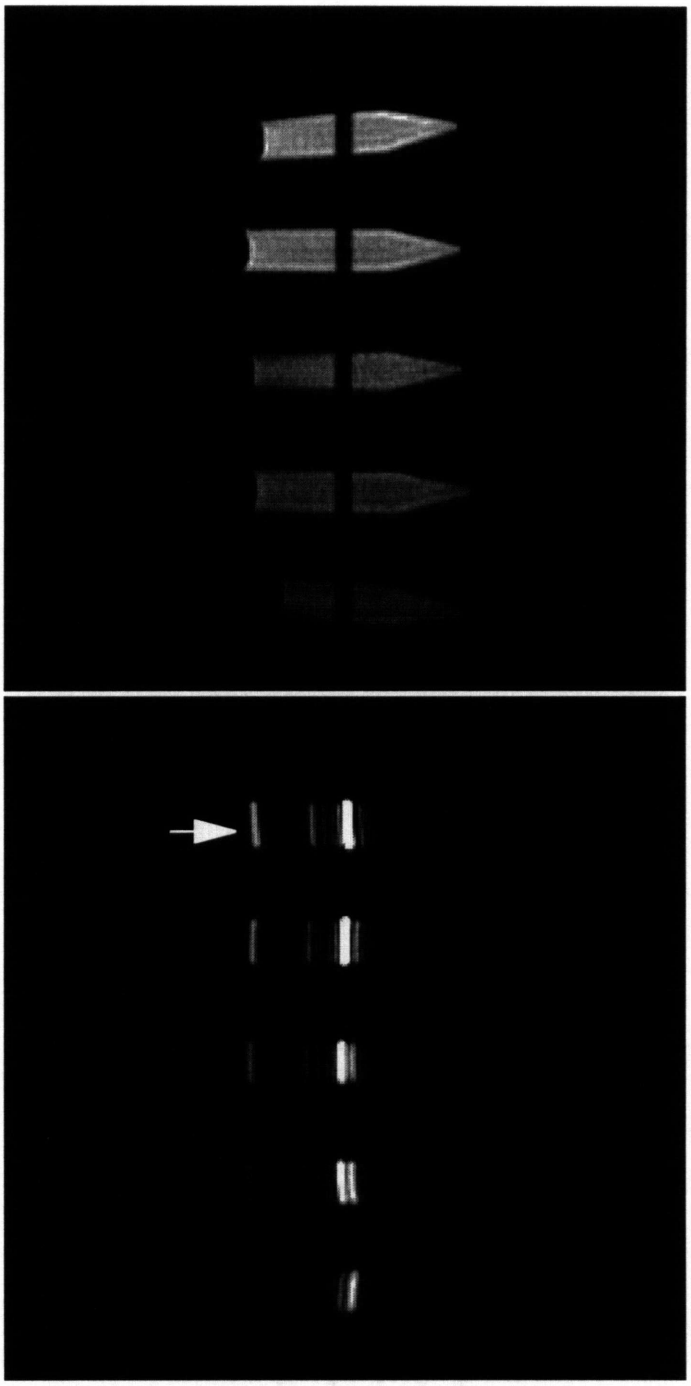

Figure 5.2. (a): An array of phantoms that are mixtures of fish oil and mineral oil. The weighted percentages for each phantom are (from top to bottom): 100% fish oil, 75% fish and 25% mineral oil, 50% fish and 50% mineral oil, 25% fish and 75% mineral oil, 100% mineral oil. **(b):** First echo CPMG spectroscopic image with TE of 78 ms. The echo readout is 64 ms. The arrow points where spectra are extracted from pure fishoil.

(c).

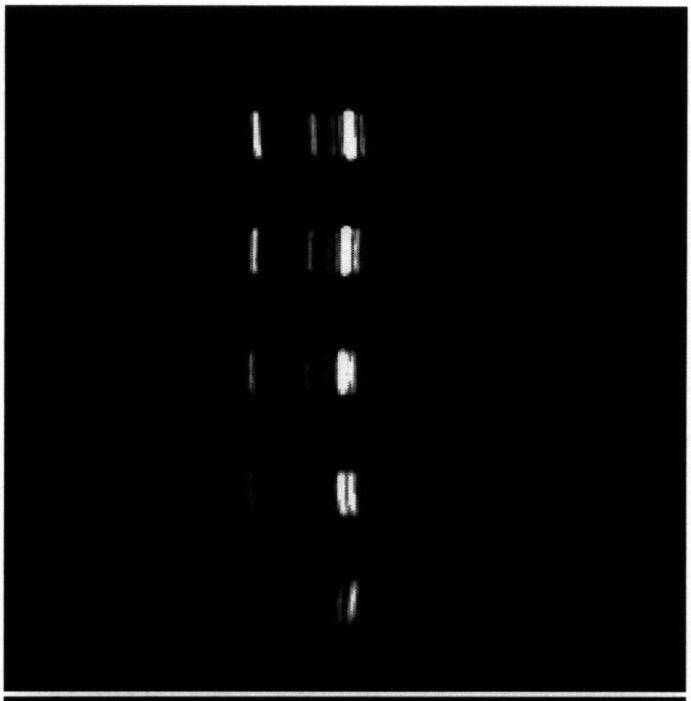

(d).

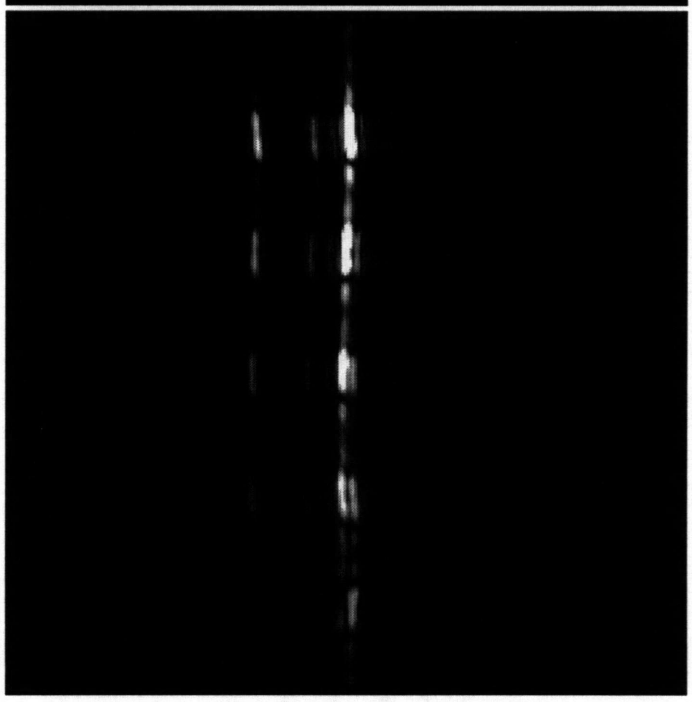

Figure 5.2. (c): Second echo CPMG spectroscopic image with TE of 156 ms. **(d):** 3-echo train RARE spectroscopic image with effective TE of 156 ms. The phase artifact that appears as blurring along the vertical direction is caused by different T2 weighting for each phase encoding step in the echo train.

(c).

(d).

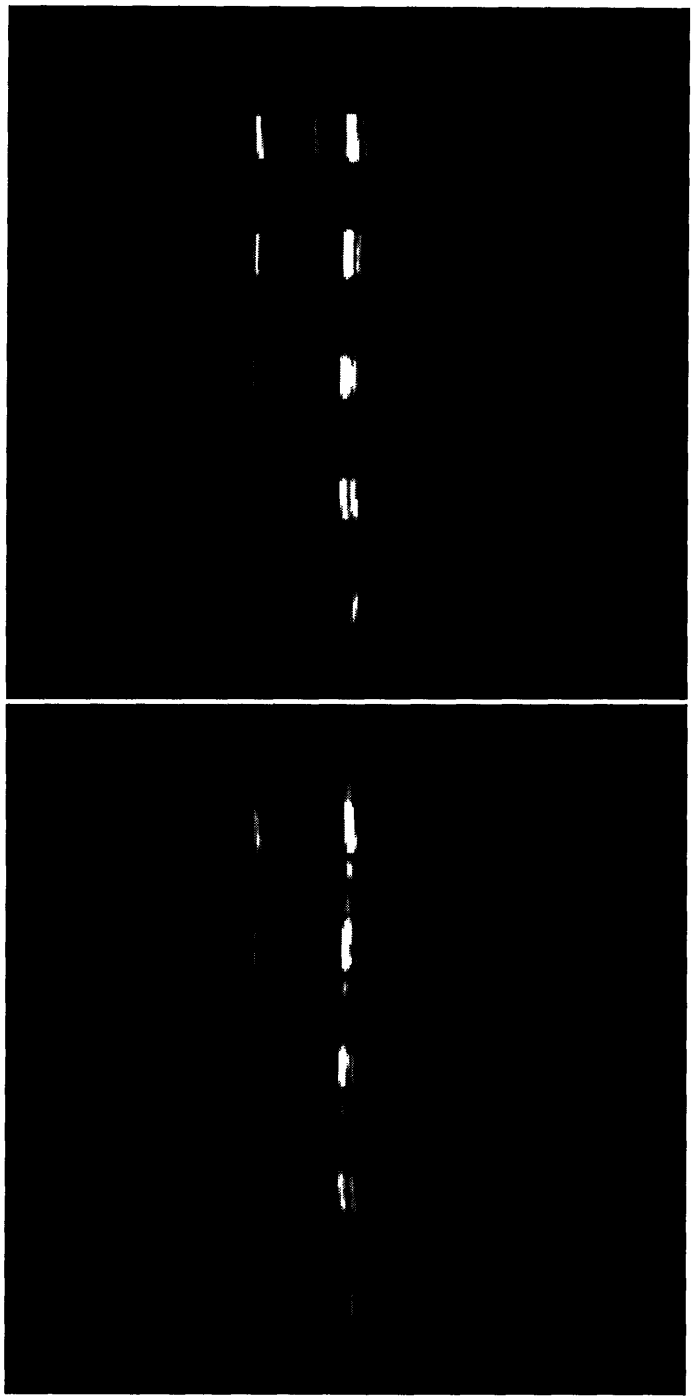

Figure 5.2. **(c):** Second echo CPMG spectroscopic image with TE of 156 ms. **(d):** 3-echo train RARE spectroscopic image with effective TE of 156 ms. The phase artifact that appears as blurring along the vertical direction is caused by different T2 weighting for each phase encoding step in the echo train.

Figure 5.3 shows the first and second echo spectra extracted from a voxel of pure fishoil denoted by the arrow in Figure 5.2 (b). The numbers in the graph represent the resonance peaks defined in Section 5.2. Peak #1 is assigned as the olefinic proton (-CH=CH-) at 5.6 ppm, peak #4 is the proton in between the double bonds (=C-CH_2-C=) at 2.9 ppm, peak #5 is the proton that adjacent to carboxyl (O=C-CH_2-) at 2.4 ppm, peak #6 is the proton that α to double bond (-C=C-CH_2-) at 2.0 ppm, peak #7 is methylene proton $(-CH_2-)_n$ at 1.2 ppm, peak #8 is terminal methyl ($-CH_3$) at 0.9 ppm, peak #9 is the proton second next to carboxyl (O=C-CH_2-$\underline{CH_2}$-) at around 1.5 ppm.

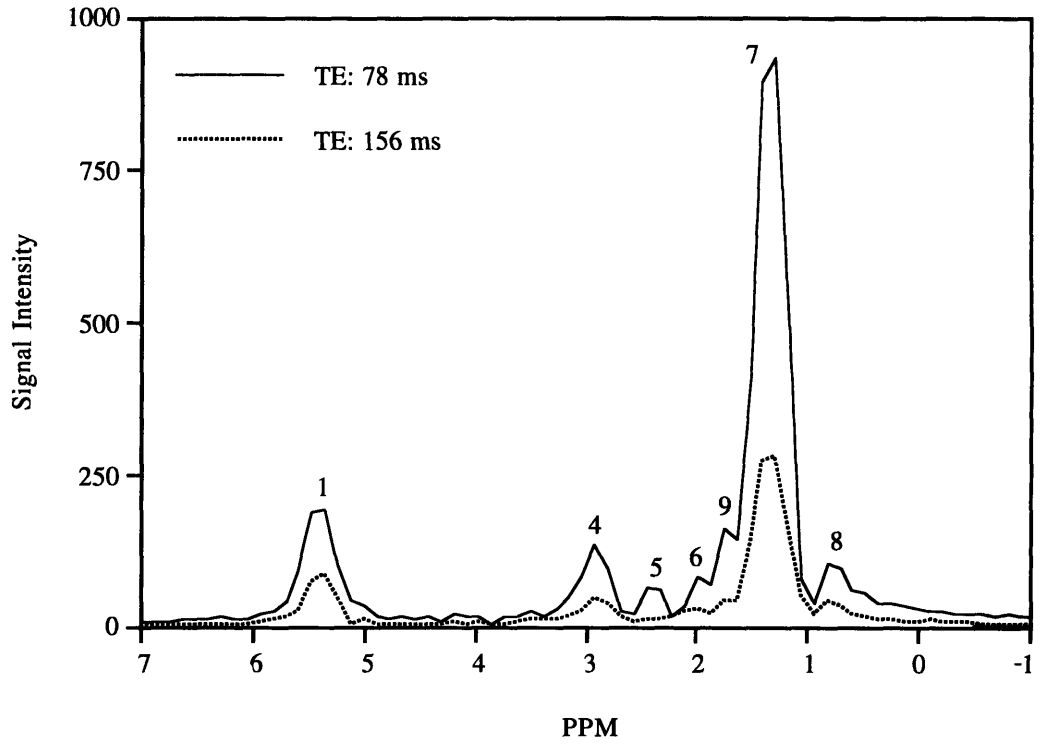

Figure 5.3: Spectra extracted from pure fishoil at the arrow location as in Figure 5.2(l for the first and second echoes with TEs of 78 ms and 156 ms. The numbers represent the resonance peaks defined in Section 5.2.

5.4 Inversion Recovery Spectroscopic Imaging: Lipid T_1 Relaxation Time and Terminal Methyl Detection

5.4.1 Introduction

This section presents the inversion recovery line scan RARE spectroscopic imaging techniques and their applications *in vivo* and *in vitro*. The lipid T_1 relaxation times in healthy adult yellow marrow were measured. Inversion pulse nulls the methylene signal and the terminal methyl signal is detected even with a limited spectral resolution (echo readout) [7].

In vivo methods for mapping spectral relaxation times and relative concentrations of methyl, methylene, and olefinic protons contain information related to triglyceride chain lengths and unsaturation. If performed in clinically acceptable scan times, they may prove useful for diagnosing or non-invasively monitoring disorders of lipid metabolites. To characterize T_1 values for lipid signals in bone marrow, the line scan RARE spectroscopic imaging technique described in Chapter 3 was modified with an inversion preparation pulse. As in short-tau inversion recovery imaging technique [8], a non-selective 180° pulse is placed before the regular line scan spectroscopic sequences. For each inversion time (TI), spectra from 128 voxels along the selected tissue column were acquired in 1.5 minutes. Data from over 10 TIs were acquired for spectral T_1 relaxation analysis in under 20 minutes. At a properly chosen TI, the inversion recovery nulls the large methylene signal in yellow marrow. Therefore the relatively smaller terminal methyl signal is detected even with the limited spectral sampling window required for multiple spectroscopic echo collections.

5.4.2 Materials

Studies were performed on a 1.5 T GE Signa system. The line scan RARE spectroscopic imaging sequence consisted of a 3 echo train, 48 ms echo spacing and 32 ms

echo readout. The sequence was preceded by a non-selective 180° pulse with a variable TI. Mutually orthogonal slice selective excitation and refocusing pulses confined the spectroscopic echoes (32 Hz resolution zero filled to 16 Hz) to spins within a 5×5 mm^2 column. The dimension along the column (FOV of 20 cm) was encoded using distinct phase encode gradients for each echo, yielding 3 k-space lines per TR. The lowest phase encode gradients were assigned to the second echo, resulting in an effective TE of $2 \times 48 =$ 96 ms. A TR of 2 second and a total of 128 phase encodes resulted in a scan time of 1 minute and 26 seconds.

Data sets were collected form columns parallel to lower extremity long axis centered on the knees. Four healthy volunteers were studied using up to 14 TI values from 50 to 1200 ms. Olefinic and methylene peak areas from over 50 voxels of yellow marrow for every volunteer were measured as functions of TI to estimate T_1 values. *In vitro* studies of fish oil (Natures Bounty, Bohemia, NY) and corn oil (Mazola, CPC international, Cliffs, NJ) were also performed.

5.4.3 Results

Figure 5.4 shows the methylene and olefinic proton intensity (peak area) in bone marrow of a 55-year-old healthy man versus inversion time. (a) is inversion recovery T_1 relaxation curve for methylene protons and (b) is olefinic proton. The error bars come from averaging of a few voxels in bone marrow along the tissue column. The solid lines represent a best non-linear fit of the form: $y = M_1 - M_2 \exp(-x / T_1)$, where M_1 stands for the initial magnetization after the inversion pulse. The fitted T_1 (mean $\pm$ SD) is 288 $\pm$7 ms for methylene proton and 460 $\pm$ 98 ms for olefinic proton.

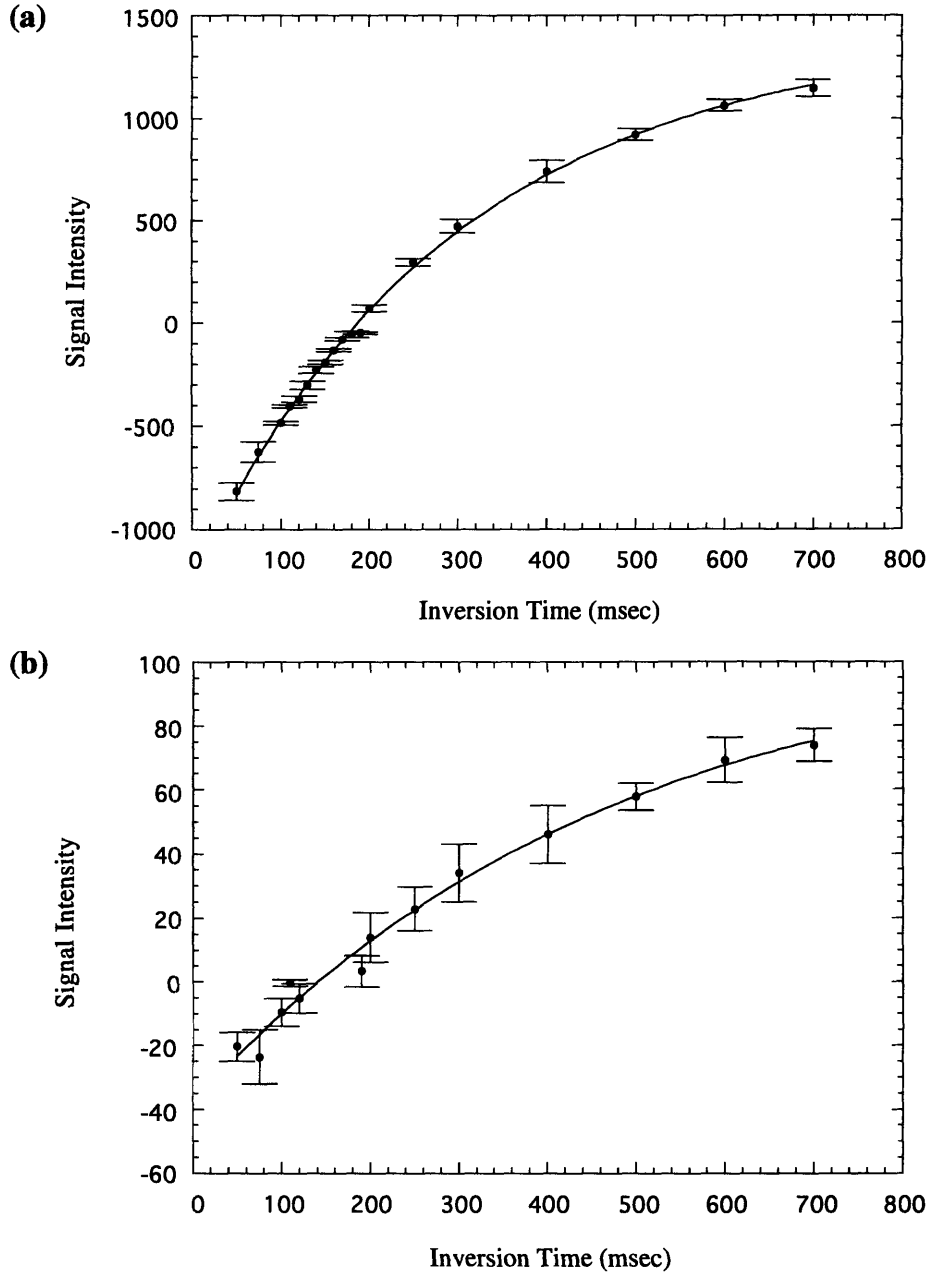

Figure 5.4: Signal intensity (peak area) versus inversion time in bone marrow of a 55-year-old man. (a). The methylene proton. (b). Olefinic (vinyl) proton. The solid line is a best non-linear fit to the data with y= m1- m2*exp(-x/T1).

Table 5.2 reports methylene and olefinic proton T_1 values of healthy adult yellow marrow and the two oil samples. The methylene T_1 in marrow was found to be slightly longer those found in the oils. The marrow olefinic proton T_1 was intermediate to those found for the different oils. The longest olefinic proton T_1 values were observed in fish oil, consistent with a higher degree of unsaturation (high in w-3 fatty acids) and subsequent increased fluidity [6]. The methylene peak contains a small contribution from terminal methyl protons. The methyl peak was observed in all subjects at TI values which adequately nulled methylene signal.

	Methylene Proton	Vinyl Proton
Yellow Marrow	274 ± 27 ms	348 ± 84 ms
Corn Oil	227 ± 11 ms	233 ± 27 ms
Fish Oil	202 ±12 ms	476 ± 39 ms

Table 5.2: Methylene and vinyl proton T_1 values of healthy adult yellow marrow and samples of fish oil and corn oil.

Figure 5.5 illustrates the *in vivo* marrow spectra acquired at TI values of 160 to 200 ms. The persistent signal at 0.9 ppm as the large methylene peak passes through a null is attributed to terminal methyl protons with unspecified, but longer, T_1 values as compared to methylene protons. Note from TI of 160 ms to 180 ms, the methylene peak is nulled gradually. At TI of 180 ms, the inversion pulse nulls the methylene peak almost completely and the methyl peak dominates the spectral range between 0 to 2 ppm.

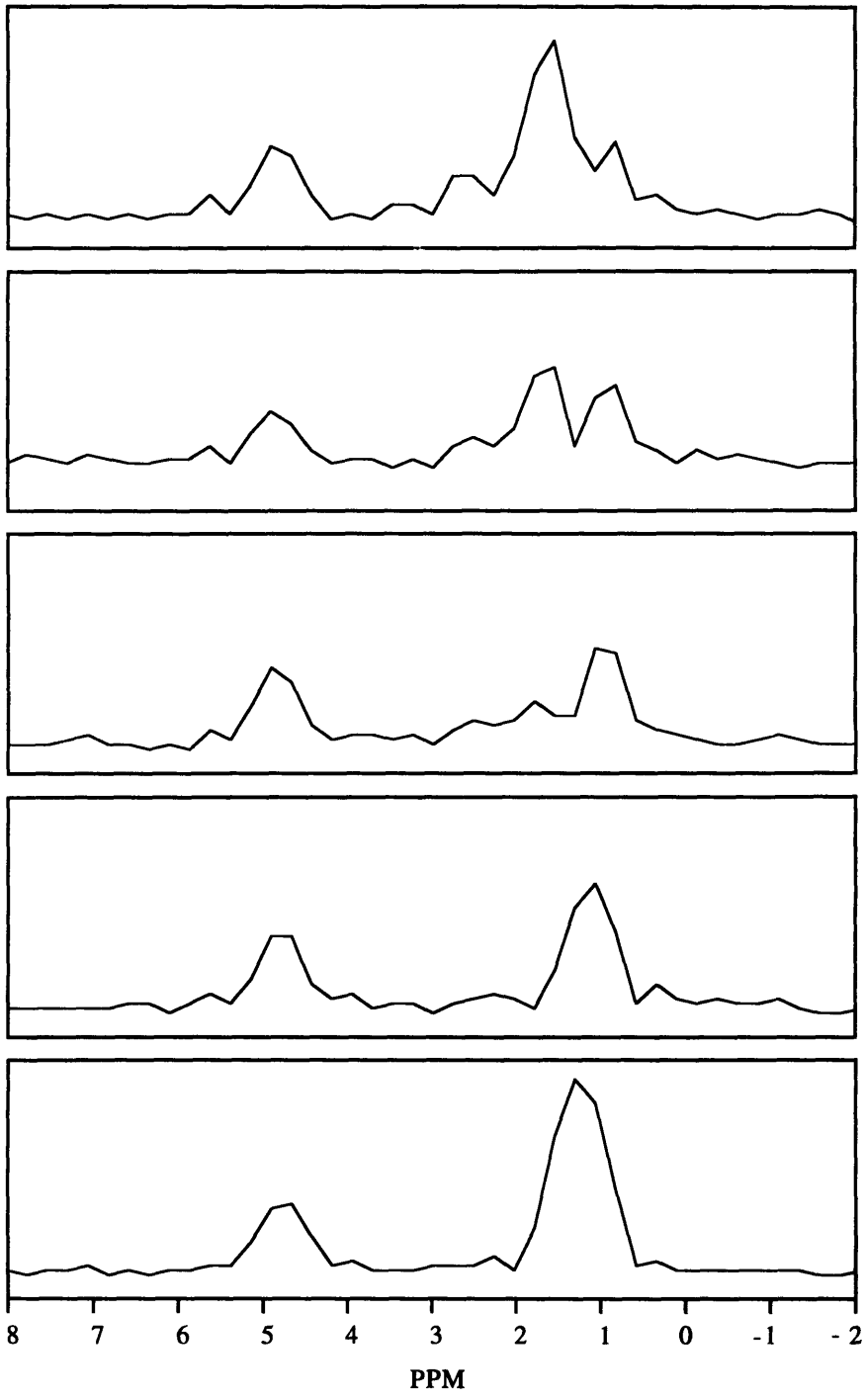

Figure 5.5: *In vivo* yellow marrow spectra at TI values 160, 170, 180,190 and 200ms, bottom to top. Spectra are extracted from each voxel of 0.04 cc and averaged over neighbouring four voxels. The signal at 0.9 ppm is attributed to terminal methyl protons as the methylene protons pass through a null around TI = 180 ms.

(a).

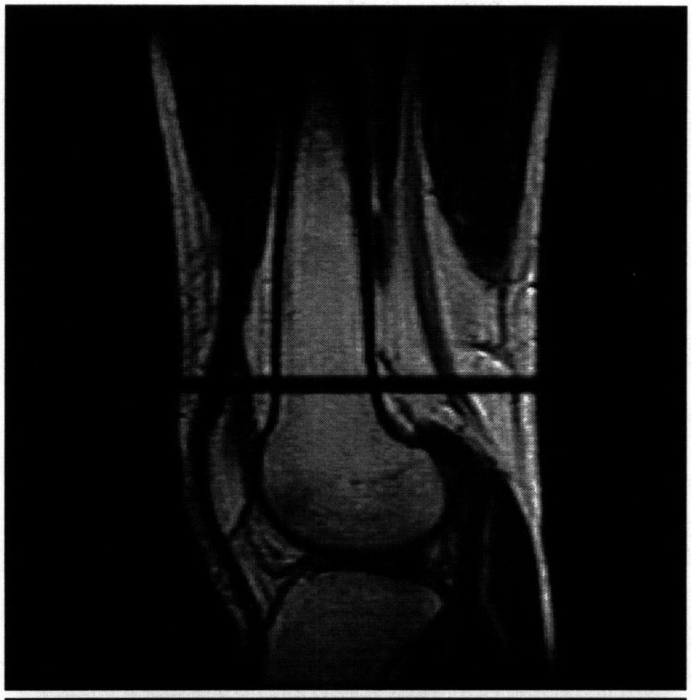

(b).

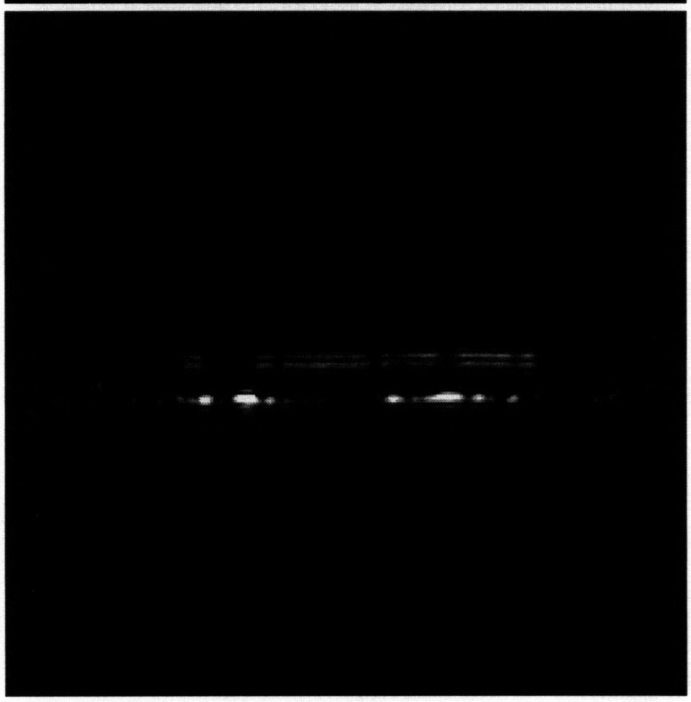

Figure 5.6. (a): A sagittal slice of the knee from a 55-year-old man. The column selection appears as a dark band. **(b):** 3-echo-train RARE spectroscopic image with a non-selective inversion pulse. TI is 190 ms. The effective TE is 96 ms and the echo readout is 32 ms.

(c).

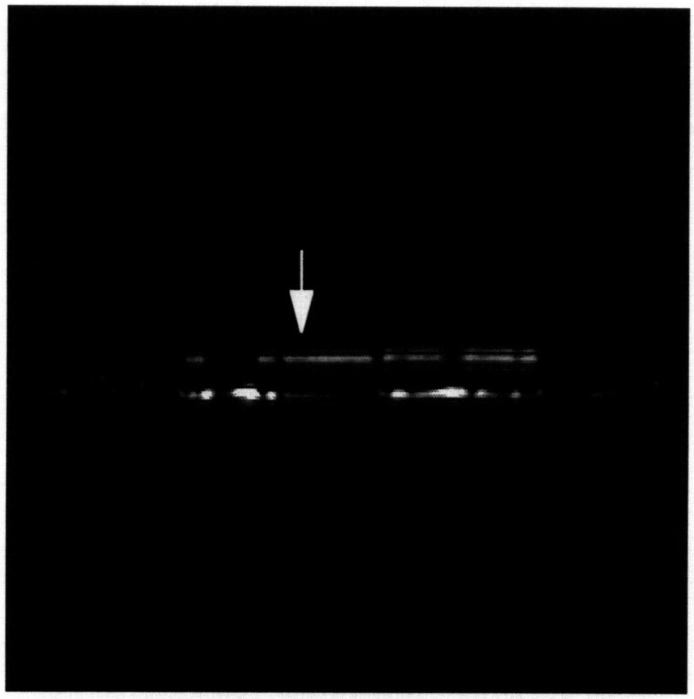

(d).

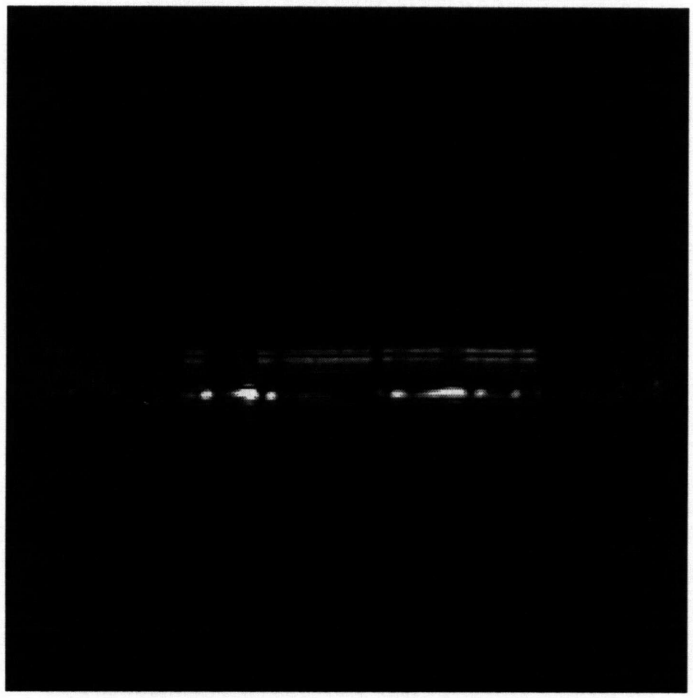

Figure 5.6: First echo (**c**) and second echo (**d**) CPMG spectroscopic image with a non-selective inversion pulse. TI is 190 ms and the spectral read out is 32 ms. TEs are 48 ms for (**c**) and 96 ms for (**d**).

(c).

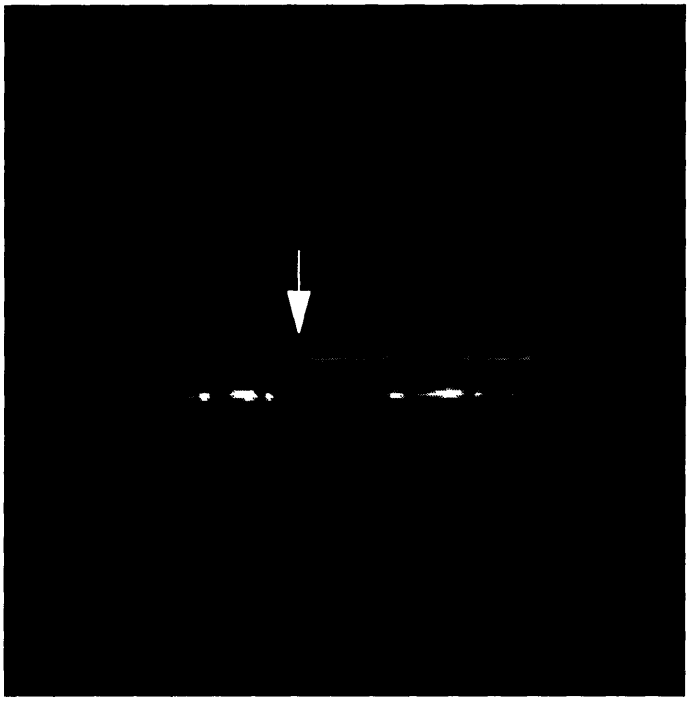

(d).

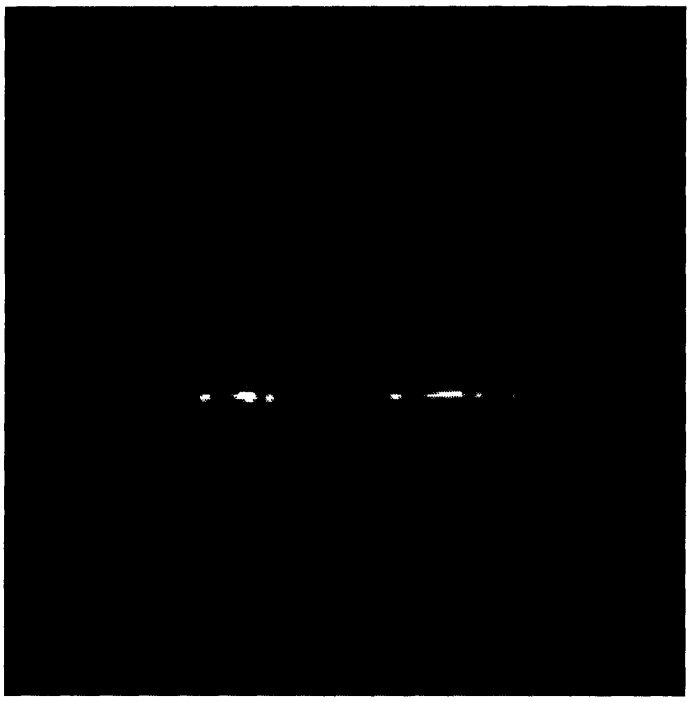

Figure 5.6: First echo (**c**) and second echo (**d**) CPMG spectroscopic image with a non-selective inversion pulse. TI is 190 ms and the spectral read out is 32 ms. TEs are 48 ms for (**c**) and 96 ms for (**d**).

Figure 5.7 is the spectra for the first four echoes extracted from the arrow location in Figure 5.6 (c). The TEs are 48, 96, 144, and 192 ms for four echoes respectively. The spectra are extracted and averaged over neighboring 4 pixels to increase the signal-to-noise ratio. Note that methylene peak (1.3 ppm) decays faster than methyl peak (0.9 ppm), which implies methyl protons have a longer T_2 value than methylene protons.

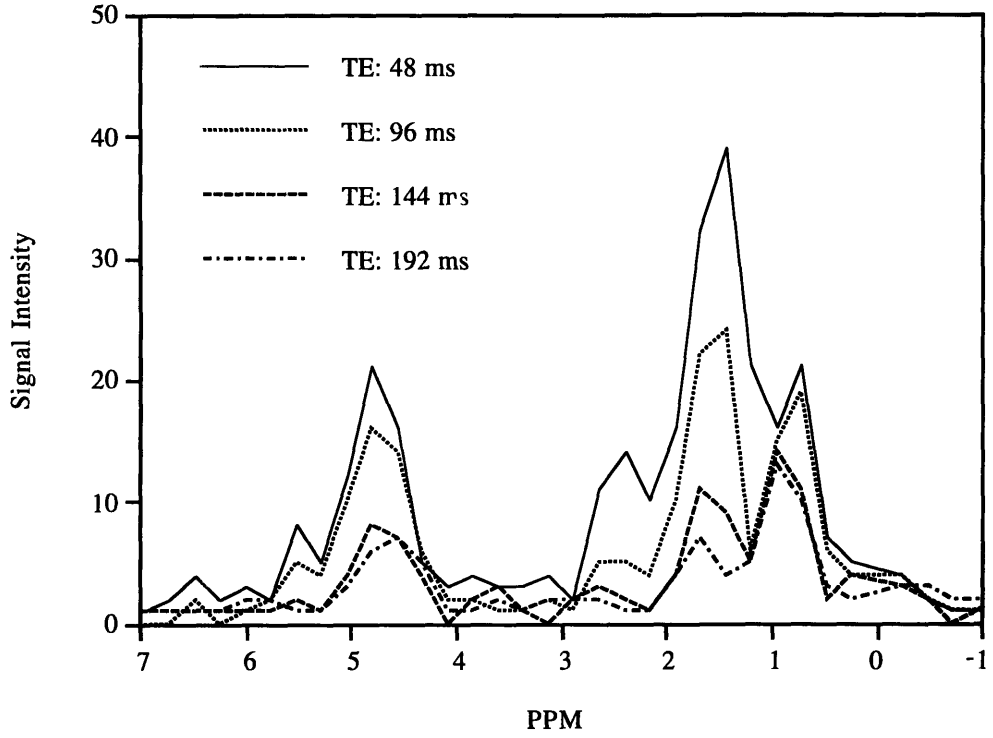

Figure 5.7: The spectra extracted from the arrow location. The inversion pulse nulls the methylene peak (1.3 ppm), so methyl peak (0.9 ppm) is visible even for 32 ms spectral read.

5.5 Assessing Triglyceride Unsaturation

5.5.1 Introduction

This section demonstrates the line scan CPMG spectroscopic imaging techniques in assessing the degree of triglyceride unsaturation *in vivo* and *in vitro* [9, 10].

Non-invasive assessment of triglyceride chemical compositions *in vivo* may be useful for monitoring patients with abnormalities in fat absorption and metabolism. Several investigators have discussed the clinical significance of measuring the degree of unsaturation among triglycerides for monitoring dietary compliance in patients with vascular disease or for assessing abnormal fatty acid metabolism in cystic fibrosis patients, using ^{13}C NMR [11-13]. In addition to overall unsaturation, ^{13}C can also be used to measure the degree of mono- versus poly-unsaturated fatty acids. However, the low sensitivity makes extensive tissue sampling difficult in clinically acceptable scan times at routine imaging field strengths [11].

The line scan CPMG spectroscopic imaging techniques are capable of measuring an index which associated with the degree of unsaturation in triglycerides. The index is the ratio of olefinic proton signal to combined methylene /methyl proton signal. The rationale is that the olefinic proton peak arises solely from unsaturated fatty acids while the methylene/methyl peak arises from both saturated and unsaturated fatty acids. For every double bond created in the triglyceride aliphatic backbone, two protons are added to the olefinic signal and four protons are directly removed from methylene signal. Therefore, the ratio of these two peaks is sensitive to the overall degree of unsaturated versus saturated fatty acids.

The techniques were applied to yellow marrow of healthy adult volunteers from which the index in many small voxels within yellow marrow was measured. Control

values for olefinic to methylene/methyl ratios in healthy adult yellow marrow are reported. The sensitivity of the ratio to degree of triglyceride unsaturation is demonstrated *in vitro*.

5.5.2 Materials

Proton spectroscopic imaging was performed with the 1.5T GE Signa scanner using a 8 echo line scan CPMG spectroscopic imaging sequence. Each echo was phase encoded for spatial information along the selected tissue column and unwound following readout in the absence of gradients. Final data sets consisted of spectra from 128, $5 \times 5 \times 1.6$ mm^3 voxels along the column at echo time from 48 to 384 ms with a spectral resolution of 32 Hz zero filled to 16 Hz. Acquisition time was 4 minutes and 18 seconds using a 2 s TR and 128 phase encodes. The knees of 8 healthy adult volunteers were studied. Multi-echo spectra from voxels within marrow were fitted with Gaussian functions. Peak percentages were calculated from peak areas extrapolated to zero echo time, accounting for spectral T_2 decay differences as described in Chapter 3. The spectral assignments of olefinic, water and methylene/methyl peaks are the same as in Section 5.2. The alpha peak refered in this section is a composite lipid peak at 2.4 ppm. *In vitro* studies of fish oil and corn oil were also performed. High resolution proton ^1H spectra of the oils were obtained at 7 Tesla with a GE vertical bore spectrometer to confirm differences in the overall degree of unsaturation and for comparison with 1.5 Tesla proton spectroscopic imaging.

5.5.3 Results

Percentage contributions to the healthy adult yellow marrow spectra, as averaged over 8 volunteers and over 50 marrow voxels per volunteer are shown in Table 5.3. The olefinic to methylene/methyl extrapolated peak area ratio was 0.08 ± 0.02.

	Percentage (average ± SD)
Olefinic Protons	6.4 ± 0.4 %
Water Protons	4.2 ± 1.5 %
Alpha Protons	7.2 ± 0.5 %
Methylene/Methyl Protons	82.2 ± 1.9 %

Table 5.3: Relative percentage of proton peak areas in adult yellow marrow. The percentage values are the average of 8 healthy adult volunteers.

Table 5.4 reports the ratio of olefinic peak area to combined methylene/methyl peak area for fish and corn oil obtained in 7 T ^{1}H spectrometer and 1.5 T clinical scanner. The measurements at high field (7 T) and conventional field (1.5 T) ^{1}H spectroscopy confirmed the presence of more unsaturated fatty acids in fish oil than in corn oil.

	Spectroscopy at 7 T	Spectroscopic Imaging at 1.5 T
Corn Oil	0.14	0.13 ± 0.01
Fish Oil	0.26	0.24 ± 0.02

Table 5.4: The ratio of olefinic peak area to methylene/methyl peak area in oil samples. The listed ratios are obtained from spectroscopy measurement on a 7 T spectrometer and line scan CPMG spectroscopic imaging measurement on a 1.5 T clinical scanner.

5.6 Discussion

Previous proton spectroscopic studies of bone marrow have focused assessing water versus saturated fat content for monitoring hematologic disease [14]. Assessing lipid chemical composition non-invasively may have even more widespread utility from an overall medical perspective [15]. Though single voxel proton spectroscopy may be applied towards this end [5, 14], the advantage of a line scan spectroscopic approach is increased volume coverage and reduced voxel size, the latter being useful for minimizing susceptibility induced intra-voxel dephasing in studies of marrow within trabecular bone [14].

Spectral T_1 relaxation measurements of lipid peaks in yellow can be made throughout the knee in many small voxels in reasonable scan times using spectroscopic RARE techniques. Spectral resolution is limited and can only be improved at the expenses of increased T_2 weighting because longer readouts increase echo spacing. As such, the small methyl peak adjacent to the large methylene peak was previously unresolved with 32 ms readouts [16]. Inversion pulses at TIs similar to those used for STIR imaging [8] allow for methyl signal observation even with the limited spectral resolution required for spectroscopic RARE acquisitions. Nulling the methylene signal in this manner allows for T_2 measurement of the methyl signal at relatively short echo spacings with CPMG spectroscopic sequence.

As currently implemented, the line scan techniques provide a measure of the ratio of olefinic to methylene/methyl protons in yellow marrow, a chemical index sensitive to the degree of unsaturation among the triglycerides. In most red marrow sampled, however, the spectral resolution afforded by the 32 ms echo readouts was not sufficient to separate resolve the olefinic proton contribution from the dominant water peak. Better spectral would be required for this task as well as for assessing the degree of mono - versus poly-unsaturated triglyceride levels. In this case, a peak at 2.8 to 3.0 ppm from CH_2 groups

between double bonds [5] must be resolved and quantified, thus allowing for a measurement of a proton peak arising solely from polyunsaturated fatty acids. With the present spectral resolution, this peak is just one of several resolved peaks contributing to the alpha peak.

References

1. Chapman D, Goni FM. Nuclear magnetic resonance spectra. The lipid handbook. London: Chapman and Hall, 1986; 406-421.

2. Henrikson KP. Nuclear magnetic resonance spectroscopy of lipids. Biochemistry and methodology of lipids. New York, Wiley-interscience, 1971; 243-249.

3. Rosen BR, Fleming DM, Kushner WP, Wismer GL, Brady TJ. Hematologic bone marrow disorders: quantitative chemical shfit MR imaging. Radiology 1988; 169:799-804.

4. Gussoni M, Greco F, Pegna M, Bianchi G, Zetta L. Solid state and microscopy NMR study of the chemical constituents of Afzelia cuanzensis seeds. Magn. Reson. Imag. 1994; 12: 477-486.

5. Brix G, Heiland S, Bellemann ME, Koch T, Lorenz WJ. MR imaging of fat-containing tissues: valuation of two quantitative imaging techniques in comparison with localization proton spectroscopy. Magn. Reson. Imaging. 1993; 11: 977-991.

6. Stryer L. Biochemistry, 3rd edition, W. H. Freeman and Company, New York, 1988.

7. Meng J, Oshio K, Williamson DS, Mulkern RV. Inversion recovery spectroscopic imaging of bone marrow: lipid T_1 relaxation and terminal methyl detection. Book of Abstracts, Second Meeting of SMR, Volume 1, Page 180, 1994.

8. Jones KM, Unger EC, Granstrom P, et al. Magn Reson Imag. 1992; 10:169.

9. Mulkern RV, Meng J, Oshio K, Jaramillo D, Williamson DS. In vivo measurements of lipid chemical composition in bone marrow with a line scan CPMG ^1H spectroscopic imaging method. Book of Abstracts, ENC, 1995.

10. Mulkern RV, Lilly HS, Meng J, Bowers J, Guttmann CRG, Oshio K, Williamson DS, Jaramillo D. Assessing triglyceride unsaturation with a proton spectroscopic imaging method: in vivo and in vitro studies. Book of Abstract, Second Meeting of SMR, Volume 1, Page 176, 1994.

11. Moonen CTW, Dimand RJ, Cox KL. The non-invasive determination of linoleic acid content of human adipose tissue by natural abundance carbon-13 nuclear magnetic resonance. Magn Reson Med 1988; 6: 140-157.

12. Beckman N, Brocard JJ, Keller U, Seelig J, Relationship between the degree of unsaturation of dietary fatty acids and adipose tissue fatty acids assessed by natural-abundance ^{13}C magnetic resonance spectroscopy in man. Magn Reson Med 1992; 27: 97-106.

13. Dimand RJ, Moonen CTW, Chu SC, Bradbury EM, Kurland G, Cox KL. Adipose tissue abnormalities in cystic fibrosis: Non-invasive determination of mono- and poly-unsaturated fatty acids by carbon-13 topical magnetic resonance spectroscopy. Rediatr Res 1988; 24: 243-246.

14. Ballon D, Jakubowski A, Gabrilove J, Graham MC, Zakowski M, Sheridan C, Koutcher JA. In vivo measurements of bone marrow celularity using volume-localized proton NMR spectroscopy. Magn Reson. Med. 1991; 19:85-95.

15. Gunstone FD, Harwood JL, Padley FB. The lipid handbook, Chapman and Hall, London, 1986.

16. Oshio K, Mulkern RV. Rapid fat/water assessment in knee cavity bone marrow by inner volume spectroscopic imaging with RARE. JMRI 1992; 2: 601-604.

Chapter 6

Applications: Human Brain Metabolites

The studies in previous chapters were mainly on bone marrow, designed to quantification of the cellularity and the lipid chemical composition. In this chapter the line scan CPMG and RARE spectroscopic imaging methods, implemented on the standard 1.5 T clinical scanner, are applied to map brain metabolite signals and to estimate metabolites T_2 relaxation values. Multiple spectroscopic images from a selected tissue column through the brain are obtained in scan time of less than 10 minutes. The potential to improve signal-to-noise ratios by adding data from several different echoes is examined. Separate acquisitions with the line scan RARE spectroscopic imaging methods are shown to provide column maps of major brain metabolites in 90 seconds. Due to the inherent tradeoffs between T_2 decay, spectral resolution and echo spacing in application to the brain, separate quantification of choline and creatine resonances is not achieved with the present implementation. Instead, combined choline + creatine (Cho + Cr) resonance is quantified in the brain studies, as well as the N-acetyl aspartate (NAA) resonance.

The goal of this chapter is to demonstrate the ability to make rapid line scan spatial metabolite maps in 90 seconds or to collected data sets suitable for T_2 decay analyses of Cho+ Cr and NAA resonances in under 10 minutes, features which may prove of practical clinical utility in the diagnosis and monitoring of brain pathologies. This chapter begins with a review on biochemical functions of major metabolites in human brain. It is followed by our studies on brain metabolites using the line scan CPMG and RARE techniques. The chapter concludes with a discussion on the limitations and potential uses of the methods as applied to the brain.

6.1 Function of Major Metabolites in Brain

This section provides some relevant biochemical background about the major resonance peaks observed in ^{1}H spectroscopy. Some of the materials are from a review paper on ^{1}H spectroscopy by Miller [1]. The chemicals contributing to the three main peaks are: N-acetyl-aspartate (NAA), creatine/phosphocreatine (Cr), and choline-containing compounds (Cho). NAA is attributed to the peak seen at shift of 2.0 ppm, Cr to 3.0 ppm, and Cho to 3.2 ppm.

Discovered in 1956, NAA is present within neurons although its biological function is largely unknown. Studies show that NAA level changes with different diseases. For example, NAA is 3 times higher in amyotrophic lateral sclerosis, a progressive degenerative disease affecting motor systems in brain and spinal cord, than in normal controls. The concentration of NAA decreases in non-neuronal tumor, such as chronic multiple sclerosis where there is a loss of axons. However, the level of NAA is normal in acute multiple sclerosis where there is no loss of axons. Also the excess NAA is shown partially responsible for certain degenerative disease in early childhood such as canavan disease. It is suggested the potential of NAA as neuronal marker to study various neuron diseases.

Creatine is from the diet and synthesized within the liver, kidney, and pancreas. Humans have approximately 120 g of creatine and creatine phosphate present in muscle and neurons. It serves as reserve for energy metabolism. The single peak measured at 3.0 ppm with ^{1}H spectroscopy consists of both creatine phosphate and creatine while ^{31}P NMR measures only creatine phosphate. It is suggested creatine peak be used as control value even though studies show that the creatine peak decreases on brain tumor and infectious brain masses.

Choline is a nutrient from most foods. Cho is associated with neurotransmitter that is critical for memory, cognition and mood. It is also a related the cell membrane. The Cho peak at 3.2 ppm in ^{1}H spectroscopy consists of a complex mixture of Cho-containing

compounds. Studies show that the Cho peak changes significantly with stroke, degenerative dementia, drug intake, and infectious and neoplastic brain masses. For example, Cho rises with brain ischemia and decreases with Alzheimer's disease.

The preliminary studies of *in vivo* ^{1}H spectroscopy have found increased Cho and decreased NAA and Cr peaks in tumors. ^{1}H MR spectroscopy shows great promises for aiding diagnosis of various brain diseases.

6.2 Studies of Brain Metabolites

6.2.1 Introduction

The detection and mapping of low concentration brain metabolites with proton MR spectroscopy is an evolving research field with potentially important clinical applications. Measurement of signals from choline containing compounds, total creatine, N-acetyl-aspartate, and lactate has proven feasible at the routine clinical imaging field strength of 1.5 Tesla. Though the studies are of an inherently low signal-to-noise nature, chemical signatures from brain metabolites obtained with proton spectroscopic studies may ultimately prove useful in diagnosing or monitoring the effects of therapy in a number of brain disorders such as tumors [2-6], stroke [7, 8], multiple sclerosis [9], and neurodegenerative disorders [10-12].

Single voxel acquisitions based on the STEAM and PRESS sequences have played important roles in determining the fundamental characteristics of proton brain spectra [13-18]. However, dramatic increases in the extent of spatial coverage and spatial resolution can made using chemical shift imaging principles [19] based phase encoding STEAM, PRESS or spin echo signals [20-23]. Such techniques are becoming increasingly more common in the study of brain disorders with proton MR spectroscopy [3, 4, 11].

The line scan CPMG and RARE spectroscopic imaging sequences used for brain metabolites studies are a modified version of sequences described in Chapter 3.

The water concentration in the brain is about 40 - 50 M (mole per litter) while the concentrations of the brain metabolites are in the order of 10 mM. So the signals from metabolites are about 5000 times smaller than that from water. Due to the limited dynamic range the strong lipid signal from the skull, it is impossible to observe the small metabolite peaks without water and lipid suppression using the sequences shown in Chapter 3. Figure 6.1 represents the spectroscopic image of a column across the brain without the water suppression and lipid saturation. The huge water signal and lipid signals make the direct observation of low concentration brain metabolites impossible.

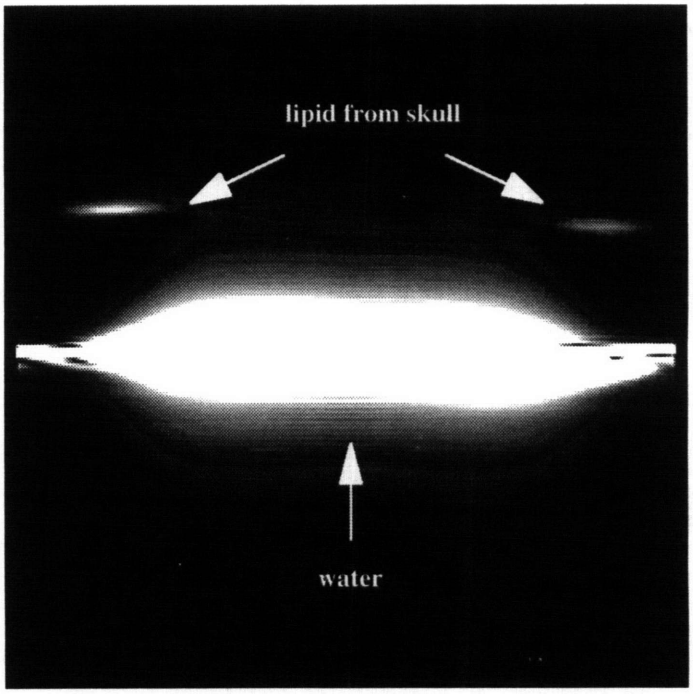

Figure 6.1: A spectroscopic image of a column oriented across the brain from left to right without the water suppression and lipid nulling.

Figure 6.2 shows the modified line scan CPMG sequence that is capable of detecting the low concentration brain metabolites. The primary modifications include the

The line scan CPMG and RARE spectroscopic imaging sequences used for brain metabolites studies are a modified version of sequences described in Chapter 3.

The water concentration in the brain is about 40 - 50 M (mole per litter) while the concentrations of the brain metabolites are in the order of 10 mM. So the signals from metabolites are about 5000 times smaller than that from water. Due to the limited dynamic range the strong lipid signal from the skull, it is impossible to observe the small metabolite peaks without water and lipid suppression using the sequences shown in Chapter 3. Figure 6.1 represents the spectroscopic image of a column across the brain without the water suppression and lipid saturation. The huge water signal and lipid signals make the direct observation of low concentration brain metabolites impossible.

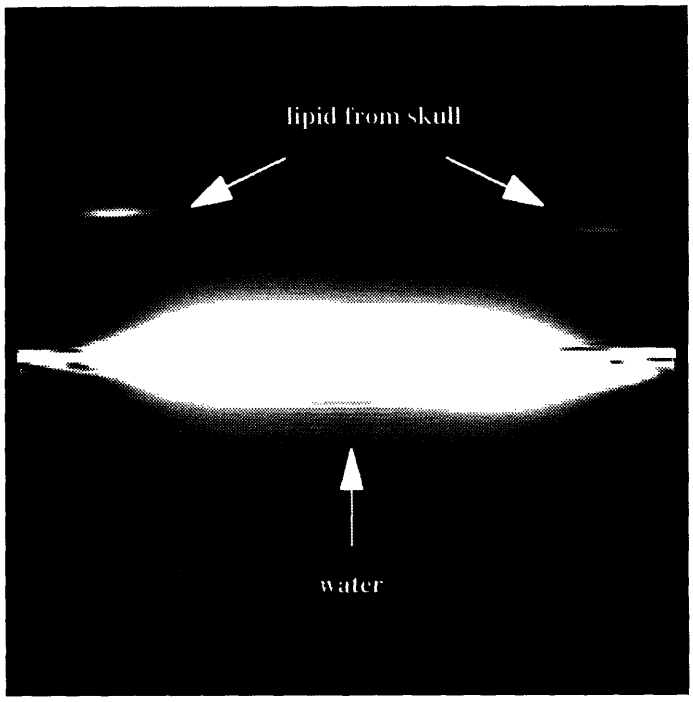

Figure 6.1: A spectroscopic image of a column oriented across the brain from left to right without the water suppression and lipid nulling.

Figure 6.2 shows the modified line scan CPMG sequence that is capable of detecting the low concentration brain metabolites. The primary modifications include the

placement of a non-selective inversion pulse as in STIR imaging technique [31] and three chemical shift selective (CHESS) pulses [32]. The non-selective 180° (3 ms one-side lobe sinc) pulse placed 175 ms prior to the excitation pulse of the CPMG sequence reduces the lipid signal from the skull. The CHESS pulses (20 ms sinc, ±75 Hz bandwidth) that are applied between the inversion pulse and the excitation pulse of the CPMG sequence flip the water protons 90° degree into the transverse plane. The following spoiling gradients dephase the water protons along x, y and z directions. As the coherence of the water protons is destroyed, the small metabolites signals can be picked up by the receivers.

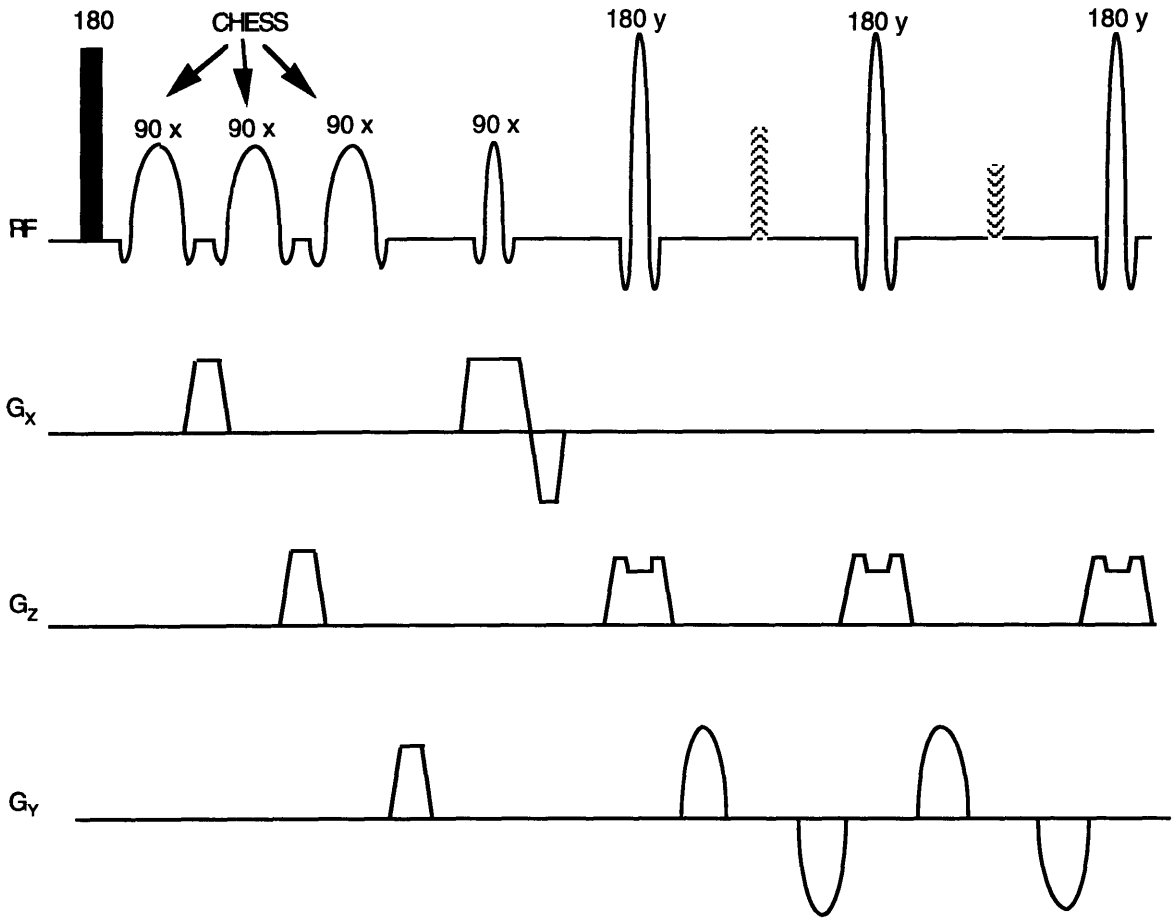

Figure 6.2: Line scan CPMG spectroscopic imaging sequence modified for brain study. A non-selective 180 pulse nulls the skull lipid signal. Three CHESS pulses suppress the water signal. Echoes are then collected without readout gradients. Only 2 echoes are shown.

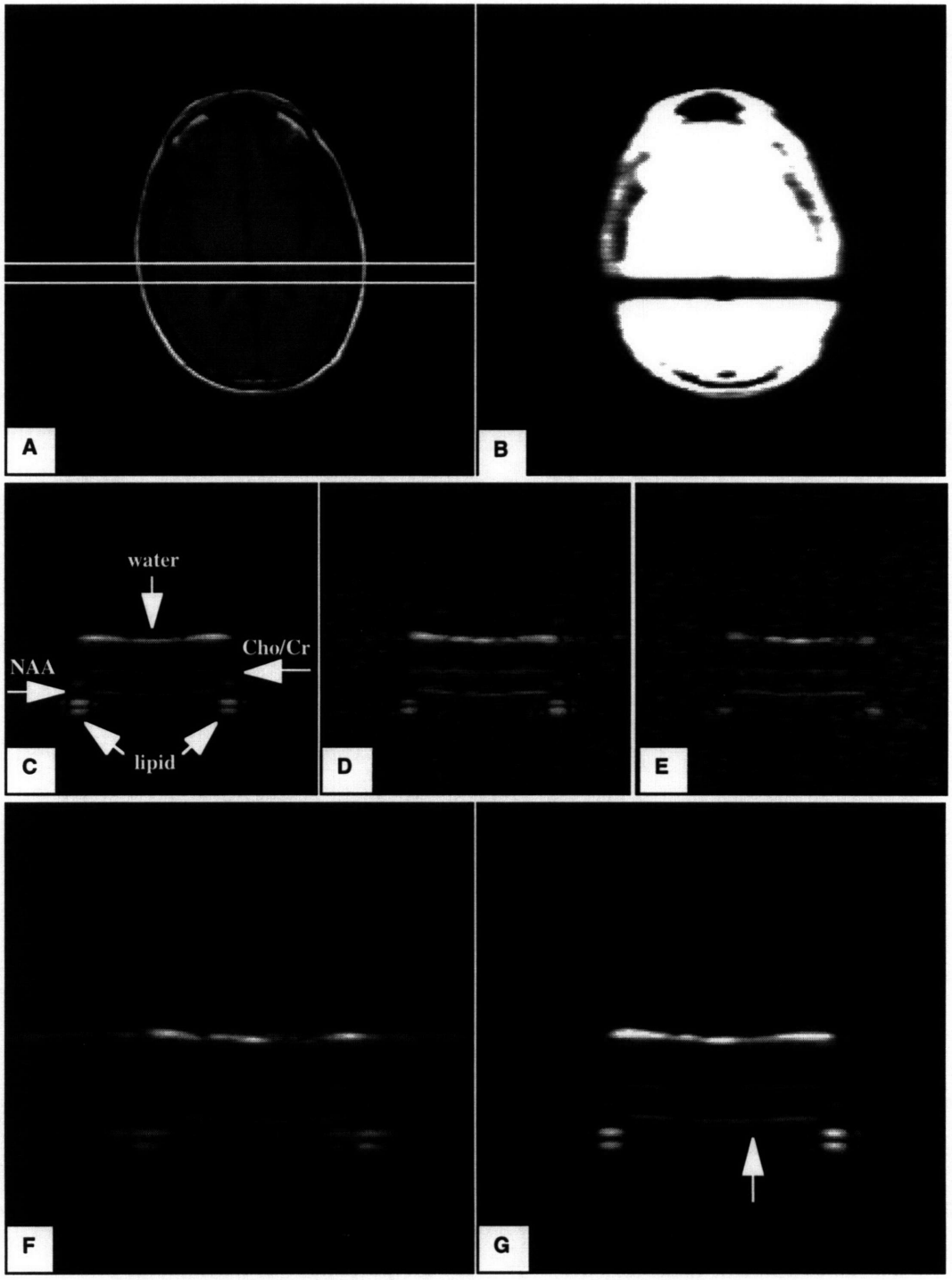

Figure 6.3. Images from a healthy 38-year-old man. **(a):** T1-weighted localizing image depicts the 15 mm thick column. **(b):** A 4 s scan scout image confirms the column with a dark band. The very bright signal is a consequence of the multiplicative factor of 350 applied to the sampled data. **(c-e):** CPMG spectroscopic images of first 3 echoes. TEs are 145, 290, 435 ms respectively. **(f):** Image of 90 seconds 3-echo RARE scan. **(g):** A summation image generated by adding the first 3 echoes.

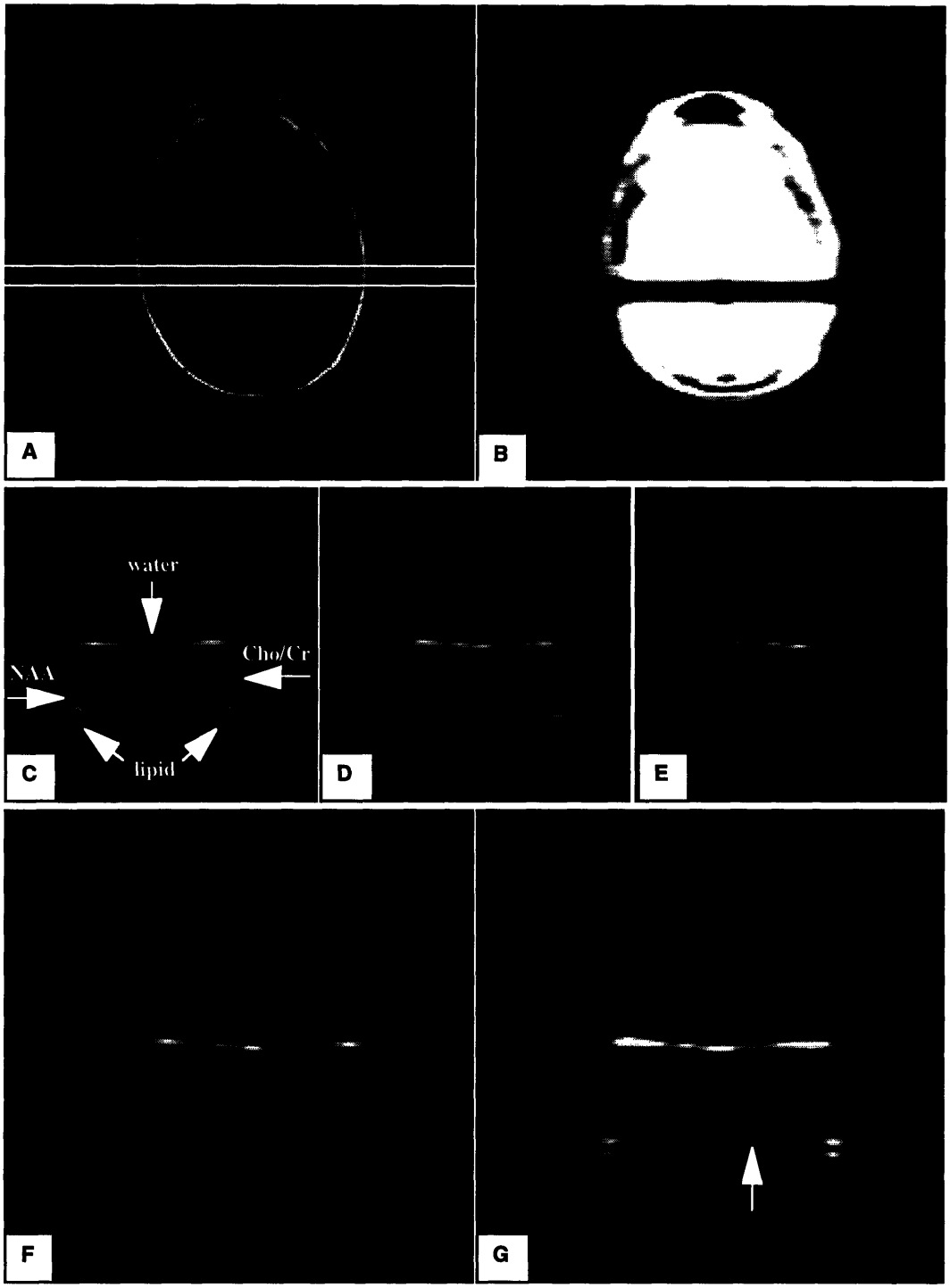

Figure 6.3. Images from a healthy 38-year-old man. **(a):** T1-weighted localizing image depicts the 15 mm thick column. **(b):** A 4 s scan scout image confirms the column with a dark band. The very bright signal is a consequence of the multiplicative factor of 350 applied to the sampled data. **(c-e):** CPMG spectroscopic images of first 3 echoes. TEs are 145, 290, 435 ms respectively. **(f):** Image of 90 seconds 3-echo RARE scan. **(g):** A summation image generated by adding the first 3 echoes.

is a 4 seconds scout image (5 echo RARE, 30 phase encodes, TR of 600 ms) used to quickly outline and confirm the position of the target tissue column with a dark saturation band. The very bright signal from unsaturated tissue is a consequence of the muliplicative factor of 350 applied to the sampled data for bringing up the low concentration metabolites. Several 15 seconds RARE spectroscopic scan of the column were run to optimize water suppression through minor adjustments of the third CHESS pulse amplitude.

Figure 6.3 (c - e) depict first 3 of 5-echo CPMG spectroscopic images of the column with signal readout setting of 128 ms. The echo times are 145, 290, 435 ms respectively. These images were acquired in 8 minutes and 42 seconds (8 signal averages, 30 phase encodes, 2 s TR). The absolute spectral resolution (vertical axis) is 8 Hz which is zero filled to 4 Hz. The nominal voxel size is $1.5 \times 1.5 \times 1$ cm^3 , or 2.25 cc and zero filling making an apparent spatial resolution of approximately 1.2 mm along the column. The arrows point the residual water resonance, the lipid resonance from the skull, the NAA, and the combined Cho+Cr resonance. Note that the spectral resolution is generally not sufficient to allow for independent quantification of the choline peak at 3.2 ppm and the total creatine peak at 3.0 ppm. Figure 6.3 (f) is the 90 seconds 3-echo RARE spectroscopic image of the column. The effective TE is 290 ms with echo readouts of 128 ms. Primary bands from brain metabolites are still detectable, though considerable spatial blurring due to the T_2 weighting of k-space data is observed. Note that despite the spatial blurring of lipid signal along the column, the lipid signal never intersects with the NAA band anywhere in the brain. Figure 6.3 (g) is a summation image from the first 3 echoes. It was generated by adding raw data of the first 3 echoes before Fourier transformation and magnitude reconstruction. The T_2 weighting of such image is given by TE and n, as defined in the previous section. Signal-to-noise ratio measured for NAA is an approximately 15% better than that from the first echo spectra in Figure 6. 3 (c) (SNR = 7.7 $\pm$ 1.3 vs SNR = 6.7 $\pm$ 1.5). Spectra from the RARE data at the same location (Figure 6.3 (f)) show decreased

SNR and increased lipid bleed, a phenomenon well-known from imaging studies with RARE [33, 34].

From the arrow location in Figure 6.3 (g), spectra averaged over four adjacent pixels along the column ($15 \times 15 \times 5$ mm^3 nominal voxel size) are plotted in Figure 6.4 for the first 3 echoes of the CPMG acquisition. The solid lines are the best fits to Gaussian functions for the residual water peak, the overlapping Cho+Cr peak, and the NAA peak. In adult volunteers studied with 5 echo CPMG sequence, the residual water peak, the NAA peak, and the combined Cho+Cr peak were generally quantifiable with Gaussian fitting at the first three echoes. The NAA peak generally persisted in the 4th and 5th echoes while the Cho+Cr peak was usually in the noise level at these later echoes. Peak areas extracted from these fits are used to estimate spectral T_2 relaxation values.

Figure 6.5 presents the spectral T_2 decay of the combined Cho+Cr peak area and the NAA peak area with echo time from the volunteer study in Figure 6.3. The plot was generated by averaging data from four $15 \times 15 \times 5$ mm^3 voxels along the column. T_2 relaxation times estimated are: 318 ms (combined Cho+Cr) and 357 ms (NAA).

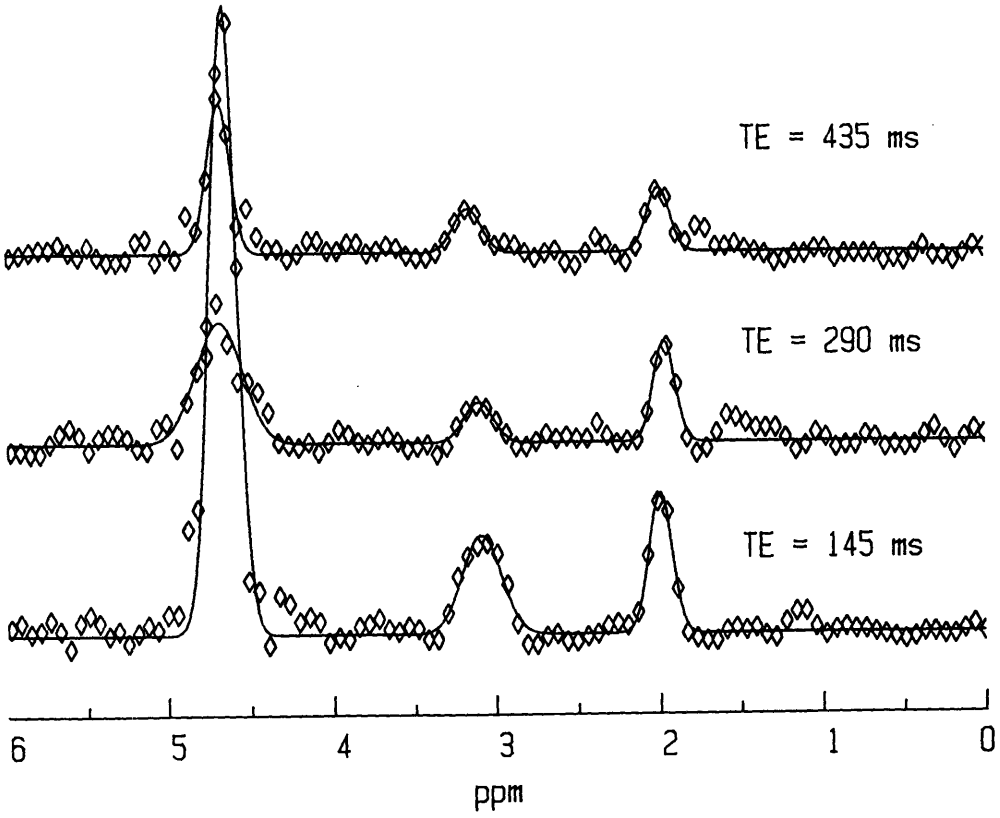

Figure 6.4: Magnitude brain spectra at the first 3 echoes of the 5-echo CPMG acquisition in Figure 6.3. These spectra were extracted at the spatial location pointed by the arrow in Figure 6.3 (g). Solid lines are the best fits to Gaussians.

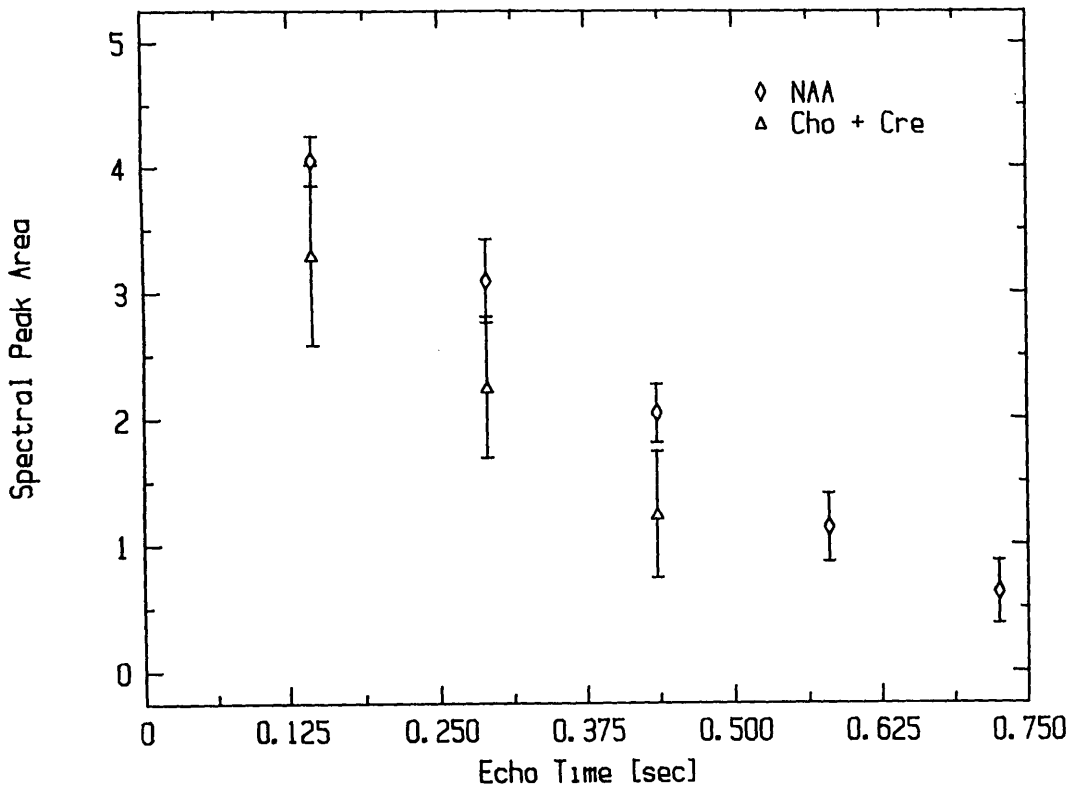

Figure 6.5: Spectral T2 decay of the combined Cho+Cr peak and the NAA peak as obtained from the data set of Figure 6.3. Note that the NAA signal was quantifiable even at the last two echoes with TEs of 580 and 725 ms respectively.

Figure 6.6 shows a spatial profile for water and NAA peaks along the column. The integrated water and NAA signal intensities as functions of position along the column are plotted. The water trace was taken directly from integration of signal intensity across the column dimension in the T_1-weighted image (Figure 6.3 (a)). The locations corresponding to the ventricles appear as dips in the water profile due to the T_1-weighting nature of this localizing image (TR/TE = 600/12 ms). The NAA trace was taken from integration across the NAA frequency band in the first echo spectroscopic data sets of the column (TE = 145 ms, Figure 6.3 (c)). The metabolites trace has been multiplied by a scaling factor to make it comparable to the water trace for visualization. Both traces show coincident spikes at the edges of the skull due to strong lipid signal in the T_1-weighted localizer and to lipid signal bleed along the frequency direction into the NAA band at scalp locations in the TE = 145 ms spectroscopic image. Of interest is the correlation between signal drops at ventricle locations in the T_1-weighted water profiles and drops in the NAA integrated signal intensity at the same locations, presumably due to partial volume averaging of NAA containing brain tissue with non-NAA containing cerebrospinal fluid.

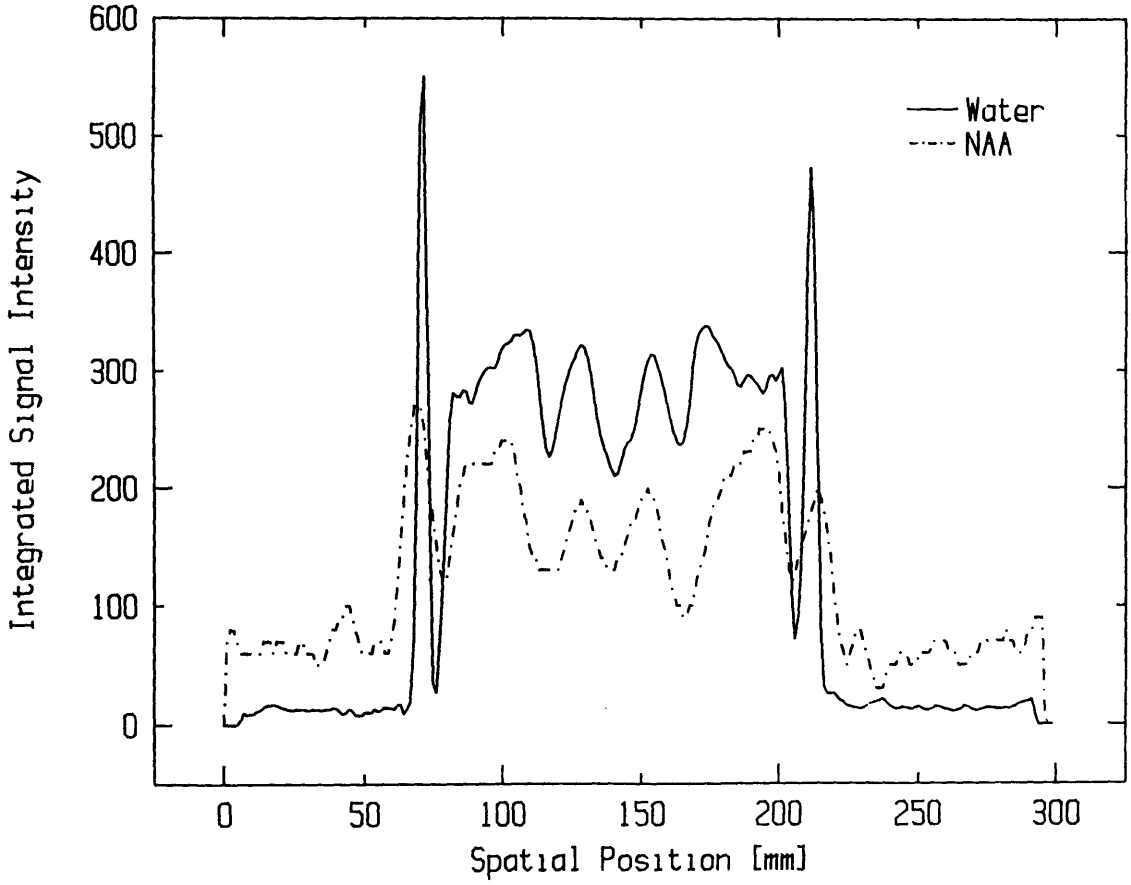

Figure 6.6: The integrated water and NAA signal intensities as functions of position along the column outlined in Figure 6.3 (a). The water trace was taken directly from integration of signal intensity across the column dimension in the T1-weighted image of Figure 6.3 (a). The NAA trace was taken from integration across the NAA frequency band in the first echo spectroscopic image (Figure 6.3 (c)). The metabolites trace has been multiplied by a scaling factor to make it comparable to water trace for visualization. Good correlation is observed between the two traces with coincident dips at locations of the ventricles and spikes at locations in the scalp.

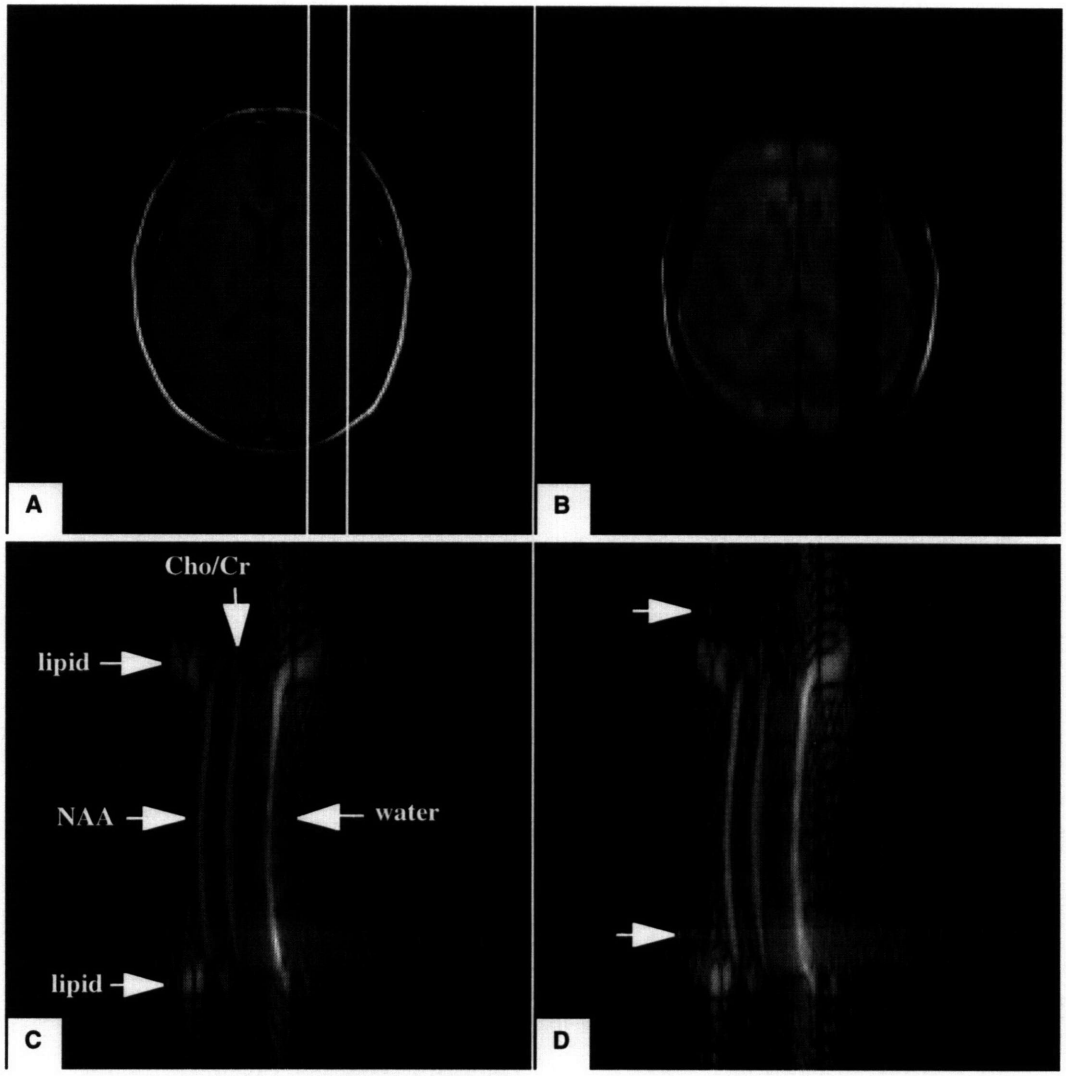

Figure 6.7: Line scan CPMG study of a healthy 26-year-old man with the 20 mm thick column oriented anteriorly to posteriorly. **(a):** One of five localizing images acquired in 23 seconds with a 3-echo RARE acqusition. **(b):** A T1-weighted 15 seconds scout image used to quickly outline and confirm the position of the targeted tissue column with a dark saturation band. Unlike Figure 6.2, the multiplicative factor of 350 are not applied to the sampled data. **(c):** First echo spectroscopic image with TE of 114 ms. **(d):** The summed spectroscopic image generated by adding data from the first 3 echoes of the CPMG acquisition.

A total of eight healthy volunteers were studied with the 5 echo CPMG line scan to determine metabolites T_2 values. Five studies were performed with the columns aligned from left to right as in Figure 6.3. Four of them were scanned with 128 ms readout, 145 ms echo spacing and one with 96 ms readout, 114 ms echo spacing. Three studies were performed with the columns oriented from anterior to posterior as in Figure 6.7, all using the 96 ms readout and 114 ms echo spacing. The TR was 2 seconds for all 8 studies. From each data set, 4 to 6 brain spectra were extracted from $15 \times 15 \times 5$ mm^3 or $20 \times 20 \times 5$ mm^3 nominal voxel volumes and spectral peaks fit with Gaussian functions at every TE, as in Figure 6. 4. Table 6.1 lists the ranges of T_2 values found for the NAA signal and the composite Cho+Cr signal. The mean and standard deviations are the results from 45 spectral T_2 decay data sets. The ratio of the NAA signal to the combined Cho+Cr signal calculated from spectral peak areas extrapolated back to zero TE is 0.95 ± 0.34.

	Range (ms)	Mean ± SD (ms)
Cho/Cr	175 - 769	286 ± 82
NAA	277 - 772	435 ± 113

Table 6.1: T2 values obtained from analysis of 45 spectral relaxation data sets of 8 healthy adult volunteers. T2 for the Cho/Cr peak was smaller than that for NAA peak.

Figure 6.8 is an example of the techniques as applied to a 17-year-old boy with a brain tumor of glial origin. Shown are the 20×20 mm^2 tissue column selected for interrogation from a T_2-weighted localizing image (a), the summation image generated from the first 3 echoes of a 5-echo CPMG data set (b), and the 3 echo RARE spectroscopic image acquired only in 90 seconds (c). The scan parameters are identical to those used for Figure 6.3. The location of the tumor, marked with an arrow in Figure 6.8 (b), clearly shows a depletion of NAA signal and an increase in the combined Cho+Cr peak, presumably due to increased choline in tumor cells. Note that with this spectral resolution,

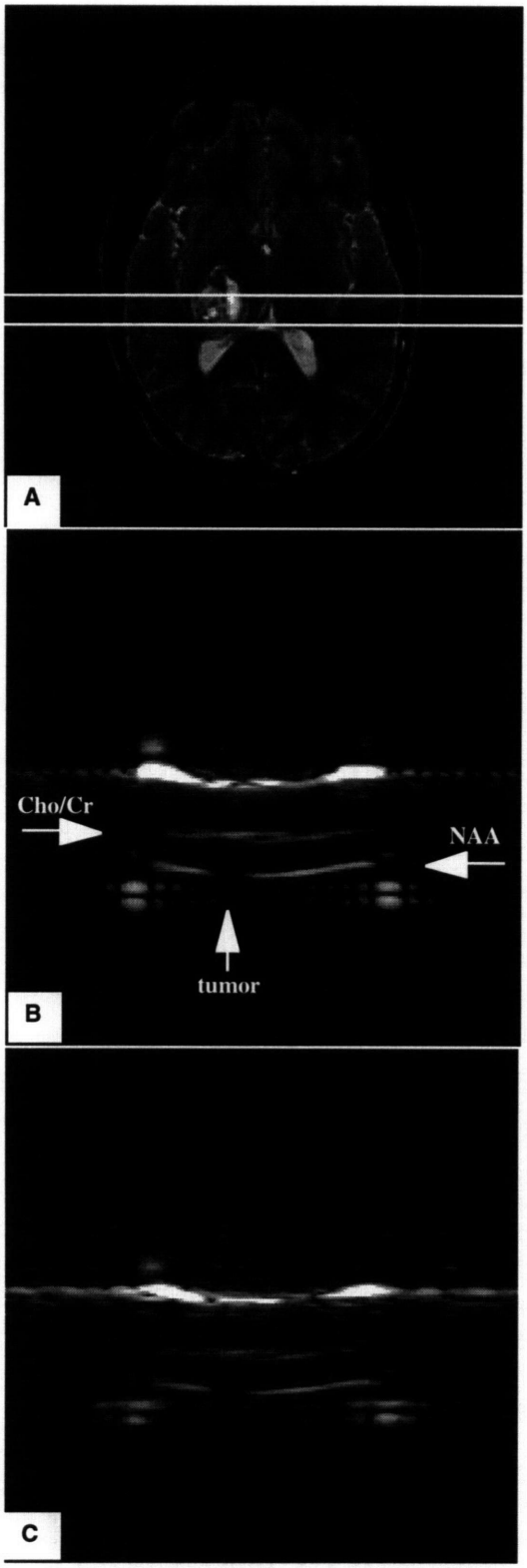

Figure 6.8 (a): RARE T2-weighted localizer shows the tumor and the 20 mm thick column. **(b):** Summation image using data from the first 3 echoes of a 5-echo CPMG acquisition. **(c):** The spectroscopic image of the 90 seconds RARE acquisition with effective TE of 290 ms.

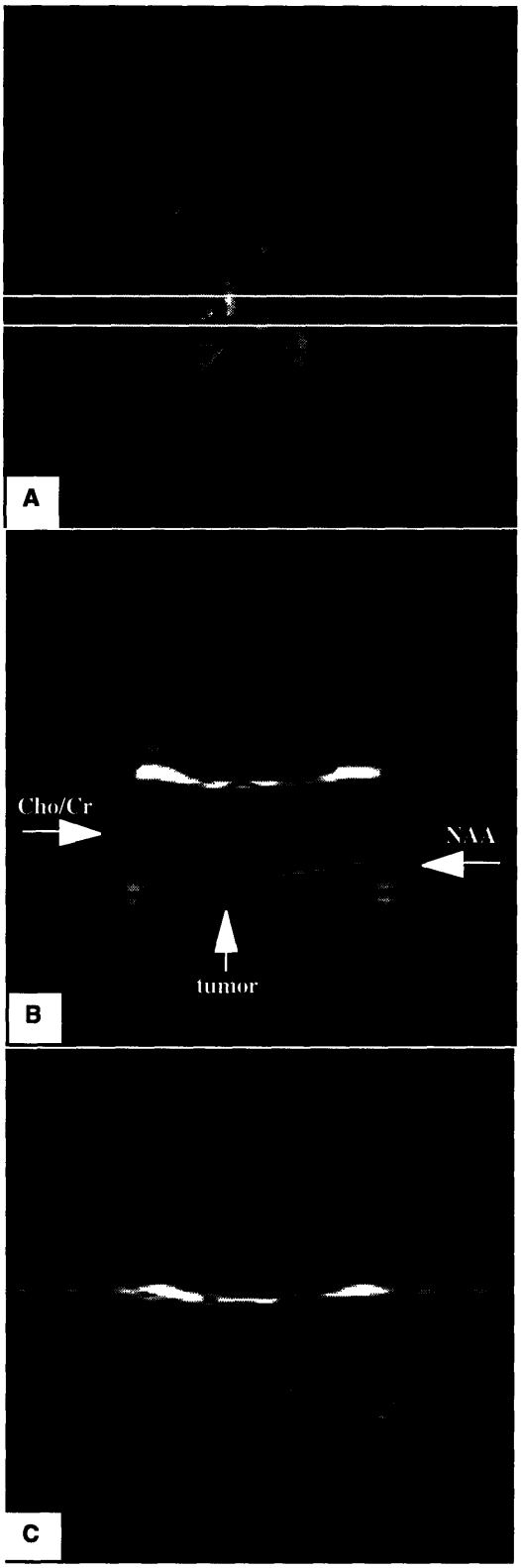

Figure 6.8 (a): RARE T2-weighted localizer shows the tumor and the 20 mm thick column. **(b):** Summation image using data from the first 3 echoes of a 5-echo CPMG acquisition. **(c):** The spectroscopic image of the 90 seconds RARE acquisition with effective TE of 290 ms.

Figure 6.9 (a) and (b) are plots of spectra at each echo time extracted from locations in the tumor and from normal brain tissue on the contralateral side for the patient in Figure 6.8. The nominal voxel size is $20 \times 20 \times 5$ mm^3. The T_2 value of the composite Cho+Cr peak in the tumor, averaged from two locations, was 303 $\pm$ 37 ms. The Cho+Cr T_2 value for normal brain tissue, averaged from four separate $20 \times 20 \times 5$ mm^3 voxels located on the contralatereal side was 385 $\pm$ 45 ms. A similar scan performed on this patient four month later and with no intervening treatment yielded T_2 values for Cho+Cr of 322 $\pm$ 42 ms in the tumor and 411 $\pm$ 47 ms in normal brain tissue, consistent with results from the first scan.

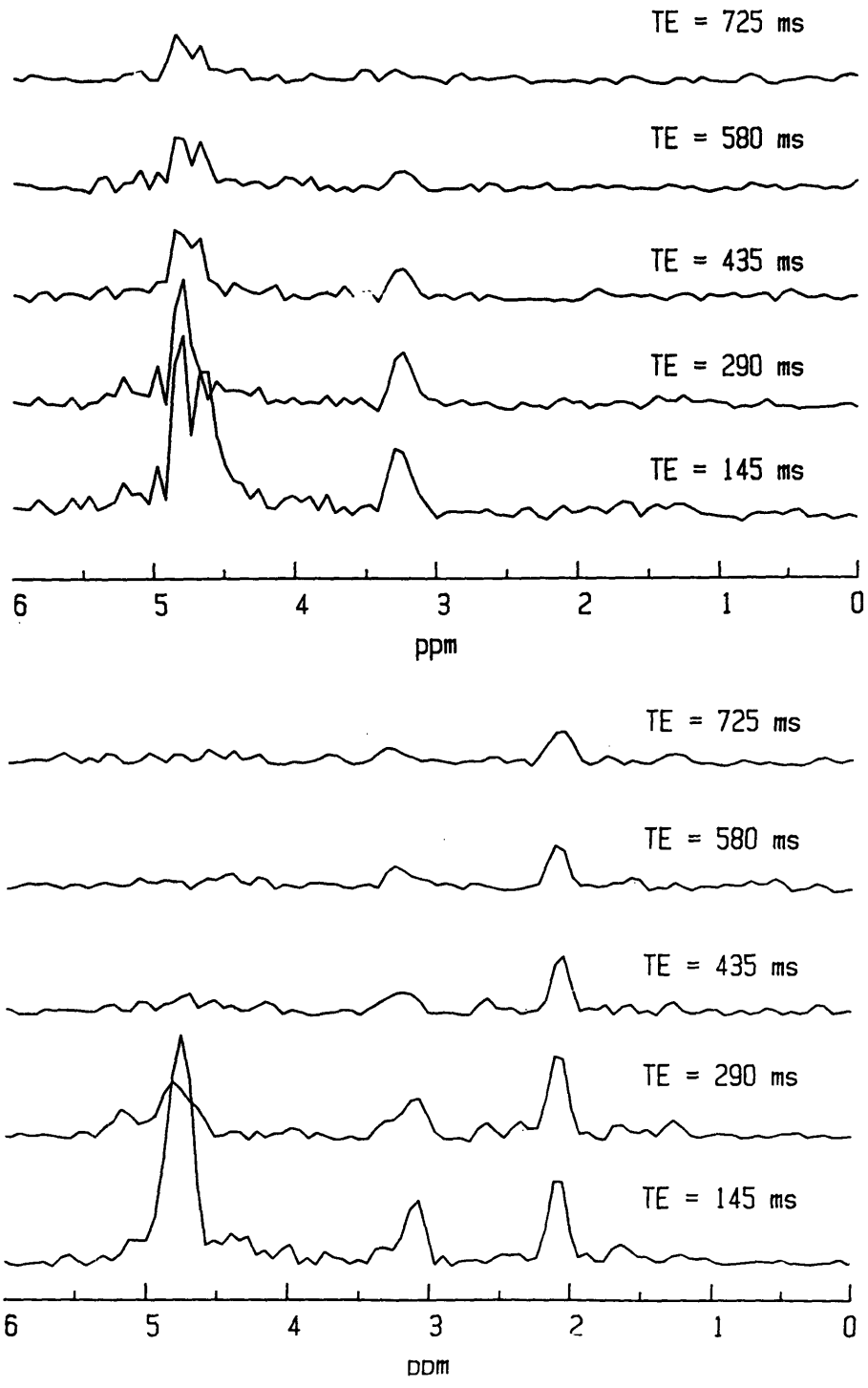

Figure 6.9. (top): CPMG spectra of 5 TEs from a voxel located in the tumor as pointed by the arrow in Figure 6.8 (b). Only residual water and the combined Cho+Cr signal are apparent in the spectra. **(bottom):** CPMG spectra from a voxel in normal brain tissue (contralateral side) of the tumor patient showing both Cho+Cr and NAA signals.

Figure 6.10 presents spatial profiles for combined Cho+Cr, NAA, and water signals for the tumor patient in Figure 6.8. The metabolites signals are integrated across the column from the summation image of Figure 6.8 (b), and the water profile extracted from T_2-weighted localizer of Figure 6.8 (a). The vertical scaling of the metabolites was performed to allow a comparison with the water profile. Horizontal scaling was also performed to account for the different FOV for the localizing image and spectroscopic image. The sharp lipid peak provide a natural reference points for checking the horizontal scaling factor. Note how the dip in NAA signal and the increase in the Cho+Cr signal corresponds to increased water signal in the tumor.

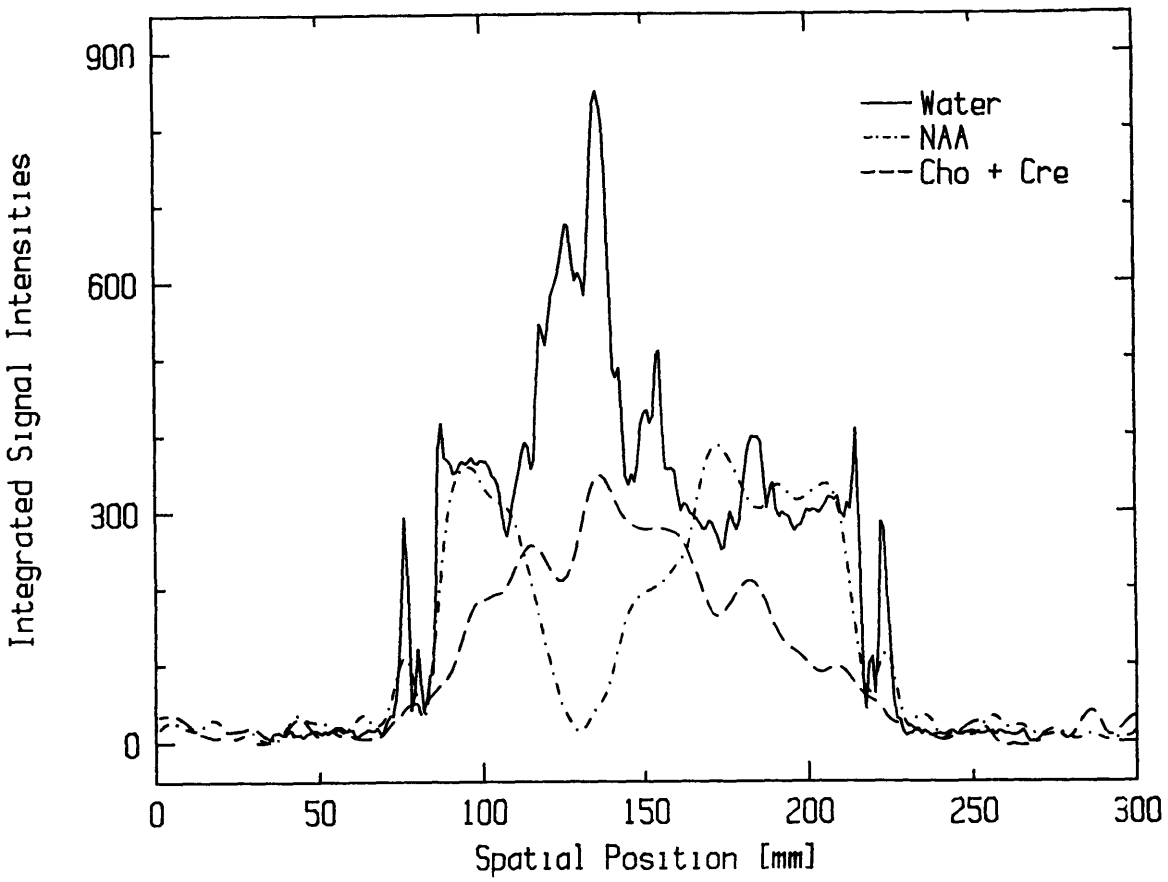

Figure 6.10: Spatial profiles of the water signal, and scaled NAA, Cho+Cr signals along the tissue column. The water trace was extracted from T2-weighted localizer image of Figure 6.8 (a). The vertical scaling of the metabolites was performed to allow a comparison with the water profile. Note the correlation between the high Cho+Cr signals and the low NAA signals with the high water intensities at the tumor locations.

6.3 Discussion

Two dimensional proton spectroscopic studies of long T_2 brain metabolites have become well established areas of investigation, though they have not become standard tools in clinical neuroradiological MR exams. Typically, scan time greater than 30 minutes have been required to generate relatively low spatial resolution 2D (32×32 matrix size) brain metabolites maps of one or several selected slices [4, 11, 20, 23]. Patients, technologists, and clinicians have become more accustomed to MR examinations consisting of several individual scans, each lasting on the order of only several minutes. It therefore becomes investigators interest in seeing wider clinical application of brain spectroscopy to explore methods that extract spectroscopic information within scan time generally tolerated by MR practitioners and patients.

Within this context, it has been shown that the use of individual CPMG generated echoes for different spatial phase encodes steps allows for 32×32 spatial array mapping of brain metabolites in approximately 10 minutes [29, 30]. For some applications, the volume coverage and spatial resolution afforded by such 2D CSI metabolites mapping may be required. Instead of expensive hardware upgrading with echo planar capabilities [35, 36], the 2D CSI studies with distinct phase encoding scheme for each echo are the practical choice.

Mapping metabolites with 2D CSI methods is advantageous in that results can be displayed in familiar image formats and overlaid with anatomically accurate standard MR images. However, limitations of the multi-echo approach for 2D CSI brain metabolite mapping are worth mentioning. First, the 128 ms echo readouts used to allow for the collection of 4 echoes prior to unacceptable signal loss from T_2 decay limits spectral resolution, making the separation of Cho from Cr resonance problematic. As noted elsewhere [29] and here, more sophisticated lineshape analyses of the 2.9 to 3.3 ppm spectral region may help alleviate this problem, especially if signal-to-noise can be

improved through coil development. However, to date, only 2D CSI maps of the combined Cho+Cr resonance have been reported with rapid multi-echo approaches because of this problem.

Another drawback of using multiple echoes for rapid scans (in 3D, 2D or 1D formats) is that metabolites T_2 decay processes manifest themselves as artifact rather than as a potential sources of diagnostic or physiological information. Such artifacts are fairly well understood, and presenting themselves as ringing and spatial blurring along the phase encode direction sampled with separate echoes [34]. The T_2 decay caused spatial spread of signal is quite apparent in the 90 second RARE line scan acquisitions (Figure 6.3 (f) and 6.8 (c)). Duyn and Moonen applied T_2 correction factors to the individual raw data lines based on the assumption of a global T_2 value of 400 ms to decrease the artifact [30]. Such strategies help in the qualitative presentation of the data but do not make quantitative T_2 analyses possible. It is well-recognized that spectral peak amplitudes at a single echo time, or this case a single effective echo time, reflect both metabolites concentrations and T_2 relaxation. Since metabolites T_2 information is traded off for speed when multiple echoes are used to bring 2D CSI brain scan times into clinically acceptable ranges, definitive statements as to the precise cause of spectral changes (concentration or T_2 change) remain elusive.

As demonstrated above, the line scan makes quantitative brain metabolite T_2 analyses feasible. In applications in which the volume coverage provided by a line scan format is acceptable, the complete data sets can be acquired in less than 10 minutes. The major drawback encountered with the present implementation is the overlapping Cho and Cr resonances, precluding separate T_2 quantification of these peaks. Other limitations of the metabolite T_2-decay data sets acquired with the CPMG method include inherently low signal-to-noise ratios and the sampling of only 3 to 5 data points along the T_2-decay curve. These features account for the rather wide range of metabolites T_2 values reported in Table

6.1. However, despite the limitations mentioned, our T_2 measurement demonstrate quite reasonable agreement with existing literature data on brain metabolites T_2 parameters. The NAA T_2 values of 435 ± 113 which we found (Table 6.1) by averaging 45 NAA T_2-decay data sets from 8 volunteers is in good agreement with published reports found by others using single voxel techniques [16, 17]. The T_2 value which we found for the combined Cho+Cr of 286 ± 82 ms (Table 6.1) is intermediate to the individual spectral T_2 values at 1.5 T reported by Kreis et al [17] who list a Cr T_2 value of 207 ms and a Cho T_2 value of 395 ms for adults. This makes it quite apparent that the T_2 relaxation time measured from single Gaussian fits to the 3.3 to 2.9 ppm spectral region reflect both Cho and Cr resonances. It is also of interest to note that our value of 0.95 ± 0.34 for the ratio of NAA to combined Cho+Cr, as estimated from the spectral peak area extrapolated to zero TE, is reasonably close to the value of 0.81 for this particular metabolite ratio as extracted from single voxel STEAM data recently compiled by Webb et al in adults [18]. The finding suggests that in any application in which NAA/(Cho+Cr) proves to be a useful index, the CPMG line scan spectroscopic techniques can provide reasonable estimate of this quantity.

A potential application for the line scan CPMG techniques as currently implemented is in the characterization of brain tumors (Figure 6.8). In particular, long TE spectroscopic findings in tumor to date have generally reported diminished NAA and Cr resonances and an increased Cho peak [2-6]. Thus, our T_2 measurement from the peak in the 3.0 to 3.3 ppm spectral region in tumor most probably reflects primarily Cho peak with little contamination from the Cr. Using single voxel approaches, several investigators have measured metabolites T_2 values in tumors and surrounding tissue. Manton et al measured increases in Cho T_2 values in meningiomas compared with normal brain tissue [37] and suggested that their result may due to a difference in the relative proportion of glycerophosphocholine to phosphocholine, the two major compounds contributing to the in vivo Cho peak [38]. Usenius et al also reported increased Cho T_2 values in several tumor

types [39] while Kamada et al reported T_2 shortening of Cho resonances and other metabolites peaks in peritumoral edema of several patients, including two meningioma cases [40]. In the single tumor case we have examined with the line scan CPMG technique, the Cho T_2 appeared shorter than the Cho+Cr T_2 in normal brain tissue, consistently in two separate exams. We speculate that calcium deposition may play some role in the T_2 shortening observed but hasten to add that many more studies are required before definitive conclusions can be drawn as to the mechanisms affecting metabolite T_2 values in tumor. The line scan approach is appealing in this regard since a single relatively brief scan yields data sets from which such information can be extracted from both normal and pathological tissue.

The final application considered with multiple echo CPMG type acquisitions is the addition of echoes for improving signal-to-noise. Since noise in different echoes is uncorrelated, a gain in signal-to-noise may be anticipated when echoes are added to form summation data sets like those shown in Figure 6.3 (g). However, T_2-decay also plays a role, diminishing the signal-to-noise gains obtained by adding successive echoes. For the NAA peak of the cases in Figure 6.3 (g), only a modest gain in signal-to-noise of approximately 15% was obtained when raw data from the first 3 echoes at 145, 290, 435 ms were added. This result suggests that echo addition does not present a major advantage of CPMG spectroscopic imaging scans in brain.

References

1. Miller B. A review of chemical issues in ^{1}H NMR spectroscopy: A-Acetyl-L-aspartate, Creatine and Choline. NMR in Biomedicine, 1991; 4: 47-52.

2. Alger JR, Frank JA, Bizzi A, Fulham MJ, DeSouza BX, Duhaney MO, Inscoe SW, Black JL, van Ziji PCM, Moonen CTW, Di Chiro G. Metabolism of Human Gliomas: Assessment with ^{1}H MR spectroscopy and F^{18} Fluorodeoxyglucose PET. Radiology 1990; 177: 633-641.

3. Segerbarth CM, Baleriaux DF, Luyten PR, den Hollander JA. Detection of metabolic heterogeneity of human intracranial tumors in vivo by ^{1}H NMR spectroscopic imaging. Magn. Reson. Med 1990; 13: 62-76.

4. Fulham MJ, Bizzi A, Dietz MJ, Shih HHL, Raman R, Sobering GS, Frank JA, Dwyer AJ, Alger JR, Di Chiro G. Mapping of brain tumor metabolites with proton MR spectroscopic imaging: Clinical relevance. Radiology 1992; 185: 675-686.

5. Tzika AA, Vigneron DB, Ball WS, Dunn RS, Kriks DR. Localized proton MR spectroscopy of the brain in children. J Magn Reson Imag 1993; 3: 719-729.

6. Barker PB, Glickson JD, Bryan RN. In vivo magnetic resonance spectroscopy of human brain tumors. Top Magn Reson Imag 1993; 5: 32-45.

7. Berkelbach Van der Sprenkel JW, Luyten PR, van Rijen PC, Tulleken CAF, den Hollander JA. Cerebral lactate detected by regional proton magnetic resonance spectroscopy in a patient with cerebral infarction. Stroke 1988; 19: 1556-1560.

8. Bruhn H, Frahm J, Gyngell ML, Merboldt KD, Hanicke W, Sauter R. Cerebral metabolism in man after acute stroke: New Observations using localized proton NMR spectroscopy. Magn. Reson. Med 1989; 9: 126-131.

9. Van Hecke P, Marchal G, Johannik K, Demaerel P, Wilms G, Carton H, Baert AL. Human brain proton localized NMR spectroscopy in multiple sclerosis. Magn Reson Med 1991; 18: 199-206.

10. Tzika AA, Ball WS, Vigneron DB, Dunn RS, Kirks DR. Clinical proton MR spectroscopy of neurodegenerative diseases in childhood. AJNR 1993; 14: 1267-1281.

11. Fulham MJ, Dietz MJ, Duyn JH, Shih HHL, Alger JR, Di Chiro G. Transsynaptic reduction in N-acetyl-aspartate in cerebellar diaschisis: A proton MR spectroscopic imaging study. J. Comput Assist Tomogr 1994; 18: 697-704.

12. Bruhn H, Kruse B, Korenke GC, et al. Proton MR spectroscopy of cerebral metabolic alterations in infantile peroxisomal disorders. J. Compu Assist Tomogr 1992; 16: 335-344.

13. Frahm J, Merboldt KD, Hanicke W. Localized proton spectroscopy using stimulated echoes. J Magn Reson 1987; 72: 502-508.

14. Frahm J, Bruhn H, Gyngell ML, Merboldt KD, Hanicke W, Sauter R. Localized high resolution proton NMR spectroscopy using stimulated echoes: initial applications to human brain in vivo. Magn Reson Med 1989; 9: 79-93.

15. Frahm J, Bruhn H, Gyngell ML, Merboldt KD, Hanicke W, Sauter R. Localized proton NMR spectroscopy in different regions of the human brain in vivo. Relaxation times and concentrations of cerebral metabolites. Magn Reson Med 1989; 11: 47-63.

16. Bottonley PA. Spatial localization in NMR spectroscopy in vivo. Ann NY Acad Sci 1987; 508: 333-348.

17. Kreis R, Ernst T, Ross BD. Development of the human brain: In vivo quantification of metabolite and water content with proton magnetic resonance spectroscopy. Magn Reson Med 1993; 30: 424-437.

18. Webb PG, Sailasuta N, Kohler SJ, Raidy T, Moats RA, Hurd RE. Automated single voxel proton MRS: Technical development and multisite variation. Magn Reson Med 1994; 31: 365-373.

19. Brown TR, Kincaid BM, Ugurbil K. NMR chemical shift imaging in three dimensions. Proc Natl Acad Sci 1982; 79: 3523-3526.

20. Duyn JH, Gillen J, Sobering G, van Ziji PCM, Moonen CTW. Multisection proton MR sepctroscopic imaging of the brain. Radiology 1993; 188: 277-282.

21. Dreher W, Leibfritz D. Double-echo multislice proton spectroscopic imaging using Hadamard slice encoding. Magn Reson Med 1994; 31: 596-600.

22. Maudsley AA, Matson GB, Hugg JW, Weiner MM. Reduced phase encoding in spectroscopic imaging. Magn Reson Med 1994; 31: 645-651.

23. Husted CA, Duijn JH, Matson GB, Maudsley AA, Weiner MW. Molar quantitation of in vivo proton metabolites in human brain with 3D magnetic resonance spectroscopic imaging. Magn Reson Imag 1994; 12: 661-667.

24. Carr HY, Purcell EM. Effects of diffusion on free precession in nuclear magnetic resonance experiments. Phys Rev 1954; 94: 630-638.

25. Meiboom S, Gill D. Modified spin-echo method for measuring nuclear relaxation times. Rev Sci Instrum 1958; 29: 688-691.

26. Mulkern RV, Melki PS, Lilly HS, Hoffer FA. 1D spectroscopic imaging with RF echo planar (SIRFEN) methods. Magn Reson Imag 1991; 9: 909-916.

27. Oshio K, Mulkern RV. Rapid fat/water assessment in knee bone marrow with inner volume RARE spectroscopic imaging. JMRI 1992; 2:601-604.

28. Mulkern RV, Meng J, Oshio K, Guttmann CRG, Jaramillo D. Bone marrow characterization in the lumbar spine with inner volume spectroscopic CPMG imaging studies. JMRI 1994; 4:585-589.

29. Duyn JH, Moonen CTW. Fast proton spectroscopic imaging of human brain using multiple spin echoes. Magn Reson Med 1993; 30: 409-414.

30. Duyn JH, Frank JA, Moonen CTW. Incorporation of lactate measurement in multi-spin ehco proton spectroscopic imaging. Magn Reson Med 1995; 33: 101-107.

31. Jones KM, Unger EC, Granstrom P. Magn Reson Imag. 1992; 10: 169.

32. Haasse A, Frahm J, Hanicke W, Matthaei. ^{1}H NMR chemical shift selective imaging. Phys Med Biol 1985; 30: 341-344.

33. Hennig J, Naureth A, Friedburg H. RARE imaging: a fast imaging method for clicical MR. Magn Reson Med. 1986; 3:823-833.

34. Mulkern RV, Melki PS, Jakab P, Higuchi N, Jolesz FA. Phase encode order and its effect on contrast and artifact in single-shot RARE sequences. Med Phys 1991; 18: 1032-1037.

35. Matsui S, Sekihara K, Kohno H. High-speed spatially resolved NMR spectroscopy using phase-modulated spin-echo trains. Expansion of the spectral bandwidth by combined use of delayed echo trains. J. Magn Reson 1985; 64: 167-171.

36. Posses S, Tedeschi G, Risinger R, Ogg R, Le Bihan D. High speed ^{1}H spectroscopic imaging in human brain by echo planar spatial-spectral encoding. Magn Reson Med 1995; 33: 34-37. Manton DJ, Lowry M, Blackband SJ, Horsman A. Quantitative proton MRS of brain tumors reveals increased choline T_2 in meningiomas. MAGMA 1994; 2: 361-363.

38. Barker PB, Breiter SN, Soher BJ, Chatham JC, Forder JR, Samphilipo MA, Magee CA, Anderson JH. Quantitative proton spectroscopy of canine brain: in vivo and in vitro correlations. Magn Reson Med 1994; 32: 157-163.

39. Usenius JR, Kauppinen RA, Vainio PA, Hernesniemi JA, Vapalahti MP, Paljarvi LA, Soimakalli S. Quantitative metabolites patterns of human brain tumors: Detection by ^{1}H NMR spectroscopy in vivo and in vitro. J. Comput Assist Tomogr 1994; 18: 705-713.

40. Kamada K, Houkin K, Hida K, Matsuzawa H, Iwasaki Y, Abe H, Nakada T. Localized proton spectroscopy of focal brain pathology in humans: Significant effects of edema on spin-spin relaxation time. Magn Reson Med 1994; 31: 537-540.

Chapter 7

Conclusion and Future Topics

This thesis has presented innovative proton magnetic resonance spectroscopic imaging techniques and their clinical applications *in vivo*. This chapter summarizes the thesis and suggests some of the potential clinical applications. In addition, the modification of current techniques and future topics for research that are relevant to this thesis are discussed.

7.1 Conclusion

This thesis and its contributions to the field of magnetic resonance spectroscopic imaging are summarized as follows:

- This thesis has developed and implemented innovative magnetic resonance spectroscopic imaging methodologies. The methods are based on spectroscopic interrogation of voxels along strategically oriented tissue columns which can be selected on-line. The techniques combine some of the most attractive features of both imaging and spectroscopy methods utilizing Carr-Purcell-Meiboom-Gill multiple-echo sequence, rapid acquisition and relaxation enhanced or equivalently fast spin echo sequence, inner-volume localization, and chemical shift imaging principles. The techniques offer a compromise between the low-spectral-resolution, high-spatial-resolution, large-volume-coverage imaging methods of Dixon and Sepponen and the high-spectral-resolution, single-voxel localized proton spectroscopy approaches. Spectroscopic images with high spatial, variable

spectral resolution and adequate volume coverage are generated in clinically useful time periods of 10 minutes or less.

- The techniques can be performed either in imaging mode or in spectroscopy mode. In imaging mode, localizing images with a saturated dark band representing the selected tissue column are generated with the standard RARE sequence. In spectroscopy mode, spectroscopic images of the column are created with either the CPMG or the RARE sequence. The CPMG spectroscopic imaging techniques allow spectral quantitation (concentration and T_2) from eight separate TEs in each voxel along the tissue column. The RARE spectroscopic imaging techniques provide rapid mapping of proton spectral resonances and estimation of spectral T_1 relaxation time.
- The spectroscopic imaging techniques developed in this thesis are fast ad non-invasive in the clinical setting. The techniques generate spectroscopic images much faster than conventional MR spectroscopic techniques while the images are still informative. As current implemented, the CPMG spectroscopic imaging techniques generated images that suitable for spectral T_2 and concentration analysis in 4 minutes and 18 seconds while conventional spectroscopic techniques need scan time of 40 minutes. The RARE spectroscopic imaging techniques with 7 echo train generate image in 36 seconds versus 4.5 minutes for the conventional spectroscopic techniques. Because of the short scan time, the techniques developed in this thesis are tolerated by patients and MR practitioner. Also they make practical spectroscopic studies (such as on very ill patients or on children) feasible.
- The new methodologies are developed and implemented on a conventional 1.5 Tesla clinical MRI scanner with standard software and hardware configurations. Therefore, it is convenient to extract spectroscopic information along with conventional MRI examinations. The practical significance of the technologies is that they can be feasibly incorporated into clinical protocols to perform spectroscopic studies on clinically important targets.
- The techniques provides the optimization between acquisition speed, spectral resolution, minimum echo time, and T_2 measurement. The spectroscopic images can be

acquired with different spectral resolution. The variable spectral readouts and the corresponding minimum echo spacing, as well as the echo train length, can be chosen on-line for different applications. The long sampling time yields images with high spectral resolution, and prolongs the echo spacing. As a result, the amount of unavoidable T_2 decay increases in the multiple echo train. On the other hand, the small echo spacing decreases the T_2 decay and increases the signal to noise ratio, so more echoes per TR can be obtained in the multiple echo train acquisitions. The CPMG spectroscopic imaging sequence trades spectral resolution for spectral T_2 measurement while the RARE spectroscopic imaging technique sacrifices spectral T_2 measurement for acquisition speed.

- The spectroscopic imaging techniques are demonstrated *in vivo*. Spectral concentrations, T_1 and T_2 relaxation values are obtained for bone marrow and brain metabolites. Specifically, quantitation of water and saturated fat, or cellularity measurement, is performed on vertebral marrow of a group healthy adult volunteers. Studies of developing bone marrow in knee are performed on a group of children and a group of adult volunteers. Furthermore, with variable spectral resolution and an added non-selective inversion pulse before the excitation, the techniques are shown applicable in quantifying the lipid chemical composition. The demonstrations also include lipid spectral T_1 relaxation measurements, terminal methyl proton detection even at limited spectral resolution, mapping of fat unsaturation, and study of levels of mono-unsaturated versus poly-unsaturated triglycerides. In addition, the techniques are modified with three CHESS pulses to suppress water, and applied to quantify and map human brain metabolites. The clinical feasibility of brain metabolites studies is illustrated from a group of healthy adult volunteers and a tumor patient.
- The thesis designed an automated image analysis software package. The image processing software, designed in graphics user interface format on Sun workstation, makes it convenient to extract spectroscopic information from acquired spectroscopic images.

- The fast techniques demonstrated in this thesis may provide opportunities to perform dynamic chemical shift imaging studies *in vivo*. Like functional MRI where many fast imaging techniques have been developed, the fast scan spectroscopic imaging techniques are also essential in dynamic chemical shift studies. In contrast to echo-planar imaging that requires specialized and expensive hardware for fast gradient switching, large peak amplitudes and fast data acquisition, the new MR spectroscopic imaging techniques require no special hardware and software since they are developed on conventional scanner with standard configuration.

7.2 Potential Applications

The new methodologies has been demonstrated applicable in many possible applications, such as spectral quantitation of bone marrow in vertebral and knee, metabolites mapping in human brain. Also the feasibility to study the lipid chemical composition and degree of triglycerides in fatty acids are presented.

The techniques developed in this thesis promise many possible applications *in vivo*. One is to quantitate lipid spectra in bone marrow during and after radiation therapy and chemotherapy for patients with bone marrow diseases like leukemia. Another one is to study the evolution of cerebral metabolites within brain tumors to see how relative concentrations of MR observable metabolites correlate with the state of the tumors and the relative progress of various therapies. The other application is to study fat metabolites disorders, such as cystic fibrosis.

7.3 Future Topics for Research

7.3.1 Lipid Enhancement

One future work that is relevant to this thesis is to boost the small lipid resonance peaks other than methylene peak by modifying the line scan CPMG spectroscopic imaging techniques. As presented in thesis, the small lipid peaks contain information about lipid chemical structure, such as fatty acid chain length, degree of mono-unsaturation and poly-unsaturation.

The problem encountered in performing conventional spin echo technique to study the small lipid resonance protons is the low signal-to-noise ratio. To enhance these small lipid resonance signals, we propose that the line scan CPMG spectroscopic techniques be further modified. Instead of sampling each echo after every 180° pulse in a CPMG echo train, only the positive half of the last echo is sampled. The volume localization is still a column. The new CPMG pulse sequence is like: $\pi/2$ (+x), τ, π (+y), 2τ, π (+y), 2τ, ..., π (+y), τ, positive-half-echo-readout. The TE of the spectroscopic image is $n(2\tau)$, where n is the number of echo per TR. The reason of acquiring only the positive half echo is to make TE independent of sampling time when variable spectral readout filters are used. Another reason is that the TE is shortened so that the small T_2 species can be observed.

To demonstrate the lipid enhancement over the conventional spin echo technique, we have modified the line scan CPMG spectroscopic imaging sequence as described above and applied it on a bottle of fish oil. For comparison, a spin echo sequence that is modified with volume localization being a column is also used to sample spectral information without readout gradient from the same fish oil bottle. The TEs used for both sequences are the same. The location of the column in the spin echo sequence is the same as in the modified line scan CPMG spectroscopic sequence. As in the CPMG acquisition, only the positive half echo is sampled in the spin echo sequence. Therefore, the only difference between these two sequences are the multiple selective refocusing 180° pulses used in the CPMG sequence.

Our initial study has observed the lipid enhancement by the modified CPMG spectroscopic imaging sequence over the spin echo sequence. The olefinic proton peak is

enhanced about 100% in CPMG acquisition. The lipid enhancement may result from the elimination of diffusion-mediated susceptibility dephasing and the suppression of J-coupling modulation from multiple refocusing pulses train as shown by Henkelman [1]. Further *in vitro* and *in vivo* studies are needed to prove the applicability of such proposal.

7.3.2 Diffusion Spectroscopic Imaging

Another future work that is relevant to this thesis is to study diffusion properties of brain metabolites by extending the line scan CPMG spectroscopic imaging techniques. The rationale is that *in vivo* diffusion coefficients measurement contains information about cellular parameters such as dimensionality, compartmentation, and transport processes. Previous clinical applications include determination of white matter fiber orientation in the central nervous system, and evaluation of brain infarctions at very early stage when findings of other modalities, including T_1- and T_2-weighted MR image are still normal [2].

We propose that the line scan CPMG spectroscopic techniques be modified either to acquire diffusion weighted spectroscopic images or to measure the diffusion coefficients of the low concentration brain metabolites. Specifically, three bi-polar diffusion gradients, each in one direction (x, y, and z), can be added between excitation 90° pulse and the first refocusing 180° pulse. The duration of the diffusion gradients is arranged not to increase the echo spacing as the full echo after every refocusing pulse is sampled. So the modified line scan CPMG spectroscopic acquisition will generated images at different TEs that contain both spectral T_2 and diffusion information. By varying the amplitude of the diffusion gradients, the spectral diffusion coefficients for brain metabolites can be measured.

References

1. Henkelman RM, Hardy PA, Bishop JE, Poon CS, Plewes DB. Why fat is bright in RARE and fast spin echo imaging. JMRI 1992; 2: 533-540.

2. Posse S, Cuenod CA, LeBihan D. Human brain: Proton diffusion MR spectroscopy. Radiology 1993; 188: 719-725.